

**İSTANBUL TECHNICAL UNIVERSITY ★ INSTITUTE OF SCIENCE AND TECHNOLOGY**

**MICROMACHINING OF SI-WAFER WITH FEMTOSECOND LASER  
TECHNOLOGY**

**M.Sc. Thesis by  
Şirin Didem SOFUOĞLU**

**Department : Defence Technologies**

**Programme : Materials and Manufacture**

**OCTOBER 2011**



**MICROMACHINING OF SI-WAFER WITH FEMTOSECOND LASER  
TECHNOLOGY**

**M.Sc. Thesis by  
Şirin Didem SOFUOĞLU  
(514071010)**

**Date of submission : 09 September 2011  
Date of defence examination: 06 October 2011**

**Supervisor (Chairman) : Assoc. Prof. Levent TRABZON (ITU)  
Members of the Examining Committee : Prof. Dr. Şafak YILMAZ (ITU)  
Assis. Prof. Dr. Hüseyin KIZIL (ITU)**

**OCTOBER 2011**



**İSTANBUL TEKNİK ÜNİVERSİTESİ ★ FEN BİLİMLERİ ENSTİTÜSÜ**

**FEMTOSANIYE LAZER İLE Sİ-PLAKA ÜZERİNE MİKRO ÖLÇEKTE  
BİÇİMLENDİRME**

**YÜKSEK LİSANS TEZİ  
Şirin Didem SOFUOĞLU  
(514071010)**

**Tezin Enstitüye Verildiği Tarih : 09 Eylül 2011**

**Tezin Savunulduğu Tarih : 06 Ekim 2011**

**Tez Danışmanı : Doç Dr. Levent TRABZON (İTÜ)  
Diğer Jüri Üyeleri : Prof. Dr. Şafak YILMAZ (İTÜ)  
Yrd. Doç. Dr. Hüseyin KIZIL (İTÜ)**

**EKİM 2011**



## **FOREWORD**

Femtosecond laser micromaching has many advantages compared to other laser regimes. In order to benefit from these advantages simple but important rules must be followed when using this technology. In order to find these simple rules a wide range of parameters have been tested to achieve the perfect micromachined surfaces as desired.

First of all I would like to thank my beloved fiancé Mehmet Onder, my partner Zeynep Onder, my mother Hulya Sofuoglu, my father Mehmet Bugra Sofuoglu, my Grandparents Pertev Sahir Ergir, NevNihal Ergir, Mustafa Zeki Sofuoglu , Mukadder Sofuoglu and the rest of the family for all the support they have given me.

I would also like to thank my lab colleagues Mustafa Yilmaz, Berna Yalizay, Ozer Oztop, Ozgur Aydinli, Deniz Esgin, Cagdas Tunc & Melissa Seyrek Intas for making my working environment a joy.

Last but not least, I would like to thank my post graduate adviser Assc. Prof. Levent Trabzon, my teachers Asst. Prof. Selcuk Akturk, Asst. Prof. Huseyin Kizil, my undergraduate adviser Prof. Cenap S. Ozben, Prof. Ahmet Togo Giz, Prof. Huceste Giz and my highschool physics teacher Nevcivan Balta for guiding my way through.

October 2011

Şirin Didem Sofuoğlu  
Physics Engineer



## TABLE OF CONTENTS

	<u>Page</u>
<b>FOREWORD</b> .....	<b>v</b>
<b>TABLE OF CONTENTS</b> .....	<b>vii</b>
<b>ABBREVIATIONS</b> .....	<b>ix</b>
<b>LIST OF TABLES</b> .....	<b>xi</b>
<b>LIST OF FIGURES</b> .....	<b>xiii</b>
<b>SUMMARY</b> .....	<b>xix</b>
<b>ÖZET</b> .....	<b>xxi</b>
<b>1. INTRODUCTION</b> .....	<b>1</b>
1.1 Purpose of the Thesis .....	1
1.2 Electromagnetic Spectrum .....	1
1.3 Femtosecond Lasers .....	2
1.4 Femtosecond Laser Advantages over Nanosecond Laser in Thermal Diffusion and Material Choices.....	2
<b>2. FEMTOSECOND LASER MICROMACHINING</b> .....	<b>5</b>
2.1 Laser Properties And Their Effects On Micromachining .....	6
2.1.1 Scan Speed .....	6
2.1.2 Cycle And Passovers.....	8
2.1.3 Pulse Duration.....	8
2.1.4 Frequency (Repetition Rate) .....	9
2.1.5 Number Of Pulses .....	9
2.1.6 Energy / Power.....	11
2.1.7 Electric Field Polarization.....	12
2.1.8 Fluence .....	13
2.1.8.1 Fluence thresholds.....	14
2.1.9 Melting Threshold.....	15
2.2. Laser Ablation .....	16
2.2.1 Ablation Mechanisms .....	17
2.2.2 Ablation Threshold .....	17
2.3 Multiphoton Excitation (MPE).....	18
2.4 Ripple Formation.....	19
2.5 Heat Affected Zones (HAZ).....	20
2.6 Crater Depth Versus Laser Fluence .....	21
2.7 Surface Microstructures On Silicon .....	23
<b>3. EXPERIMENTAL SETUP</b> .....	<b>25</b>
3.1 S-Pulse.....	25
3.2 Laser Operationg Principles .....	25
3.2.1 Chirped Pulse Amplification.....	25
3.2.2 Laser Oscillator .....	26
3.2.3 Pulse Stretcher.....	26
3.2.4 Laser Amplifier .....	27
3.2.5 Pulse Compressor.....	27
3.2.6 Wave Plate .....	27

3.2.6.1 Operating principle of wave plates.....	28
3.2.6.2 Using a wave plate .....	28
3.2.6.3 Half-wave .....	29
3.2.6.4 Quarter-wave .....	30
3.2.6.5 Principles of polarizers with calcite (polarization-dependent refraction-glan laser calcite polarizer .....	31
3.3 $\lambda$ For 515 nm.....	33
3.4 $\lambda$ For 1030 nm.....	35
3.5 Optical Lenses .....	36
3.6 Focal Length.....	36
3.7 Focal Length Of A Curved Mirror .....	37
3.8 Achievable Beam Waist Radius .....	37
3.9 Surface Characteristics .....	38
3.10 Substrate .....	38
3.11 Experimental Parameters.....	38
<b>4. EXPERIMENTS AND RESULT DISCUSSION .....</b>	<b>41</b>
4.1 Focus Calibration.....	41
4.2 First Laser Pulses.....	41
4.2.1 Spot Shots.....	42
4.3 Cavities .....	44
4.4 Analysis Of Change In Frequency .....	47
4.5 Ripple Spacing.....	51
4.6 Effects Of Polarization .....	53
4.7 Effects Of Scan Speed .....	54
4.8 Hole Drilling Adjustments .....	58
4.9 Hole Micromilling With 90° Polarization Angle At 25.4 mm Focal Length ...	62
4.10 Passover Studies With Differing Polarization Angles.....	66
4.11 Scan Speed And Energy Level Tests With 25.4 mm Focal Length .....	70
4.12 Melting And Ablation Threshold .....	73
4.13 The Effects of Scan Speed / Cycle-Passover / Pulse Amount On Ripple Formation At Threshold Fluence Levels.....	78
4.14 Wider Cavity Micromachining.....	87
4.15 Effects Of Energy And Fluence On Wider Cavity Micromachining With 50 mm Lens .....	90
4.16 Effects Of Energy And Fluence On Wider Cavity Micromachining With 100 mm Lens .....	95
4.17 Further Experimentation With 100 mm Lens.....	95
4.18 Dumbbell Like Structures.....	98
4.19 Ablation In Both X And Y Directions With Fixed Polarization Angle And Creating Dumbbell Like Shaped Channels .....	99
4.20 Polarization Vs. Scanning Direction X- Y- XY .....	102
4.21 Surface Characteristics In Both X And Y Directions (Letter M).....	105
<b>5. CONCLUSION.....</b>	<b>109</b>
<b>REFERENCES.....</b>	<b>111</b>

## **ABBREVIATIONS**

<b>FS</b>	: Femtosecond
<b>NS</b>	: Nanosecond
<b>PS</b>	: Picosecond
<b>MPE</b>	: Multi-Photon Excitation
<b>HAZ</b>	: Heat Affected Zone
<b>SEM</b>	: Scanning Electron Microscope



## LIST OF TABLES

	<u>Page</u>
<b>Table 1</b> Fluence Threshold compilation for silicon ablation [34].....	15
<b>Table 2</b> Comparison between the parameters estimated from the current and the literature values.....	22
<b>Table 3</b> Thorlabs Broadband Dielectric Mirror Specifications [54]. .....	32
<b>Table 4</b> Mirror specifications [54].....	36
<b>Table 5</b> E02 and E03 mirror specifications [54]. .....	36
<b>Table 6</b> Optical camera images of Si-Wafer irradiated with differing fluence levels and number of pulses. ....	42
<b>Table 7</b> Experiment statistics for pulse shots with varying number of pulses power and fluence. ....	43
<b>Table 8</b> Statistical results on the first experiment .....	46
<b>Table 9</b> Statistical results on the second experiment.....	49
<b>Table 10</b> Statistical results of ripple spacing.....	52
<b>Table 11</b> Effects of polarizer angle on surface structures. ....	52
<b>Table 12</b> Scan speed comparisons for differing energy fluence and power ranges. .	55
<b>Table 13</b> Detailed statistics for holes drilled at experiment 7 .....	60
<b>Table 14</b> Parameters and results for the twenty one holes drilled with differing energy and fluence ratings. ....	63
<b>Table 15</b> Effects of passover with differentiating polarizer Angles.....	67
<b>Table 16</b> Statistics of the experiments run to test the effectiveness of 25 mm Focal Length Lens. ....	71
<b>Table 17</b> Statistical data driven from the first cavities of 8 different sets of experiments. ....	75
<b>Table 18</b> Detailed comparisons for scan speed, cycles, and amount of pulses. ....	79
<b>Table 19</b> Statistics of cavities without ripples.....	83
<b>Table 20</b> Parameters and resulting beam diameters for this experiment.....	88
<b>Table 21</b> Effects of scan speed and fluence on cavity depth and width, using a 50 mm Lens .....	91
<b>Table 22</b> f=100mm focal length lens is used to try and achieve wider cavity widths and depths .....	94
<b>Table 23</b> 100mm Focal Length Lens cavity width tests.....	97
<b>Table 24</b> Parameters used to machine the above imaged surfaces.....	105



## LIST OF FIGURES

	<u>Page</u>
<b>Figure 1.1</b> The electromagnetic spectrum (Picture Courtesy of Westinghouse Research Laboratories) reference. ....	2
<b>Figure 2.1</b> Phases of modification during Femtosecond micromachining of silicon [24] .....	5
<b>Figure 2.2</b> (a) Comparison of increase in laser power to drilling depth. , (b) Comparison of increase in scan speed to drilling depth.[28] .....	7
<b>Figure 2.3</b> Effects of Scan Speed on the maximum channel length [7]. ....	7
<b>Figure 2.4</b> The relation between scan speed and cavity diameter, where higher scan speeds reduce the overlapping of holes [32]. ....	8
<b>Figure 2.5</b> (a) Pulse duration vs Crater depth with 620 nm at 0.6 J/cm <sup>2</sup> [34]. (b) Pulse duration vs. Crater depth with 800 nm at 0.7J /cm <sup>2</sup> [34]. ....	9
<b>Figure 2.6</b> Comparison of cavity profiles with different repetition rates causing overlapping pulses [30]. ....	10
<b>Figure 2.7</b> Numerical simulation showing the effect of number of pulses on a silicon target. 10,50,80 and 100 pulses from top to bottom. With velocity compositions on the right side [39]. ....	10
<b>Figure 2.8</b> Effects of laser power on depth, a. 1.0mW b.1.5mW and c.2.5mW. d shows the top view of the drilled hole to show laser powers effect on the diameter of the drilled hole.[28] .....	11
<b>Figure2.9</b> SEM images of the Silicon(100) surface showing directional differences at different polarization types (a and b in SF <sub>6</sub> , and c and d in N <sub>2</sub> ambient gasses[25]. ....	12
<b>Figure 2.10</b> Effects of horizontal polarized pulses on Si-Wafer[31]. ....	13
<b>Figure 2.11</b> Increase in crystallization dependant on laser peak fluence.[42] .....	14
<b>Figure 2.12</b> Si(111) material timeline of exposure to 130fs, 620nm pulses [41, 45, 46]. ....	15
<b>Figure 2.13</b> Ablation rate for 20 holes drilled with 700 nm, 150 fs pulse with a focal length of 400 mm [56]. ....	18
<b>Figure 2.14</b> Electron mean free path vs. electron kinetic energy. Shaded area is the typical kinetic energies in the presented situation [57] .....	19
<b>Figure 2.15</b> Ripple direction is affiliated with the polarization angle. At 0° polarization angle the ripples are perpendicular to the scanning direction, while at 90° polarization angle the ripples are parallel to the scanning direction [24]. ....	19
<b>Figure 2.16</b> SEM Micrographs of single-shot ablation craters showing characteristic patterns $F = 0.63 \text{ J/cm}^2$ , (b) $F=3.3 \text{ J/cm}^2$ , (c) $F=12.5 \text{ J/cm}^2$ , (d) $F=25 \text{ J/cm}^2$ , $F=125 \text{ J/cm}^2$ , (f) $F=250 \text{ J/cm}^2$ [8]. ....	22
<b>Figure 3.1</b> Oscillator, stretcher, amplifier and compressor [2]. ....	26
<b>Figure 3.2</b> Schematic drawing for pulse stretcher includes two diffraction gratings [2]. ....	27
<b>Figure 3.3</b> Drawing of Laser Amplifier [2]. ....	28

<b>Figure 3.4</b> Half Plate representation [54].	29
<b>Figure 3.5</b> Wave Plate operating mechanisms [54].	30
<b>Figure 3.6</b> Quarter Wave representation [54].	31
<b>Figure 3.7</b> Drawing of polarizer [54].	32
<b>Figure 3.8</b> Setup for achieving 515nm wavelength.	33
<b>Figure 3.9</b> 0° E02 mirror coating, reflectivity vs. wavelength [54].	34
<b>Figure 3.10</b> The process for creating a photon of 1030nm	34
<b>Figure 3.11</b> 0° E03 mirror coating, reflectivity vs. wavelength [54].	35
<b>Figure 3.12</b> Focal length of focusing and defocusing lenses. [54].	37
<b>Figure 4.1</b> Distance between overlapping pulses	45
<b>Figure 4.2</b> Distance and time interval for five consecutive Femtosecond shots	45
<b>Figure 4.3</b> Cavity images showing the formation of ripple like structures. The values are: (a) Focal Length 15 mm, Fluence 0.506 J/cm <sup>2</sup> , Polarization Angle 0°, Frequency 1 kHz, Scan Speed 1250 (b) Focal Length 15 mm, Fluence 1.506 J/cm <sup>2</sup> , Polarization Angle 0°, Frequency 1 kHz, Scan Speed 1250 (c) Focal Length 15 mm, Fluence 0.506 J/cm <sup>2</sup> , Polarization Angle 0°, Frequency 1 kHz, Scan Speed 1250	46
<b>Figure 4.4</b> Comparison of Actual Cavity Diameter, Ripple Width and Spacing for 1 kHz and 0.1 kHz Frequency, and 1250 μm/s and 125 μm/s Scan Speeds. Focal Length: 15 mm.	48
<b>Figure 4.5</b> SEM images of cavities 1 to 6 from experiments 3 and 4 // (a) F.Length 15 mm, Fluence 1.69 J/cm <sup>2</sup> , P.Angle 0°, Fre. 1 kHz, S.Spd 1250, ripple w. 0.6 // (b) F.Length 15 mm, Fluence 1.69 J/cm <sup>2</sup> , P.Angle 0°, Fre. 1 kHz, S.Spd 1250, ripple w. 0.52 // (c) F.Length 15 mm, Fluence 1.69 J/cm <sup>2</sup> , P.Angle 0°, Fre. 1 kHz, S.Spd 1250, ripple w. 0.7 // (d) F.Length 15 mm, Fluence 16.9 J/cm <sup>2</sup> , P.Angle 0°, Fre. 0.1 kHz, S.Spd 125, ripple w. 0.58 // (e) F.Length 15 mm, Fluence 16.9 J/cm <sup>2</sup> , P.Angle 0°, Fre. 0.1 kHz, S.Spd 125, ripple w. 0.47 // (f) F.Length 15 mm, Fluence 16.9 J/cm <sup>2</sup> , P.Angle 0°, Fre. 0.1 kHz, S.Spd 125, ripple w. 0.62	50
<b>Figure 4.6</b> Effects of polarizer angle on surface formations.(a) Focal Length 15 mm, Fluence 4.21 J/cm <sup>2</sup> , Polarizer Angle 0°, Frequency 1 kHz, Scan Speed 1000. SEM magnification at 5.0k. (b) Focal Length 15 mm, Fluence 4.21 J/cm <sup>2</sup> , Polarizer Angle 90°, Frequency 1 kHz, Scan Speed 1000, SEM magnification at 2.5k	53
<b>Figure 4.7</b> Graph showing the effects of scan speed energy and fluence on cavity depth.	56
<b>Figure 4.8</b> Actual Cavity Diameter, Ripple Width and Spacing compared for 1000 μm/s and 1500μm/s scan speeds. Focal Length: 15 mm.	56
<b>Figure 4.9</b> Sem images of cavities 2 through 5 for cavity depth comparison at 1000 scan speed. The values for ripple spacing on these images were approximated. (a) Focal Length 15 mm, Fluence 4.21 J/cm <sup>2</sup> , magnification 2.5k Polarizer Angle 90°, Frequency 1 kHz, Scan Speed 1000, (b) Focal Length 15 mm, Fluence 8.43 J/cm <sup>2</sup> , magnification 2.5k Polarizer Angle 90°, Frequency 1 kHz, Scan Speed 1000, (c) Focal Length 15 mm, Fluence 12.6 J/cm <sup>2</sup> , magnification 5.0k Polarizer Angle 90°, Frequency 1 kHz, Scan Speed 1000, (d) Focal Length 15 mm, Fluence 16.9 J/cm <sup>2</sup> , magnification 5.0k Polarizer Angle 90°, Frequency 1 kHz, Scan Speed 1000	57
<b>Figure 4.10</b> SEM images of cavities 6 through 9 for cavity depth comparison at 1500 scan speed. The values for ripple spacing on these images were	

approximated. (a) Focal Length 15 mm, Fluence  $4.21 \text{ J/cm}^2$ , Polarizer Angle  $90^\circ$ , Frequency 1kHz, Scan Speed 1500, (b) Focal Length 15 mm, Fluence  $8.43 \text{ J/cm}^2$ , Polarizer Angle  $90^\circ$ , Frequency 1kHz, Scan Speed 1500, (c) Focal Length 15 mm, Fluence  $12.6 \text{ J/cm}^2$ , Polarizer Angle  $90^\circ$ , Frequency 1kHz, Scan Speed 1500, (d) Focal Length 15 mm, Fluence  $16.9 \text{ J/cm}^2$ , Polarizer Angle  $90^\circ$ , Frequency 1kHz, Scan Speed 1500. .. 58

**Figure 4.11** Schematics of overlapping holes to create cavities. .... 59

**Figure 4.12** Sem images of holes drilled with different polarization angles (a) Focal Length 15 mm, Fluence  $8.43 \text{ J/cm}^2$ , Polarizer  $90^\circ$ , Frequency 1 kHz (b) Focal Length 15 mm, Fluence  $8.43 \text{ J/cm}^2$ , Polarizer  $90^\circ$ , Frequency 1 kHz (c) Focal Length 15 mm, Fluence  $8.43 \text{ J/cm}^2$ , Polarizer  $0^\circ$ , Frequency 1 kHz (d) Focal Length 15 mm, Fluence  $8.43 \text{ J/cm}^2$ , Polarizer  $0^\circ$ , Frequency 1 kHz, (e) Focal Length 15 mm, Fluence  $8.43 \text{ J/cm}^2$ , Polarizer  $0^\circ$ , Frequency 1 kHz, (f) Focal Length 15 mm, Fluence  $8.43 \text{ J/cm}^2$ , Polarizer  $90^\circ$ , Frequency 1 kHz ..... 61

**Figure 4.13** Comparison of Actual Cavity Diameter and Desired Cavity Diameter 64

**Figure 4.14** Thumbnail images and statistics for the holes micromilled in this experiment. (a)Focal Length 25.4 mm, Fluence  $2.94 \text{ J/cm}^2$ , Polarization Angle  $90^\circ$ , Frequency 1 kHz (b) Focal Length 25.4 mm, Fluence  $0.881 \text{ J/cm}^2$ , Polarization Angle  $90^\circ$ , Frequency 1 kHz (c) Focal Length 25.4 mm, Fluence  $1.17 \text{ J/cm}^2$ , Polarization Angle  $90^\circ$ , Frequency 1 kHz (d) Focal Length 25.4 mm, Fluence  $2.35 \text{ J/cm}^2$ , Polarization Angle  $90^\circ$ , Frequency 1 kHz (e) Focal Length 25.4 mm, Fluence  $5.87 \text{ J/cm}^2$ , Polarization Angle  $90^\circ$ , Frequency 1 kHz (f) Focal Length 25.4 mm, Fluence  $4.41 \text{ J/cm}^2$ , Polarization Angle  $90^\circ$ , Frequency 1 kHz (g) Focal Length 25.4 mm, Fluence  $5.29 \text{ J/cm}^2$ , Polarization Angle  $90^\circ$ , Frequency 1 kHz (h) Focal Length 25.4 mm, Fluence  $0.441 \text{ J/cm}^2$ , Polarization Angle  $90^\circ$ , Frequency 1 kHz (i) Focal Length 25.4 mm, Fluence  $0.441 \text{ J/cm}^2$ , Polarization Angle  $90^\circ$ , Frequency 1 kHz (j) Focal Length 25.4 mm, Fluence  $0.441 \text{ J/cm}^2$ , Polarization Angle  $90^\circ$ , Frequency 1 kHz (k) Focal Length 25.4 mm, Fluence  $0.587 \text{ J/cm}^2$ , Polarization Angle  $90^\circ$ , Frequency 1 kHz (l) Focal Length 25.4 mm, Fluence  $0.294 \text{ J/cm}^2$ , Polarization Angle  $90^\circ$ , Frequency 1 kHz..... 65

**Figure 4.15** Comparison of Actual Cavity Diameters on various pulses at  $0^\circ$  and  $90^\circ$  polarization. Focal Length: 15 mm. Scan speed is fixed to  $3000 \text{ } \mu\text{m/s}$  and fluence to  $8.43 \text{ J/cm}^2$ . .... 66

**Figure 4.16** (a) Focal Length 15 mm, Fluence  $8.43 \text{ J/cm}^2$ , Polarization Angle  $90^\circ$ , Frequency 1 kHz, Scan Speed 3000, (b) Focal Length 15 mm, Fluence  $8.43 \text{ J/cm}^2$ , Polarization Angle  $90^\circ$ , Frequency 1 kHz, Scan Speed 3000, (c) Focal Length 15 mm, Fluence  $8.43 \text{ J/cm}^2$ , Polarization Angle  $90^\circ$ , Frequency 1 kHz, Scan Speed 3000, (d) Focal Length 15 mm, Fluence  $8.43 \text{ J/cm}^2$ , Polarization Angle  $0^\circ$ , Frequency 1 kHz, Scan Speed 3000, (e) Focal Length 15 mm, Fluence  $8.43 \text{ J/cm}^2$ , Polarization Angle  $0^\circ$ , Frequency 1 kHz, Scan Speed 3000, (f) Focal Length 15 mm, Fluence  $8.43 \text{ J/cm}^2$ , Polarization Angle  $0^\circ$ , Frequency 1 kHz, Scan Speed 3000 68

**Figure 4.17** SEM images of the resulting cavities, with Actual Cavity Diameter values. (g) Focal Length 15 mm, Fluence  $8.43 \text{ J/cm}^2$ , Polarization Angle  $0^\circ$ , Frequency 1 kHz, Scan Speed 3000, (h) Focal Length 15 mm, Fluence  $8.43 \text{ J/cm}^2$ , Polarization Angle  $0^\circ$ , Frequency 1 kHz, Scan Speed 3000, (i) Focal Length 15 mm, Fluence  $8.43 \text{ J/cm}^2$ , Polarization

	Angle 90 °, Frequency 1 kHz, Scan Speed 2000, (j) Focal Length 15 mm, Fluence 8.43 J/cm <sup>2</sup> , Polarization Angle 90 °, Frequency 1 kHz, Scan Speed 3000, (k) Focal Length 15 mm, Fluence 8.43 J/cm <sup>2</sup> , Polarization Angle 90 °, Frequency 1 kHz, Scan Speed 3000, (l) Focal Length 15 mm, Fluence 8.43 J/cm <sup>2</sup> , Polarization Angle 90 °, Frequency 1 kHz, Scan Speed 3000 .....	69
<b>Figure 4.18</b>	Fluence versus Actual Cavity Diameter Graph. Pulses are 10000 and 20000. Focal Length: 25.4 mm. ....	72
<b>Figure 4.19</b>	Collective SEM images of cavities micromachined with 25.4 mm Focal Length Lens. (a) Focal Length 25.4 mm, Fluence 8.43 J/cm <sup>2</sup> , Polarization Angle 90 °, Frequency 1 kHz, Scan Speed 100, (b) Focal Length 25.4 mm, Fluence 1.69 J/cm <sup>2</sup> , Polarization Angle 90 °, Frequency 1 kHz, Scan Speed 100, (c) Focal Length 25.4 mm, Fluence 12.29 J/cm <sup>2</sup> , Polarization Angle 90 °, Frequency 1 kHz, Scan Speed 200 .....	73
<b>Figure 4.20</b>	SEM images of resulting cavities (a), Focal Length 15 mm, Fluence 0.16 J/cm <sup>2</sup> , Polarization Angle 90 °, Frequency 1kHz, Scan Speed 10 (b) Focal Length 15 mm, Fluence 0.211 J/cm <sup>2</sup> , Polarization Angle 90 °, Frequency 1 kHz, Scan Speed 10 (c) Focal Length 15 mm, Fluence 0.337 J/cm <sup>2</sup> , Polarization Angle 90 °, Frequency 1 kHz, Scan Speed 10 (d) Focal Length 15 mm, Fluence 0.843 J/cm <sup>2</sup> , Polarization Angle 90 °, Frequency 1 kHz, Scan Speed 10, (e) Focal Length 15 mm, Fluence 0.843 J/cm <sup>2</sup> , Polarization Angle 90 °, Frequency 1 kHz, Scan Speed 10 , (f)Focal Length 15 mm, Fluence 0.421 J/cm <sup>2</sup> , Polarization Angle 90 , Frequency 1 kHz, Scan Speed 10 .....	76
<b>Figure 4.21</b>	Microstructures formed on SI-Wafer surface at threshold values. ....	77
<b>Figure 4.22</b>	Actual Cavity Diameter, Ripple Spacing and Width comparisons for different fluence, scan speed and numbers of pulses for the first 12 cavities. Focal Length: 15 mm. ....	78
<b>Figure 4.23</b>	(a), Focal Length 15 mm, Fluence 0.16 J/cm <sup>2</sup> , Polarization Angle 90 °, Frequency 1kHz, Scan Speed 10 , (b) Focal Length 15 mm, Fluence 0.16 J/cm <sup>2</sup> , Polarization Angle 90 °, Frequency 1kHz , Scan Speed 50, (c) Focal Length 15 mm, Fluence 0.16 J/cm <sup>2</sup> , Polarization Angle 90 °, Frequency 1 kHz, Scan Speed 100, (d) Focal Length 15 mm, Fluence 0.16 J/cm <sup>2</sup> , Polarization Angle 90 °, Frequency 1 kHz, Scan Speed 500, (e) Focal Length 15 mm, Fluence 0.211 J/cm <sup>2</sup> , Polarization Angle 90 °, Frequency 1 kHz, Scan Speed 10, (f) Focal Length 15 mm, Fluence 0.211 J/cm <sup>2</sup> , Polarization Angle 90 °, Frequency 1 kHz, Scan Speed 50	81
<b>Figure 4.24</b>	SEM images of the first 12 cavities, with ripple formations (a) Focal Length 15 mm, Fluence 0.211 J/cm <sup>2</sup> , Polarization Angle 90 °, Frequency 1 kHz, Scan Speed 100, (b) Focal Length 15 mm, Fluence 0.211 J/cm <sup>2</sup> , Polarization Angle 90, Frequency 1 kHz, Scan Speed 500, (c) Focal Length 15 mm, Fluence 0.337 J/cm <sup>2</sup> , Polarization Angle 90 °, Frequency 1 kHz, Scan Speed 10, (d) Focal Length 15 mm, Fluence (J/cm <sup>2</sup> ) 0.337, Polarization Angle 90 °, Frequency 1 kHz, Scan Speed 50, (e) Focal Length 15 mm, Fluence 0.337 J/cm <sup>2</sup> , Polarization Angle 90 °, Frequency 1 kHz, Scan Speed 100, (f) Focal Length 15 mm, Fluence 0.337 J/cm <sup>2</sup> , Polarization Angle 90 °, Frequency 1 kHz, Scan Speed 500 .....	82
<b>Figure 4.25</b>	(a) Focal Length 15 mm, Fluence 0.843 J/cm <sup>2</sup> , Polarization Angle 90 °, Frequency 1 kHz, Scan Speed 10, (b) Focal Length 15 mm, Fluence	

- 0.843 J/cm<sup>2</sup>, Polarization Angle 90 °, Frequency 1 kHz, Scan Speed 50, (c) Focal Length 15 mm, Fluence 0.843 J/cm<sup>2</sup>, Polarization Angle 90 °, Frequency 1 kHz, Scan Speed 100, (d) Focal Length 15 mm, Fluence 0.843 J/cm<sup>2</sup>, Polarization Angle 90 °, Frequency 1 kHz, Scan Speed 100, (e) Focal Length 15 mm, Fluence 0.843 J/cm<sup>2</sup>, Polarization Angle 90 °, Frequency 1 kHz, Scan Speed 100, (f) Focal Length 15 mm, Fluence 0.843 J/cm<sup>2</sup>, Polarization Angle 90 °, Frequency 1 kHz, Scan Speed 10084
- Figure 4.26** SEM images of cavities drilled for this experiment. (a) Focal Length 15 mm, Fluence 0.211 J/cm<sup>2</sup>, Polarization (b) Frequency 1 kHz, Scan Speed 50, (c) Focal Length 15 mm, Fluence 0.211 J/cm<sup>2</sup>, Polarization Angle 90 °, Frequency 1 kHz, Scan Speed 50, (d) Focal Length 15 mm, Fluence 0.843 J/cm<sup>2</sup>, Polarization Angle 90 °, Frequency 1 kHz, Scan Speed 1085
- Figure 4.27** SEM images of some of the cavities from Figure 4.25 at a 45° angle. The 2<sup>nd</sup> and 3<sup>rd</sup> images are of the deeper cavities. (a) Focal Length 15mm, Fluence 0.16 J/cm<sup>2</sup>, Polarization Angle 90°, Frequency 1 kHz, Scan Speed 10, 50 and 100 respectively, (b) Focal Length 15mm, Fluence 0.421 J/cm<sup>2</sup>, Polarization Angle 90°, Frequency 1 kHz, Scan Speed 50 μm/s, (c) Focal Length 15mm, Fluence 0.843 J/cm<sup>2</sup>, Polarization Angle 90°, Frequency 1 kHz, Scan Speed 50 μm/s ..... 86
- Figure 4.28** SEM images for cavities created using a 100 mm Focal Length lens. (a) Focal Length 100 mm, Fluence 4.17 J/cm<sup>2</sup>, Polarization Angle 90 °, Frequency 1 kHz, Scan Speed 1000, (b) Focal Length 100 mm, Fluence 4.17 J/cm<sup>2</sup>, Polarization Angle 90 °, Frequency 1 kHz, Scan Speed 1000, (c) Focal Length 100 mm, Fluence 1.9 J/cm<sup>2</sup>, Polarization Angle 90 °, Frequency 1 kHz, Scan Speed 1000, (d) Focal Length 100 mm, Fluence 1.52 J/cm<sup>2</sup>, Polarization Angle 90 °, Frequency 1 kHz, Scan Speed 1000, (e) Focal Length 100 mm, Fluence 0.948 J/cm<sup>2</sup>, Polarization Angle 90 °, Frequency 1 kHz, Scan Speed 1000..... 89
- Figure 4.29** Graph comparing the cavity width at differing Pulse Amount Coefficients, which equals Passovers/Scan Speed . Focal Length: 50 mm.92
- Figure 4.30** Cross-Sectional SEM images showing changes in cavity width and depth at focal length 50 mm. (a) Focal Length 50 mm, Fluence 16.7 J/cm<sup>2</sup>, Polarization Angle 90 °, Frequency 1 kHz, Scan Speed 5, (b) Focal Length 50 mm, Fluence 16.7 J/cm<sup>2</sup>, Polarization Angle 90 °, Frequency 1 kHz, Scan Speed 10, (c) Focal Length 50 mm, Fluence 16.7 J/cm<sup>2</sup>, Polarization Angle 90 °, Frequency 1 kHz, Scan Speed 10, (d) Focal Length 50 mm, Fluence 16.7 J/cm<sup>2</sup>, Polarization Angle 90 °, Frequency 1 kHz, Scan Speed 5..... 93
- Figure 4.31** Comparison of cavity depth and Actual Cavity Diameter to cycles. Focal Length: 100 mm. .... 95
- Figure 4.32** SEM cross-sectional images of cavities drilled with 100 mm focal length lens. (a) Focal Length 100 mm, Fluence 4.26 J/cm<sup>2</sup>, Pol.n Angle 90 °, Frequency 1 kHz, Scan Speed 5, (b) Focal Length 100 mm, Fluence 4.26 J/cm<sup>2</sup>, Pol. Angle 90 °, Frequency 1 kHz, Scan Speed 5 (c) Focal Length 100 mm, Fluence 4.26 J/cm<sup>2</sup>, Pol.Angle 90 °, Frequency 1 kHz, Scan Speed 5 ..... 96
- Figure 4.33** Parameter details per cavity for 100 mm Focal Length Tests. (a) Focal Length 100 mm, Fluence 2.84 J/cm<sup>2</sup>, Polarization Angle 90 °, Frequency 1 kHz, Scan Speed 1, (b) Focal Length 100 mm, Fluence 1.9 J/cm<sup>2</sup>, Polarization Angle 90 °, Frequency 1 kHz, Scan Speed 1, (c)

	Focal Length 100 mm, Fluence 4.17 J/cm <sup>2</sup> , Polarization Angle 90 °, Frequency 1 kHz, Scan Speed 1.....	98
<b>Figure 4.34</b>	Shape of the desired dumbbell like formation .....	99
<b>Figure 4.35</b>	Dumbbell shape statistics and resulting SEM image for 60 mW. ....	100
<b>Figure 4.36</b>	Dumbbell shape statistics and resulting SEM image for 100 mW. ....	100
<b>Figure 4.37</b>	Dumbbell shape statistics and resulting SEM image for 170 mW. ....	101
<b>Figure 4.38</b>	Dumbbell shape statistics and resulting SEM images for 200 mW.....	101
<b>Figure 4.39</b>	Methodology for creating overlapping cavities. ....	103
<b>Figure 4.40</b>	(a) Stage Direction y, Polarization: 90, Power: 228 mW, Fluence: 27.1 J/cm <sup>2</sup> F: 50mm, V: 0.05 mm/s, (b) Stage Direction , Polarization: 90, Power: 228 mW, Fluence: 27.1 J/cm <sup>2</sup> , F: 50mm ,V: 0.05 mm/s, (c) Stage Direction xy, Polarization: 90, Power: 228 mW,Fluence: 27.1 J/cm <sup>2</sup> , F: 50mm,V: 0.05 mm/s .....	104
<b>Figure 4.41</b>	Experiment guidance schematics.....	106
<b>Figure 4.42</b>	Actual Cavity Diameter to Scanning Direction comparisons, polarization angle of 90° is used. ....	107
<b>Figure 4.43</b>	Power: 230 mW, ScanSpeed:0.005 mm/s, Fluence: 17.4 j/cm <sup>2</sup> , Focal Length: 50 mm, Desired Cavity Diameter: 40.8 mm .....	108

## **FEMTOSECOND LASER MICROMACHINING OF SI-WAFER**

### **SUMMARY**

As technology advanced with the principle, the mystery is hidden in the details, it carried itself from macro to micro and nano dimensions. This situation has pushed us from using macro development equipment to much more accurate equipment to work in micro, nano or even smaller measures.

Lasers are one of the few equipments that are able to work perfectly in these smaller dimensions. After using nanosecond lasers to produce micro materials for so long the humans natural instinct to always better themselves has passed the technology grade to femtosecond lasers.

Micromachining with femtosecond lasers has lately become more and more popular. The reason for this popularity is because the femtosecond lasers are able to send photon shots faster than the duration defined in the thermal diffusion law. Thus the micro machining process was over before heat was able to spread and damage the material. This concession of the femtosecond laser ensures a lot of advantage against it's adversaries, especially on micro materials. But this advantage isn't true for all situations. To benefit from this advantage the energy flow rating which derives from the photon shots of the laser must be between the melting and ablation thresholds of the chosen material.

During experimentation the melting and ablation thresholds of the si-wafer and the parameters to micromachine the desired cavity depth with the best surface characteristics was studied. An characterisation table showing the required parameters such as energy, frequency, number of shots and their actions and reactions to micromachine si-wafers with femtosecond lasers was formed. This characterisation table was used as a guide while micromachining si-wafers with the femtosecond laser.



## FEMTOSANIYE LAZER İLE Sİ-PLAKA ÜZERİNE MİKRO ÖLÇEKTE BİÇİMLENDİRME

### ÖZET

Teknoloji geliştikçe işin sırrı detaylarda saklıdır esasına dayanan bir ilke ile kendini makro boyuttan mikro ve nano boyuta taşıdı. Tabi bu durum bizi mikro teknoloji ile üretilen ürünlerin üretim yönteminde makro boyutlarda kullanılan aletlerden çok daha hassas yani mikro-nano hatta daha küçük mertebelerde kusursuz çalışan aletler arayışına itti.

Lazerler bu küçük mertebelerde kusursuz iş görebilen sayılı alet ve uygulama yöntemlerinden biriydi. Uzun süreler nanosaniye lazer kullanılarak yapılan mikro malzeme üretim işlemleri insanoğlunun kendini devamlı geliştirme dürtüsü ile yerini femtosaniye lazere bıraktı.

Femtosaniye lazer ile mikromalzeme işleme son dönemlerde gittikçe popüler hale geldi.

Bunun sebebi ise lazerin foton darbelerinin arasında geçen süresi termal difüzyon yasasına göre ısının yayılımından çok daha kısa zamanda gerçekleşmekte olması idi. Böylece ısı daha yayılıp malzemeye zarar vermeye başlamadan mikro malzeme üzerine uygulanan mikro işleme süreci çoktan bitmiş oluyordu. Femtosaniye lazerin bu ayrıcalığı, özellikle mikro malzeme gibi çok küçük hacimli malzemeler işlerken, rakiplerine göre çok büyük avantaj sağlamakta. Tabi bu avantaj her koşulda geçerli değil. Femtosaniye lazer ile mikromalzeme işlerken yöntemin avantajından yararlanmak için lazerlerden çıkan foton darbeleri kaynaklı olan enerji akışı değeri işlenen malzemenin melting eşiği ve ablasyon eşiği arasında tutulduğu sürece geçerli olmakta.

Yapılan deneylerde Si-Plakanın Ablation ve Melting Threshold değerlerinin bulunmalarının yanı sıra en düzgün yüzey karakteristiğine sahip ve istenilen derinlikteki kanalların açılması için gerekli diğer parametrelerin bulunmasına çalışıldı. Femtosaniye lazer ile işlenen si-plakasının gerekli parametreler, yani hangi enerji hangi frekans, hangi foton darbe sayısı kullanılarak nasıl tepki gösterdiğini anlatan bir etki tepki karakterizasyon tablosu çıkarıldı. Çıkarılan bu karakterizasyon tablosu femtosaniye ile si-plaka işleme sırasında bir rehber olarak kullanıldı.



## 1. INTRODUCTION

Laser is a consistent monochromatic beam of electromagnetic radiation. Laser wavelengths range from infrared to ultraviolet[1]. Lasers are obtained by optical amplification of the stimulated emission of photons. The mentioned electromagnetic radiation is an energy form which shows wave like behavior while traveling through space.

### 1.1 Purpose Of The Thesis

The main objective of this thesis is to achieve the best micromachining parameters by changing and testing all of the laser parameters. These machined surfaces will in effect be used to create micro-fluidic channels.

### 1.2 Electromagnetic Spectrum

Ionizing and nonionizing radiation of varying frequencies and wavelengths form the electromagnetic spectrum as can be seen in **Figure 1.1**. It consists of all the possible frequencies of electromagnetic radiation. These waves are described by their frequency, wavelength or photon energy.

It has not been possible to explain the wave nature of the electromagnetic radiation. For this reason the quantum theory of electromagnetic radiation has been proposed. In this theory, the electromagnetic radiation is considered to be a stream of particles, which are called photons. Each of these photons is associated with an amount of energy proportional to its frequency. This photon energy is expressed in the formula below[1].

$$E = h\nu \tag{1}$$

In this equation  $h$  is the Planck constant ( $6.63 \times 10^{-34}$  J/s), and  $\nu$  represents frequency. Thus, electromagnetic radiation exhibits wave and particle natures. These theories of electromagnetic radiation are deemed complementary [2].

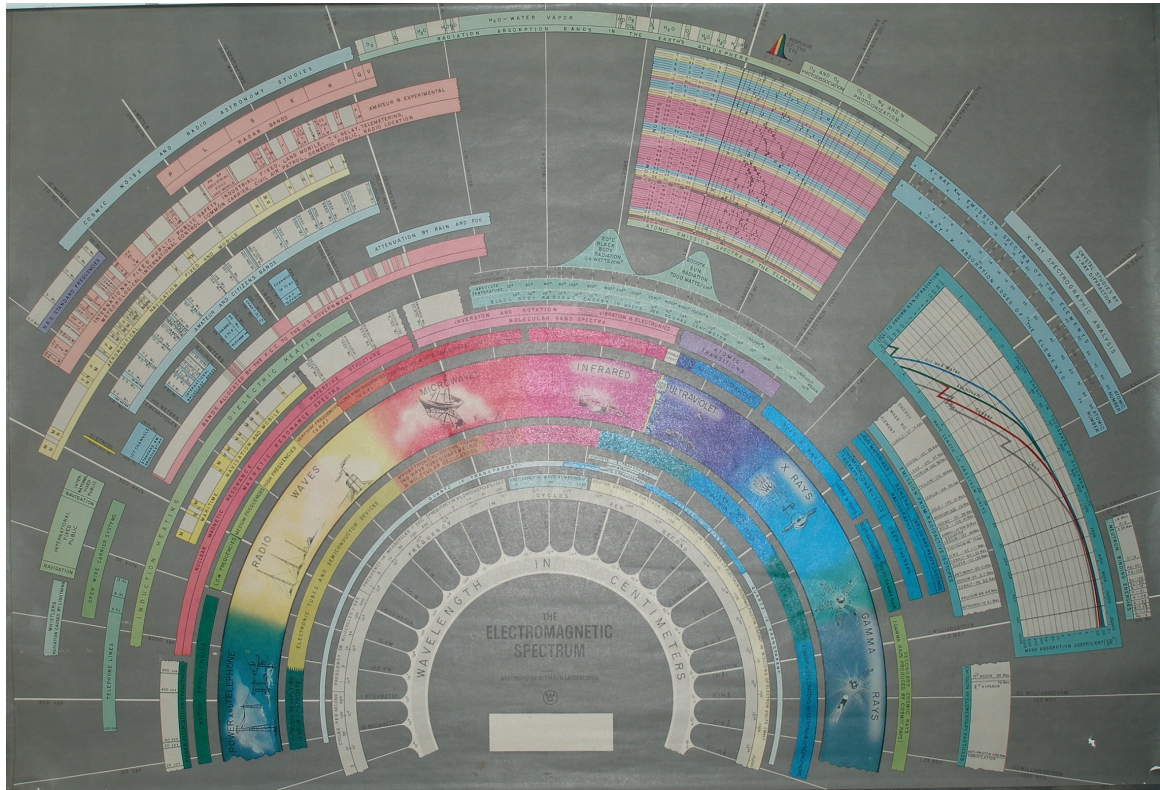


**Figure 1.1** The electromagnetic spectrum (Picture Courtesy of Westinghouse Research Laboratories) reference

### 1.3 Femtosecond Lasers

The Femtosecond Laser earns its name thanks to its ability to deliver laser pulses with durations between a few femtoseconds and hundreds of femtoseconds. 1fs (Femtosecond) =  $10^{-15}$ s. Femtosecond lasers belong to the ultrashort (sometimes also referred to as ultrafast [3, 4, 5, 6, 7] pulse laser category. Femtosecond lasers pulse duration is tuneable within a specific range. Femtosecond lasers discharge optical pulses in femtoseconds. It belongs to the ultra-short pulse laser category. Femtosecond lasers are used mainly in micro-machining, femto-chemistry, laser eye surgeries [8, 9] or other areas such as nano-particles [10] and nano-bump arrays creation. They are also used in other interesting areas such as optical communications [11]. But all femtosecond uses are expensive and complex to setup in general [12].

### 1.4 Femtosecond Laser Advantages Over Nanosecond Laser In Thermal Diffusion And Material Choices

The main attribute of femtosecond laser micromachining is the ultra short pulses used for the process. This results in minimal thermal and mechanical deformations

on the surface of the target material. Meanwhile nanosecond machining is bound by deformations caused to the surface of the material.

Femtosecond regime is also more versatile when it comes to choice of materials and types of material processing. Large variety of materials have been processed and experimented on with femtosecond lasers.

Furthermore it is known that nanosecond machining proceeds by deforming the surface of the material, resulting in unwanted surface deformations.

At low energy levels Femtosecond Lasers can cause melting, at higher energy levels ablation occurs [13]. Femtosecond lasers also provide lower ablation thresholds compared to nanosecond lasers [14]. It has also been proposed that processing femtosecond laser micromachining in ambient [15] atmospheric conditions would be useful for commercial applications [16]. Furthermore they are also used in structuring photovoltaic silicon cells in vacuum [17] environments [18].



## 2. FEMTOSECOND LASER MICROMACHINING

Laser machining is the process of removing materials from a substrate using focused laser pulses to create the desired features on it. The aim is to achieve these features with ultimately no deformations on the surface. Which in effect requires the perfection of the properties of the laser, the experimental setup and the substrate, in the right atmospheric conditions. These deformations are caused by the thermal diffusion of energy and Femtosecond Lasers are one step ahead at avoiding them with ultrashort pulse durations.

The results of a single shot to a silicon surface can be seen in **Figure 2.1**, ripples are not included in this presentation since they only occur with multiple shots.

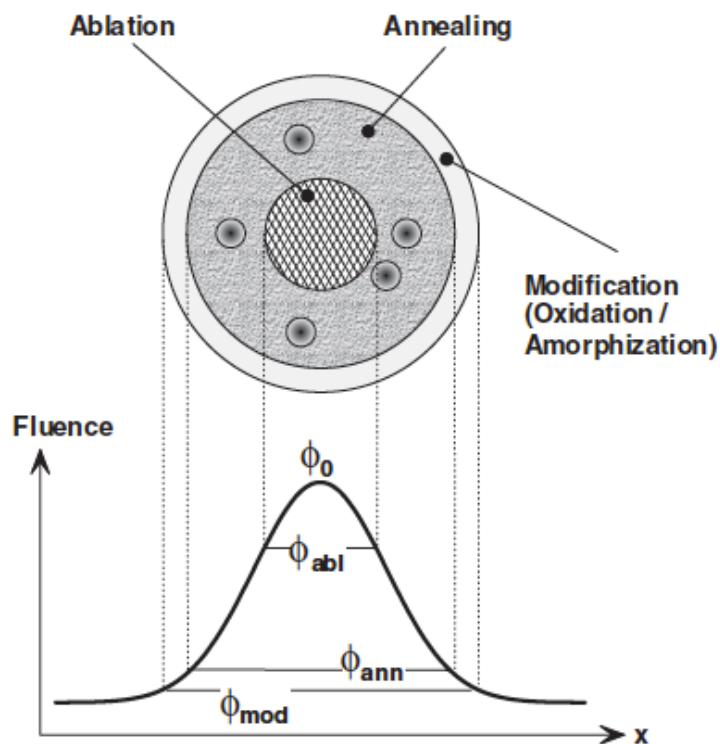


**Figure 2.1** Phases of modification during Femtosecond micromachining of silicon [24]

Much importance has been attached to laser-based machining of materials with femtosecond pulses recently [3, 13, 19, 20, 21, 22]. Thermal diffusion into surrounding material is limited by reduction of temporal width of pulses from the

nanosecond to the femtosecond regime during ablation process. This process increases the quality of the machined surface.

Through femtosecond laser-material interactions, only a small fraction of laser pulse energy is transmitted to the material surrounding the laser-irradiated area in the form of heat; in contrast to the material processing by using nanosecond or longer laser pulses where standard modes of thermal processes are domineering. As a result, non-thermal structural changes are induced by femtosecond laser pulses, which are caused by electronic excitation and associated nonlinear processes, before equilibrium is reached by the material lattice by the excited carriers. This short cut of material modification process can cause significant reduction in the thermal stresses with very little collateral damage of the materials processing [23].

## **2.1 Laser Properties and Their Effects On Micromachining**

The complexity of Femtosecond laser micromachining derives from the fact that there are many parameters appertaining to laser operation. Effects of these parameters are dependent on various factors, including but not solely based on, atmospheric effects [7, 16, 25, 26], material properties [27], types of appendages used for the laser.

Some of the adjustable properties of laser micromachining processes and their effects on materials are as below:

### **2.1.1 Scan speed**

Multiple holes were drilled on a 300  $\mu\text{m}$  thick silicon wafer with a 800 nm, 30 fs femtosecond laser with a repetition rate of 1 kHz to investigate the dependence of depth on laser power. The tests were run first with fixed scan speed and increasing laser power, then with fixed laser power and increasing scan speed [28].

The results of increasing the laser power increases the depth of the micromilled cavity as can be observed on **Figure 2.2(a)**. While increasing the scan speed in **Figure 2.2(b)** results in reduced depth of cavities [28].

In comparison while drilling channels instead of cavities, it is observed that lowering the scan speed can increase the length of the machined channel as can be observed on **Figure 2.3** [7].

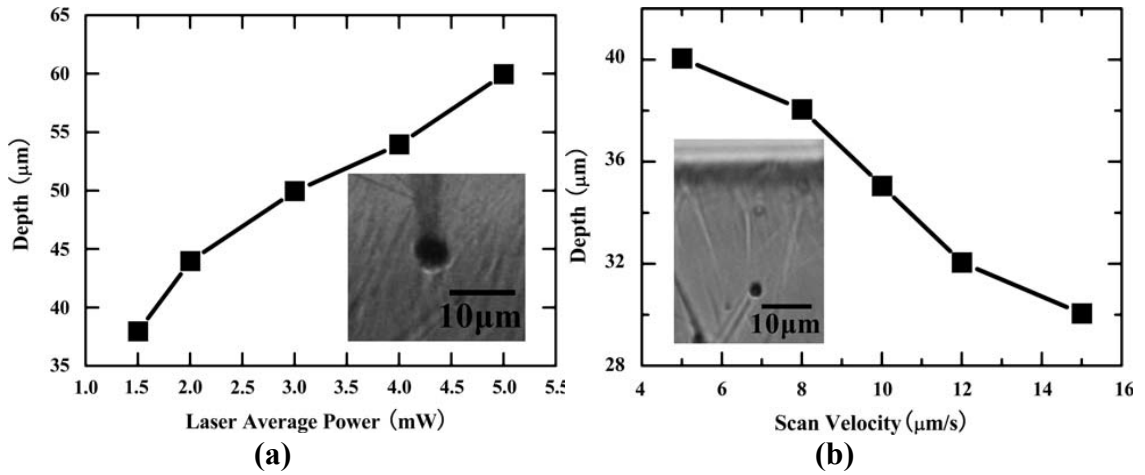


**Figure 2.2** (a) Comparison of increase in laser power to drilling depth. , (b) Comparison of increase in scan speed to drilling depth.[28]

However extremely low scan speeds can result in severely damaged surfaces because of the very high amount of pulses gathered on the ablated surface spot [29]. This can result in undesired surface morphologies.

Whereas at higher scan speeds, scattered irradiation and non irradiated areas can occur [3] This is due to the fact that as the scan speed rises the number of pulses hitting a given spot on the substrate is lowered, which in effect results in spots where pulses don't accumulate enough to start a thermal reaction.[30]

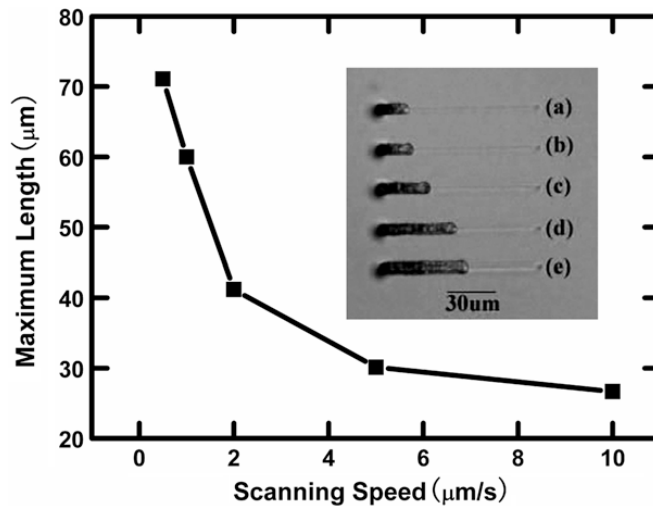


**Figure 2.3** Effects of Scan Speed on the maximum channel length [7].

In general decrease in scan speed causes more pulses to deposit in a unit area, thus intensifying the amount of surface modifications [31]. While increase in scan speed causes less amount of pulses to deposit in a unit area, thus causing minimal amount

of surface modifications. Ergo scan speed is taken into account where length depth and surface morphologies of cavities and micro-channels are concerned.

To set scan speed, the lowest value is where defects on surface morphology can be avoided and a smooth surface can be achieved. Whereas as **Figure 2.4** illustrates, highest value of scan speed is dependent on cavity diameter and depth, as setting the scan speed too high would result in non-overlapping (i.e. non continuous channels) pulses [32]. This also effects ripple formation, as the percentage of overlapping areas is increased above half the focus diameter, ripple spacing rises in conjunction [33].

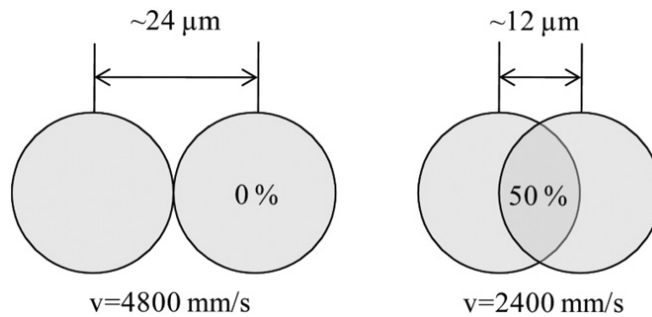


**Figure 2.4** The relation between scan speed and cavity diameter, where higher scan speeds reduce the overlapping of holes [32].

### 2.1.2 Cycle and passovers

Passover as the name suggests is a single pass over the cavity length, whereas cycle is a full round trip of laser over the desired cavity. It is then safe to state that Cycle and Passover relates to the same parameter of the micromachining property.

It has been observed that multiple Passovers over a Si-Wafer result in linearly deeper cavities. However the linearity is broken as surface deformations occur and further increase as the depth is increased even more [8, 32].

### 2.1.3 Pulse duration

It has been suggested that an increase in pulse duration causes an increase in cavity depth. This is based on the fact that light absorption increases with increasing pulse duration. The effects of this increase in depth can be observed in **Figure 2.5**. Increasing the pulse duration also increases the ablation threshold[9].

The effects of pulse duration at below melting threshold fluences was tested for metals. It has been observed for Ni that there is a surge of temperature at a pulse duration close to the electro-phonon relaxation time.[35]

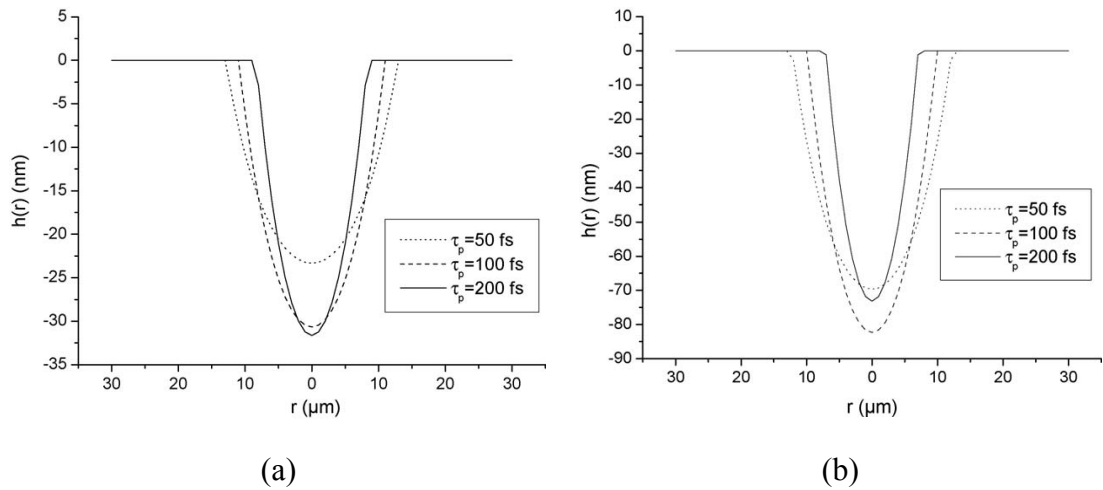


**Figure 2.5** (a) Pulse duration vs Crater depth with 620 nm at  $0.6 \text{ J/cm}^2$  [34]. (b) Pulse duration vs. Crater depth with 800 nm at  $0.7 \text{ J/cm}^2$  [34].

#### 2.1.4 Frequency (Repetition Rate)

Frequency or repetition rate is the number of pulses emitted by the laser source per second. Effects of repetition rate vary depending on adjustments on other laser properties. One such effect is that as the repetition rate increases threshold fluence decreases [36].

As can be observed in **Figure 2.6** femtosecond laser at 150fs pulses and 800 nm. wavelength with tripled frequency to obtain 266nm was used on silica glass in an argon environment to test the effects of repetition rate. A fixed scan speed of  $10 \mu\text{m/s}$  is used, when repetition rate is increased, pulse overlapping increases resulting in deeper cavities [30].

#### 2.1.5 Number of pulses

After each consecutive pulse delivered to the material, fractions are removed. The depth of the cavity increases with the number of pulses delivered [37].

Working with sub-picosecond pulses has been understood to reduce the thermal damage. This in turn lowers the pulse energy required for ablation. As a result the features of the laser-machined areas are improved.

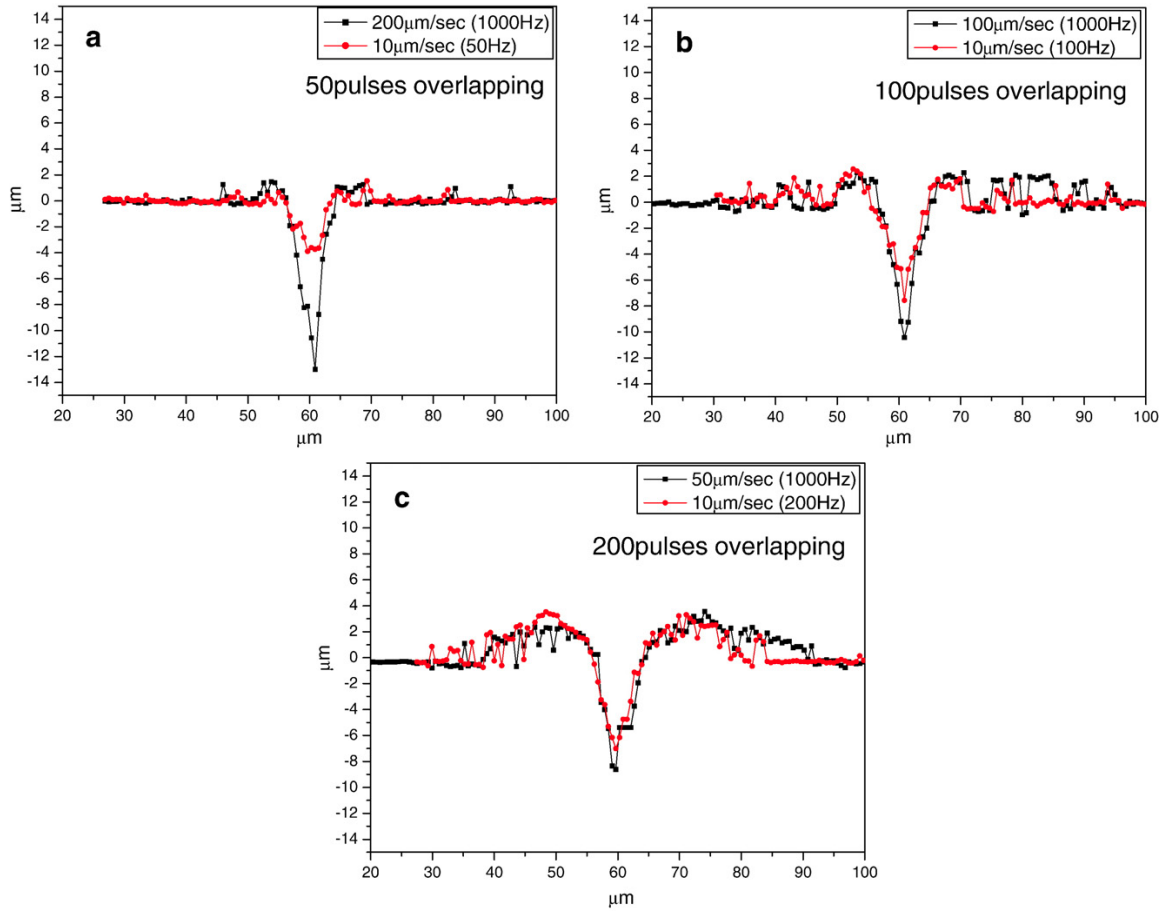


**Figure 2.6** Comparison of cavity profiles with different repetition rates causing overlapping pulses [30].

The high number of photons in any single pulse ensures a spatial distribution of energy at the material surface [38].

Dependence of changes in surface morphology on number of pulses was observed during ablation. The resulting graph of 10, 50, 80 and 100 laser pulses on silicon can be observed in **Figure 2.7** [39].

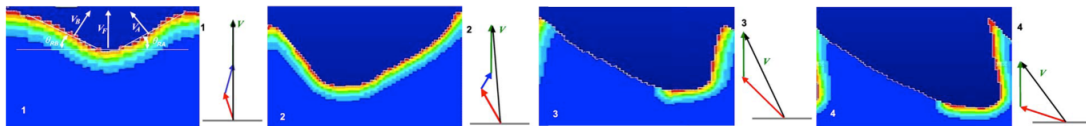


**Figure 2.7** Numerical simulation showing the effect of number of pulses on a silicon target. 10,50,80 and 100 pulses from top to bottom. With velocity compositions on the right side [39].

### 2.1.6 Energy / power

Increasing the energy of the laser, increases the depth and diameter of the generated cavity.

Effects of laser power on depth and various other attributes has been tested, using a 800nm, 30fs femtosecond laser with a repetition rate of 1kHz on a 300 $\mu$ m thick silicon wafer. The resulting effects of crater depth can be observed in **Figure 2.8**.

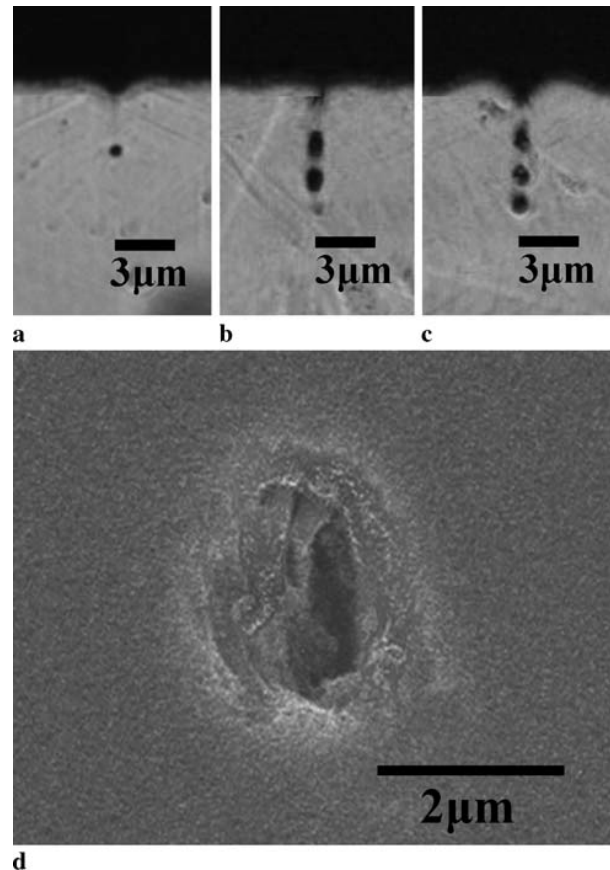


**Figure 2.8** Effects of laser power on depth, a 1.0 mW and c.25 mW d shows the top view of the drilled hole to show laser powers effect on the diameter of the drilled hole [28]

From 1.0mW to 2.5mW with 0.5mW increments. It has been observed that the increase in laser power directly affects the depth of the machined area. During this test it has also been observed that increase in power does not influence the diameter of the drilled holes[28].

A pyroelectric device is always used to measure the energy of a laser pulse (in joules, or usually microjoules) from either a single-shot or a high-repetition-rate system. In such a material a proportional electrical response is produced by an increase in the temperature [40].

Because of the energy deposited by the laser pulse in the material, this electrical response, generally a voltage, is directly proportional to the rise in temperature.

Overall absorbing power of the material, with or without an adequate coating is the primary drive for this thermal effect [40].

### 2.1.7 Electric field polarization

Effects of the polarization of laser beam on a silicon surface has been discussed. 350  $\mu\text{m}$  thick Si(100) wafers were structured using a 800 nm wavelength laser, with 120 fs pulses at  $1.0 \text{ J}/\text{cm}^2$  fluence in gaseous environments. Three types of polarized laser-beams were used (p-polarized, s-polarized and circular). The results show directional differences at various polarization types as can be observed in **Figure 2.9** [25].

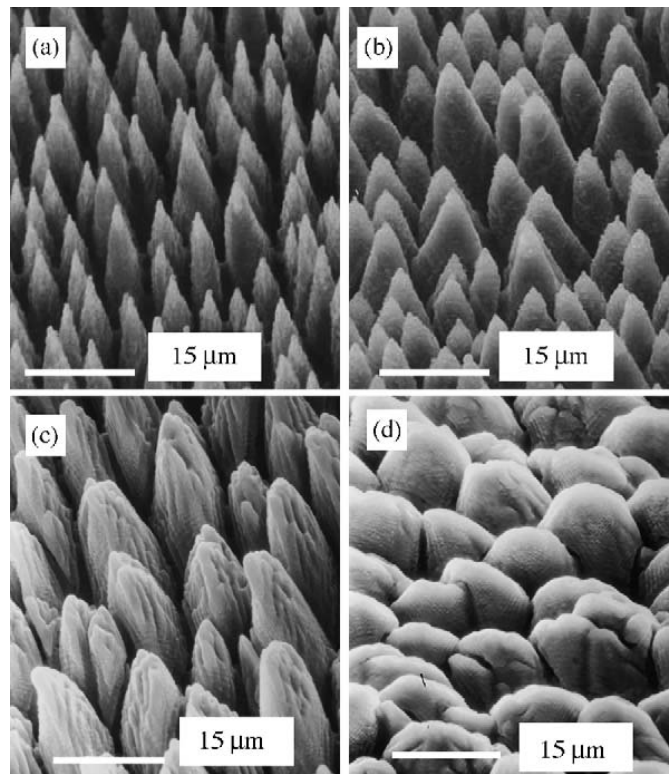


**Figure 2.9** SEM images of the Silicon (100) surface showing directional differences at different polarization types (a and b in  $\text{SF}_6$  and c and d in  $\text{N}_2$  ambient gasses) [25].

Further to above experiments, tests were run on a 400  $\mu\text{m}$  thick Si(100) wafer, with a Ti:sapphire amplifier, sending 800 nm wavelength, 30 fs pulses at a repetition rate of 1 kHz to see the difference in micro-mesoporous-structures formed on the surface of the material based on the polarization angle[31].

**Figure 2.10** shows the micrographs of surface microstructures ( $1 \times 1 \text{ mm}^2$ ) induced by horizontal polarized laser pulses, vertical laser pulses and  $45^\circ$  polarized pulses in air. When laser pulse energy is slightly exceeded the ablation threshold, the formed microstructures such as ripples were observed to be perpendicular to the polarization orientation of the laser pulses. But when the pulse energy was much higher than the ablation threshold of the sample, the polarization dependent of the microstructures break down as mentioned above which will result in texturing of polarization independent surface microstructures [31].

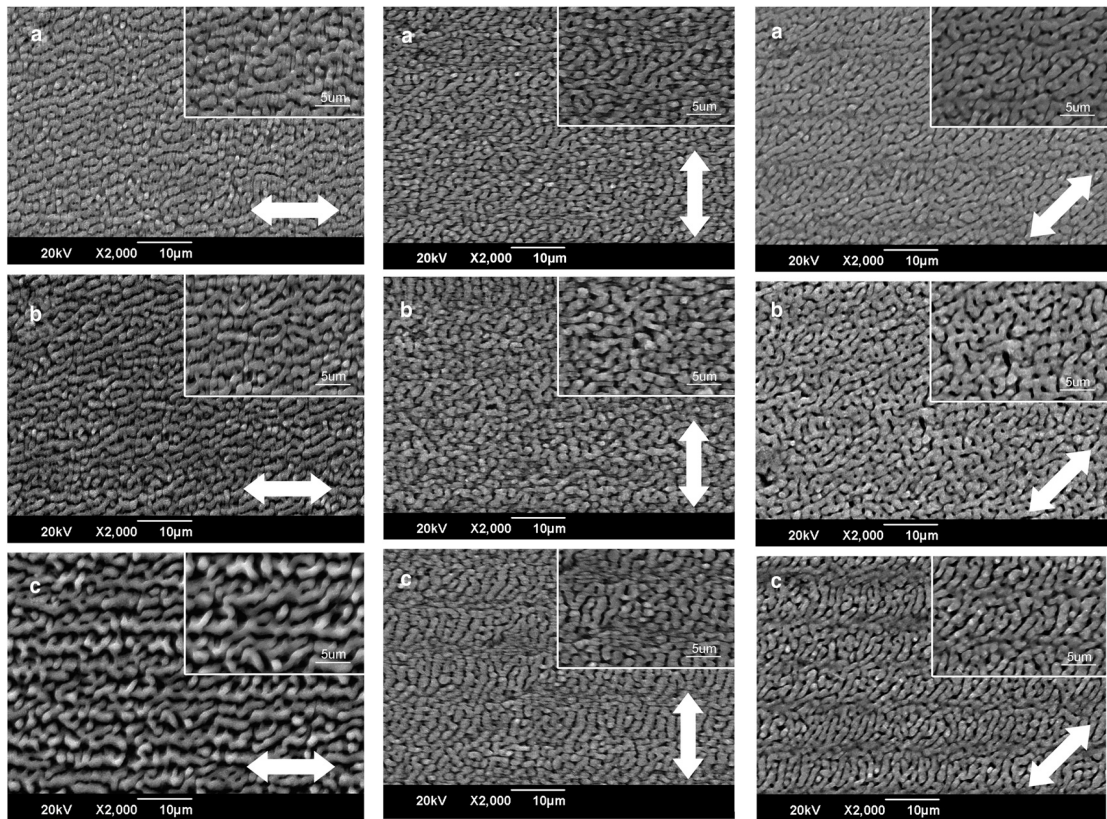


**Figure 2.10** Effects of horizontal polarized pulses on Si-Wafer[31].

### 2.1.8 Fluence

Increased laser intensity leads to a higher probability of nonlinear absorption. Thus it is safe to say shorter pulse duration is better for multiphoton excitation[41].

Also like melting thresholds, ablation thresholds for 800nm wavelength are always larger than the corresponding thresholds for 620 nm. This behavior can be explained by comparing the values of light absorption depth for the two wavelengths.

In case of liquid silicon, when the total energy transferred to the material becomes equal to the latent heat of evaporation, ablation is considered as complete. The subsequent heating is modeled by using the specific heat of the liquid phase.

Experiments were run to observe the effects of fluence on crystallization on a reflective Si surface. Ti:Sapphire laser at a wavelength of 800 nm, with a repetition rate of 1 kHz and a pulse width of 100 fs (Gaussian) was used. a-Si was sputtered on a less reflective c-Si by a 40mm objective lens in air. The Si used was Si(100). Laser fluence was set between the range of 0.03 J/cm<sup>2</sup> to 0.30 J/cm<sup>2</sup> in the range of 1 to 1000 pulses. As a result dark areas were observed on the surface expanding with increased energy. It was also observed that the thickness of a-Si increased with fluence, from 8nm to 30 nm in the center of the dark area[42]. It is stated that there is no plasma generation or surface morphology at a fluence of 0.2 J/cm<sup>2</sup> [43]

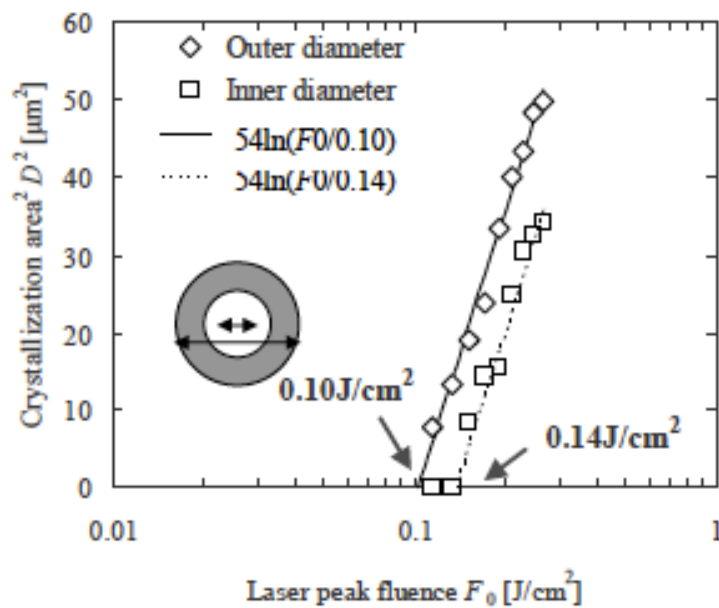


**Figure 2.11** Increase in crystallization dependant on laser peak fluence.[42]

### 2.1.8.1 Fluence thresholds

The irradiated surface area, pulse duration and power determine the fluence [44]. To calculate experimental fluence thresholds, two separate lasers with wavelengths of 620 nm and 800 nm were used with varying pulse durations between 50 fs and 200 fs. It was noted that ablation thresholds for 800 nm wavelength lasers are always higher than that of 620 nm wavelength lasers, the grounds for this was based on the light absorption depth difference of the two wavelengths. The increase

in fluence thresholds for different wavelengths and pulse durations were compiled on **Table 1** [34].

**Table 1** Fluence Threshold compilation for silicon ablation [34]

Fluence Threshold	Threshold Value (J/cm <sup>2</sup> )	$\tau_p$ (fs)	$\lambda$ (nm)
$F_{a1}$	0.30	80	620
$F_{a1}$	0.30	100-120	620
$F_{a1}$	0.32	130	620
$F_{a1}$	0.45	150	775
$F_{a2}$	0.458	83	800
$F_{a2}$	0.52	130	800

### 2.1.9 Melting threshold

The thermal absorption of the surface is characterized by the optical absorption.

According to literature the elapsed time to melt a select area on a surface takes the same time with both Femtosecond and Picosecond lasers [41].

According to **Figure 2.12** when a (111) silicon is shot at, three times the melting threshold with 130 fs pulses, at 620 nm wavelength and 0.47 J/cm<sup>2</sup> fluence; At the first picosecond a bright area occurs on the surface, then at 20 picoseconds a dark area forms in the middle of the bright area, which signifies the beginning of ablation. A ripple like formation can be observed clearly at 2 ns [41].

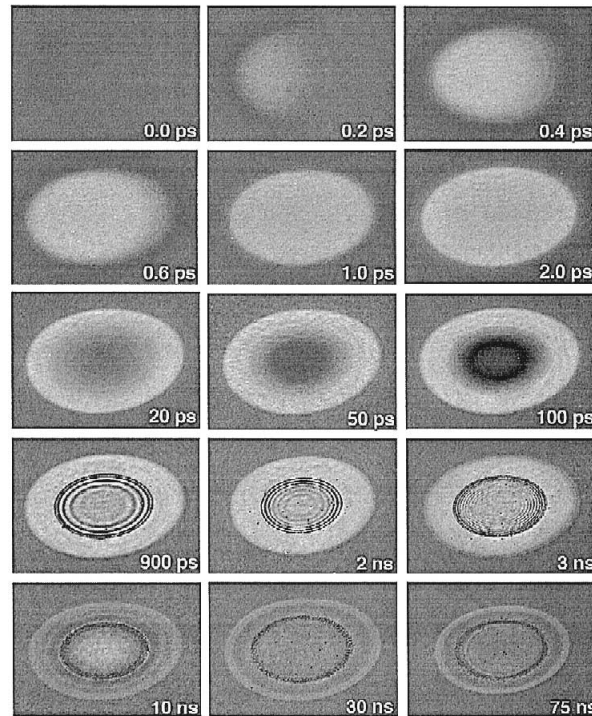


**Figure 2.12** Si(111) material timeline of exposure to 130fs, 620nm pulses [41, 45, 46].

## 2.2 Laser Ablation

The word ablation derives from the Latin word *ablatio*, which means removal [47]. Laser Ablation is the process of removing fractions of a material via erosive processes. Laser ablation occurs when the energy from the laser is transferred into the material to execute this process. The energy input thermodynamically into the target material via laser pulses, results in the sublimation or evaporation of fractions of it.

When the energy input administered is greater than the binding energy of the target material, decomposition or material removal occurs. During this process the applied energy is fully transferred to the internal energy of the material, consequently to the temperature of the target material coupled with its heat capacity and mass [48].

The aim of using short pulse lasers (such as Femtosecond Lasers) in this process is to avoid heat damage. In theory the pulses of such lasers are quick enough to remove the material that the surrounding area is unaffected of the heat. This is especially important while using heat sensitive materials such as Silicon.

By utilizing varying time scales such as Femtosecond, Nanosecond or Picosecond in observing this energy input it is evident that at femtosecond the material shows electronic excitation and emits electrons. However, in picosecond the material dissipates energy and emits ions and in nanosecond surface relaxation and reorganization occurs, with the presence of plasma plumes

Both experimental and theoretical studies have been carried out for the physics of laser ablation; with more accuracy in silicon, meaning: by using numerical models. Actually, the sequence of events ultimately leading to ablation bears radical complexity and as if causing more problems, takes place on an extensive scale of length and time. Therefore, the problem is resistant to analytical or phenomenological techniques (heat diffusion equations, two temperature model, etc); since they are prone to many limitations, and computer simulations stand out in handling complex thermo-mechanical pathway to the material follows, through the process of ablation. [34, 49]

Ablation occurs on a picosecond time scale, thus the thermal diffusion it causes on the material is nearly negligible. The thermal relaxation is characterized by the thermal diffusion length  $D$ , which is related to the pulse with  $\tau_p$  by  $D = \kappa\tau_p^{1/2}$ ,

where  $\kappa$  is the thermal diffusivity of the material [29]. Ablation precedes the thermal diffusion when  $D$  is shorter than the absorption length. This means the material does not have enough time to melt and re-solidify. Thus better spatial resolution is achieved.

### 2.2.1 Ablation mechanisms

During ablation electrons both bound and free on the surface layer become excited by absorbing multiple photons. As a result hot electrons are generated [50]. The material becomes ionized. A plasma forms at the surface of the material. Afterwards the energy is transferred to the lattice through bond breaking and material expansion [51].

### 2.2.2 Ablation threshold

The ablation threshold marks the laser fluence where ablation starts. Ablation threshold differs between materials, due to the properties of a given material.

There are multiple ablation thresholds for various materials such as graphite [28], stainless steel, copper, titanium, niobium [26] and silicon [8] as suggested in the literature [52]. A low threshold marks the material ejection and the second higher threshold marks the bond breaking of for example the ablated graphite material[16].

Both ablation thresholds can be defined by the logarithmic laws [52]:

$$\text{For lower laser fluence } L = d \ln \left[ \frac{F}{F_{th}^{skin}} \right] \quad (2.1)$$

$$\text{For higher laser fluence } L = l \ln \left[ \frac{F}{F_{th}^{thermal}} \right] \quad (2.2)$$

Where  $d$  is the total number of collisions leading to a reaction or not) per second,

$L$  is the number of collisions that result in a reaction per second (ablation depth)

$l$  is the thermal diffusion length and

$F$  defines the threshold laser fluence [53, 54]

The lowest fluence range for silicon is 150 mJ/cm<sup>2</sup>, whereas 300 mJ/cm<sup>2</sup> exceeds the ablation threshold for silicon [55].

Ablation thresholds for Silicon (100) has been tested with a Ti:Sapphire laser at 780 nm wavelength with 150 fs at a focal distance of 400 mm as seen in **Figure 2.13**. 20

Holes were drilled, and the above formulae were confirmed [5]. It is also noted that no difference was observed between Si (111) and Si (100) [102]. It was also noted that using a Gaussian distribution of energy with a femtosecond laser the lateral precision of the ablated area is limited by the fluence distribution [57].

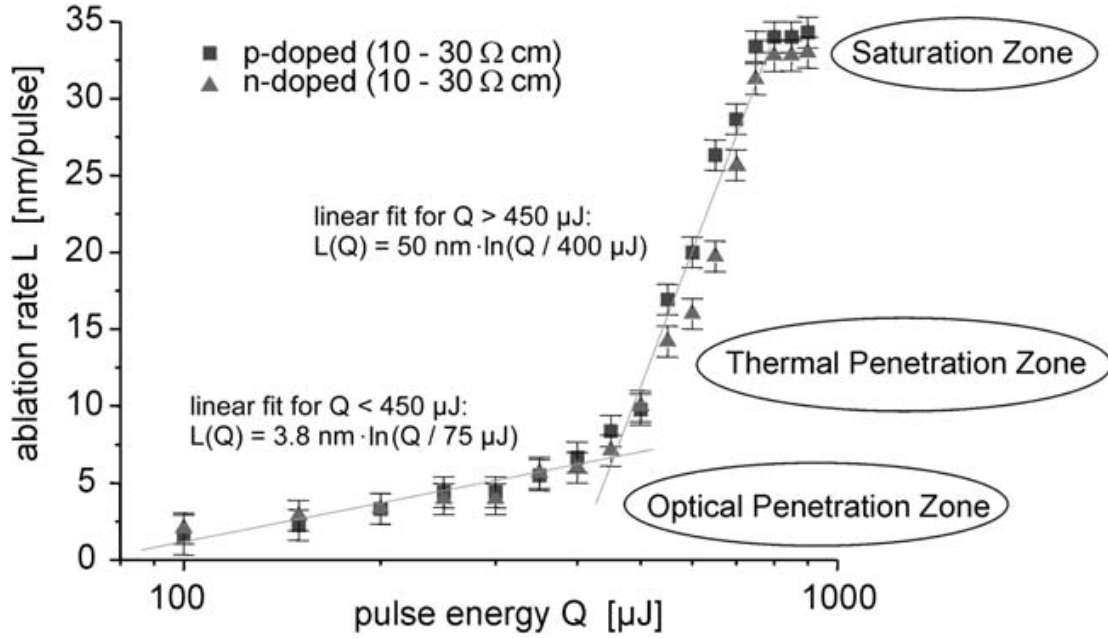


**Figure 2.13** Ablation rate for 20 holes drilled with 700 nm, 150 fs pulse with a focal length of 400 mm [56].

$$n = \text{mod}\{E_{gap}/1.55eV\} + 1 \quad (2.3)$$

$0 < E_{kin} \leq 1.55eV$  Defines the resulting kinetic energy.

### 2.3 Multiphoton Excitation (MPE)

Multi-Photon Excitation is the simultaneous absorption of multiple long wavelength photons. In solid material, the electrons are excited across the energy gap (band-gap), to the conduction band. For a situation where ultra-fast laser pulses at photon energy of  $1.55eV$  the excitation occurs via multi-photon absorption. Where  $n$  is the necessary number of photons.

Electrons located near the target surface, at a depth less than their mean free path, can leave the target when the conduction band is close to the vacuum level as can be observed in **Figure 2.14**.

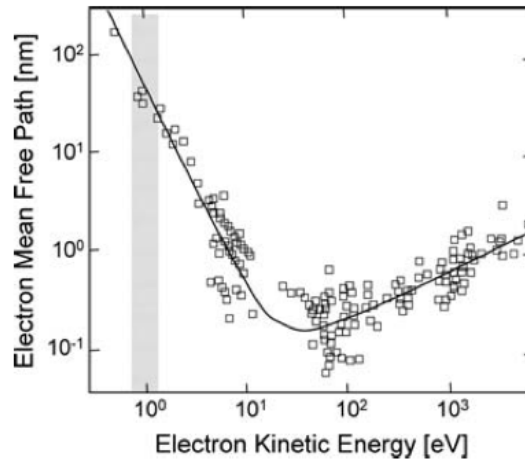


**Figure 2.14** Electron mean free path vs. electron kinetic energy. Shaded area is the typical kinetic energies in the presented situation [57]

## 2.4 Ripple Formation

Ripples as seen in **Figure 2.15** are formed during laser ablation, especially near the ablation threshold. The formation of ripples are investigated based on the scanning speed[67] pulse width[58] surface undulations[59] number of pulses[60] and various other variables of laser ablation.

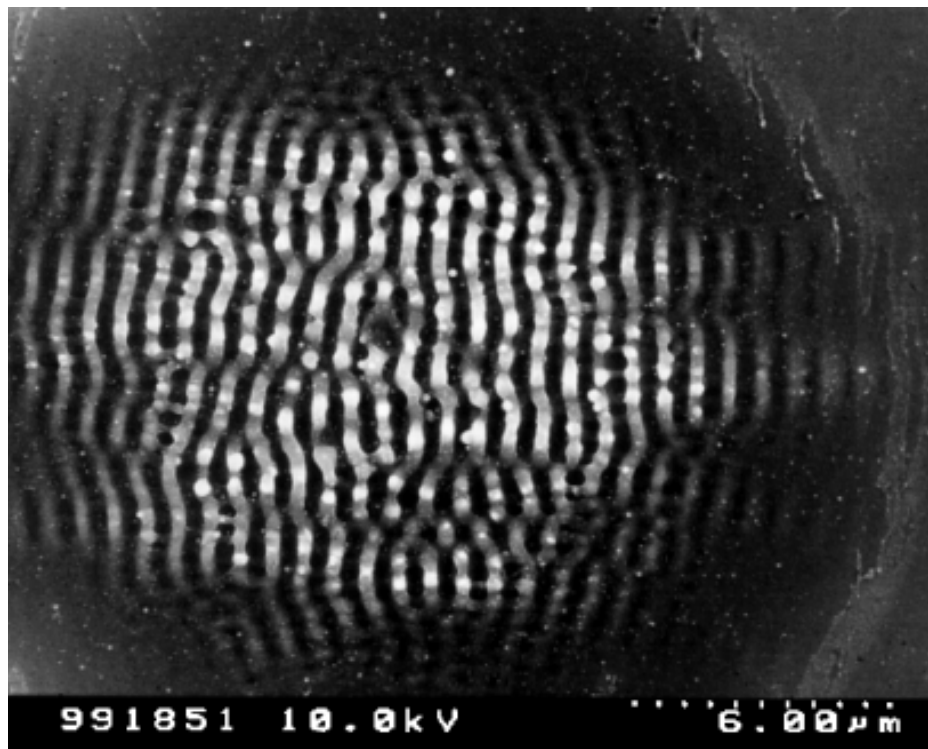


**Figure 2.15** Ripple direction is affiliated with the polarization angle. At  $0^\circ$  polarization angle the ripples are perpendicular to the scanning direction, while at  $90^\circ$  polarization angle the ripples are parallel to the scanning direction [24].

Various experiments on ripple formation show the formation and characteristics of ripples are based on parameters effecting ablation.

Experiments carried out at a pulse duration of 130 fs wavelength of 800 nm. The laser was run at a fluence rating of 1 kHz. The spacing of the ripples were accumulated based on the below formula:[33]

$$\Lambda = \lambda / (1 \pm \sin\theta) \quad (2.4)$$

Where  $\Lambda$  is the spacing of the ripples

$\lambda$  is the wavelength

$\theta$  is the polarization angle of the laser and,

$\pm$  is the direction of the wave either up or down

Meanwhile the space between two sequence of pulses is based on this formula:[33]

$$d = v/f \quad (2.5)$$

Where  $d$  is the space between 2 sequence of pulses

$v$  refers to the scan speed

$f$  is the frequency. [33]

It has been noted that temporal evolution of ring structures on Si(111) at 0.43 J/cm<sup>2</sup> occurs as follows: First the irradiated area is surrounded with dark rings coinciding with the ablated area [61], there is a precise threshold of laser fluence for the formation of said rings. This formation is noted to occur on all materials [62]. It was also reported that ripple formation occurs strongest closer to the melting threshold [63]. Ripples can be observed even way outside the irradiated area [64].

## **2.5 Heat Affected Zones (HAZ)**

It has been widely discussed that during laser interaction, physical happenings are strongly dependent on the duration of pulse. There is a huge difference between the femtosecond to nanosecond regimes [65]. HAZ does exist for Femtosecond Laser although it's two times smaller in magnitude [66].

Characteristically, 10µm to 1mm wide heat affected zones are observed during nanosecond machining[81]. Since interaction of ultra-short femtosecond pulses with the material is short enough and thermal diffusion is avoided, no heat affected zones are part of this regime.

## 2.6 Crater Depth Versus Laser Fluence

Single shots at various laser fluences are irradiated on the Si wafer. These shots create micro-sized craters. Two types of ablation regimes are identified from the craters. Semiconductors and polymers. These regimes have linear dependency on a logarithmic scale between the ablated depth and the laser fluence. The distinguishing factor between these two regimes is the volume over which the laser pulse energy is distributed. These volumes are determined by the optical or heat penetration depth for the low or high fluence regime, respectively. They are described by:

$$L_{optical,heat} \cong l_{optical,thermal} \ln \frac{F}{F_{th}} \quad (2.6)$$

F = applied fluence

F<sub>th</sub> = Treshold Fluence

L = Ablation Depth for the two regimes

At low fluence the number of hot electrons is very low. This accounts for the thermal equilibrium with the lattice that is achieved in mere picoseconds. This short time gives the charge carriers less time to move. Which means the optical penetration depth of the laser energy will exceed the thermal diffusion length of the charge carriers. Therefore energy transfer occurs only within the volume characterized by the optical penetration depth  $l_{optical} = 1/\alpha$ . But for higher fluence, the charge carriers have more energy and it takes longer for them to reach the thermal equilibrium with the lattice. Therefore, electron diffusion length  $l_{thermal}$  becomes significant causing an increase in the ablation rate.

Abrupt increase of rim height can be seen in **Figure 2.16**. This increase is chosen as a separation point between the two regimes. The results achieved with Low Fluence and High Fluence regimes can be seen in **Table 2** below.

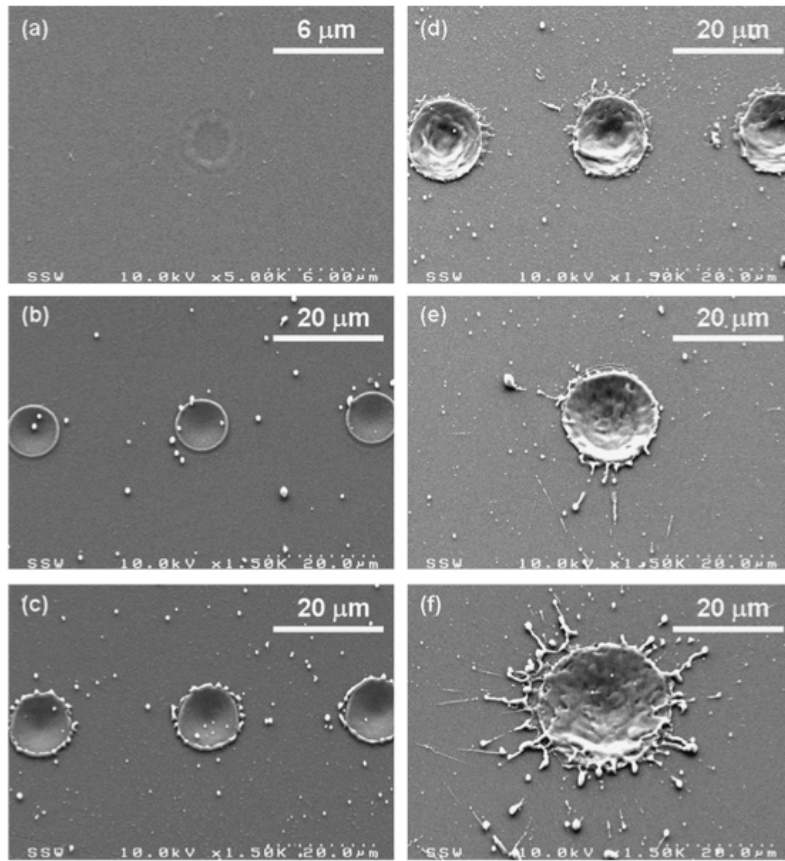


**Figure 2.16** SEM Micrographs of single-shot ablation craters showing characteristic patterns  $F = 0.63 \text{ J/cm}^2$ , (b)  $F=3.3 \text{ J/cm}^2$ , (c)  $F=12.5 \text{ J/cm}^2$ , (d)  $F=25 \text{ J/cm}^2$ ,  $F=125 \text{ J/cm}^2$ , (f)  $F=250 \text{ J/cm}^2$  [8].

Due to the nonlinear absorption characteristics of femtosecond laser irradiation the optical penetration depth was much lower than  $10 \mu\text{m}$ . Which was derived from the absorption coefficient of Si at  $780 \text{ nm}$  [35]. The estimated ablation threshold fluence of  $0.557 \text{ K/cm}^2$  for low fluence regime can be considered as the minimum fluence for crater formation by a single pulse. Meanwhile, the laser fluence of  $1.181 \text{ J/cm}^2$  may be interpreted as the level beyond which the electron temperature that attains a maximum at the target surface near the end of the pulse is sufficiently high to sustain carrier diffusion in the the bulk.

**Table 2** Comparison between the parameters estimated from the current and the literature values.

Regime Type		Experimental	REFERENCE [19]
Low Fluence Regime	$l_{optical}$	135nm	145nm
	$F_{th}^{(6)}$	$0.557 \text{ J/cm}^2$	$0.458 \text{ J/cm}^2$
High Fluence Regime	$l_{thermal}$	324nm	322nm
	$F_{th}^t$	$1.181 \text{ J/cm}^2$	$0.657 \text{ J/cm}^2$

The craters with laser fluences ranging from 0.625 to 666 J/cm<sup>2</sup> can be categorized into four characteristic crater patterns based on the morphological observations and topological analysis.

## 2.7 Surface Microstructures on Silicon

Being an important material in semiconductor industry, silicon is also very functional for MEMS devices and has received significant attention mainly because of its Potential of femtosecond laser ablation of silicon in micromachining application has created an attraction point for many studies [70].

The physics of the transient states of the single pulse ablation process using techniques including optical pump-probe [29], time-of-flight mass spectroscopy [6, 7, 8, 9] , and time-resolved microscopy [60] are mostly in focus in the studies in literature. Several theoretical models have been proposed which are based on molecular dynamics, for the purpose of modeling ultrafast heating and ablation processes [5, 6, 72].

Recently, several researchers have reported the formation of microstructures (such as ripples and spikes) on Si samples in the case of multiple pulse irradiations on stationary samples [7, 73, 74]. For example, investigation of the ablation process efficiency during silicon micromachining with femtosecond laser pulses in ambient air was carried explaining that the decrease of the ablation efficiency in the high fluence region ( $> 10 \text{ J/cm}^2$  ) is due to the strong interaction of the laser pulse together with the laser-induced plasma [68].

When substrates are irradiated at or above the melting threshold the surface deformations may form in the shape of spikes [4]. The height of these spikes are said to decrease when pulse duration is increased or fluence is decreased [73]. The shape of the spike formations is asymmetrical. This asymmetry is suggested to be caused by the dependence of polarization on Fresnel refraction [25]. They always point perpendicularly to the direction of polarization [25, 73] and don't show a directional difference for Si (100), (110) or (111) [72]. Furthermore the spike formations are suggested to be of interest for use in light absorbing surfaces [73] for solar cells [31].



### **3. EXPERIMENTAL SETUP**

The experiments were run with Amplitude brand laser, located in the Mechatronic Building in ITU Maslak Campus. The Amplitude produces S-pulse Femtosecond Laser which are used for a wide variety of applications. In the following experiments the Amplitude S-Pulse Femtosecond laser was used for structuring microfluidic cavities [2].

#### **3.1 S-Pulse**

Amplitude s-pulse delivers 1030 nm repetition rate pulses. It is a diode-pumped compact laser with a pulse duration of 500 fs.

As a laser medium the s-pulse uses Ytterbium. The ytterbium doping allows for high thermal efficiency and pulses with high average power.

The system includes a compact power supply, a synchronisation unit, an autonomous chiller and a laser head. There are no external water cooling units in this setup. The system consumes low electricity [2]

#### **3.2 Laser Operating Principles**

##### **3.2.1 Chirped pulse amplification**

A high-energy laser constitutes of a laser oscillator, which emits femtosecond pulses at a low energy and high repetition rate, and a laser amplifier.

Direct amplification of a pulse would cause optical damage in the amplifier before the desired energy level is reached, since the peak power of a pulse is inversely short.

For safe and efficient use of amplified femtosecond pulses Chirped Pulse Amplification (CPA) is used.

With this technique in order to decrease the peak power of oscillator pulses, they are temporally stretched. Thus low-peak pulses can safely be amplified. A pulse compressor is used to re-compress the high-energy pulses to their initial duration

after the amplification [2]. The difference in pulses after going through the oscillator, amplifier, stretcher and compressor are shown in **Figure 3.1**.

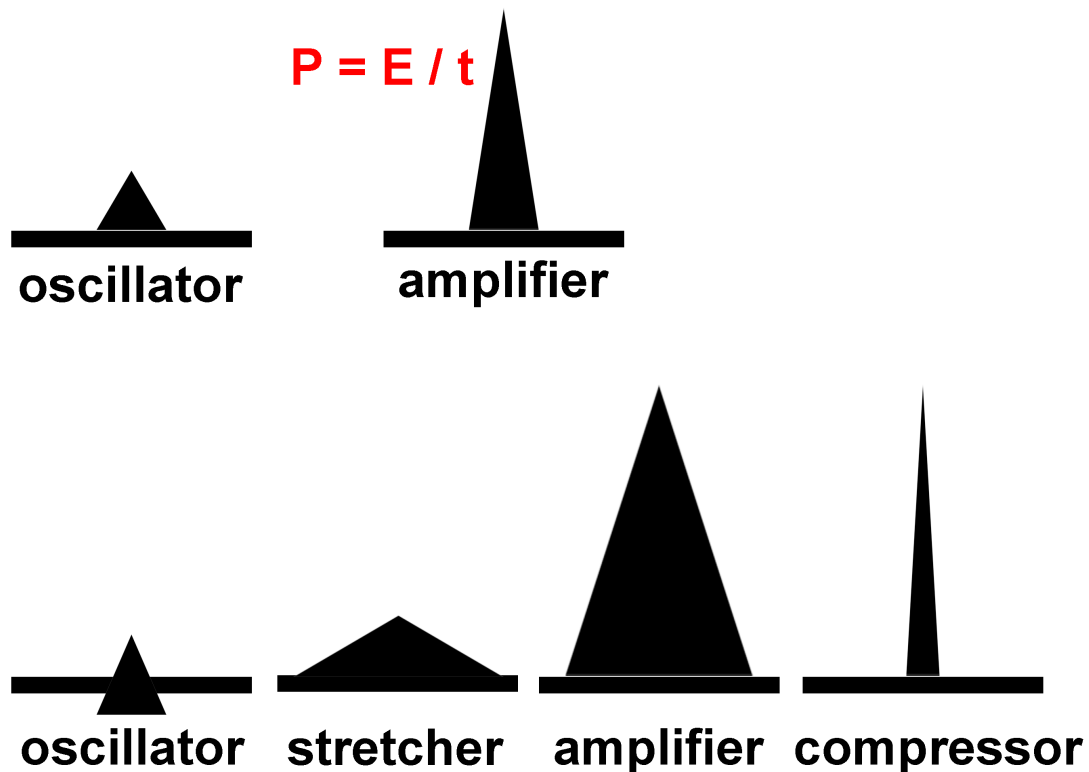


**Figure 3.1** Oscillator, stretcher, amplifier and compressor [2].

### 3.2.2 Laser oscillator

Femtosecond pulses with around 10 nJ to 20 nJ at a high repetition rate of 50 MHz is emitted from the integrated laser oscillator.

Ytterbium doped crystal is used as laser material. It transmits in the 940 nm to 980 nm infrared range, which makes it compatible with direct diode-pumping. The fluorescence bandwidth can sustain ultra-short pulse durations.

Solid-state non-linear mirror is used to achieve short pulse generation. The reflection coefficient of these pulses increase with the incident pulse energy.

Furthermore the laser operates in the “Soliton” regime [2].

### 3.2.3 Pulse stretcher

Pulse stretching benefits from the essence of femtosecond pulse to have a broad spectrum. The relation between the spectrum and pulse duration is as follows:

$$\Delta T x \Delta v > k \quad (3.1)$$

$k$  is a constant, that depends on the temporal pulse shape [2].

The process of the pulse stretcher is shown in **Figure 3.2**.

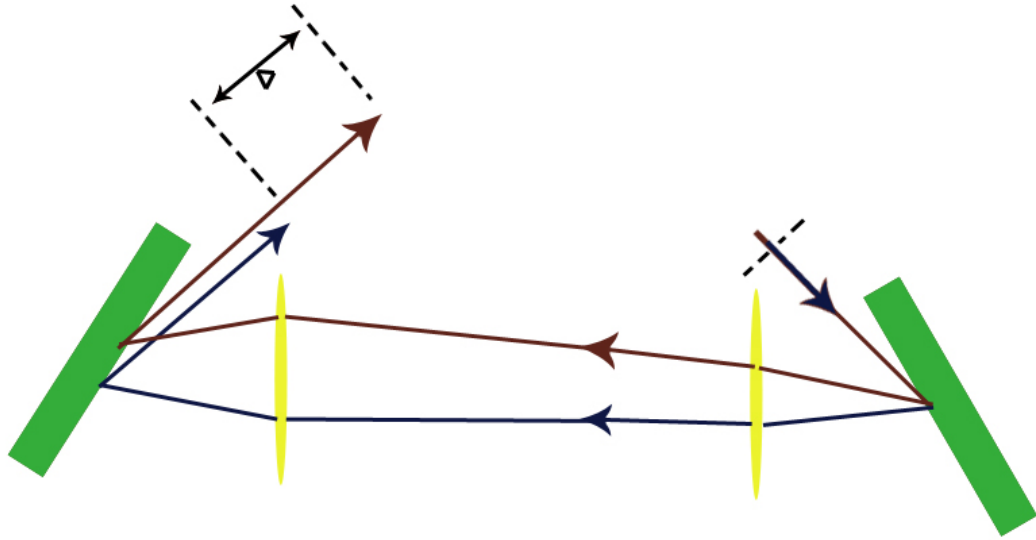


**Figure 3.2** Schematic drawing for pulse stretcher includes two diffraction gratings [2].

### 3.2.4 Laser amplifier

The laser amplifier is essentially a resonator, employing temporally stretched pulse from the oscillator. The amplifier is regenerative which allows for a large amplification ratio.

A switch module for pockels cells catches a single pulse from the oscillator amplifier. Which is amplified by several rounds in the amplifier. Once desired energy level is reached the pulse is sent out by the same switch. After which the pulse is sent to the pulse compressor via an optical routing device [2]. The principle of the laser amplifier is shown in **Figure 3.3**.

### 3.2.5 Pulse compressor

After the pulse compressor receives the pulse, it is returned to its initial duration [2].

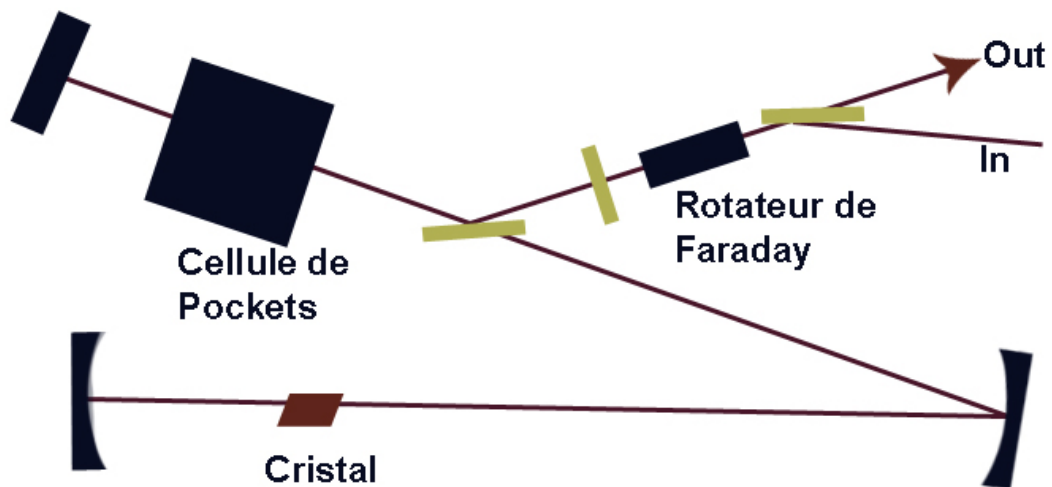


**Figure 3.3** Drawing of Laser Amplifier [2]

### 3.2.6 Wave plate

When photons leave the laser, they enter the wave-plate. The wave plate converts and routes the waves that enter, which allows us to manually set the photon power.

While the wave plate guides and converts the waves entering in, it allows setting the photon power manually. Consequently allowing experimentation with different energy levels. The results can then be compared to achieve the necessary energy level parameters to make the smoothest canal, while also testing ablation thresholds [54].

#### 3.2.6.1 Operating principle of wave plates

Optical wave plates are constructed from birefringent material. This material introduces a phase difference between the fast and slow principal axes of the wave plate. A difference in refractive index is made possible between the two axes, by the birefringent properties of the material. The reaction is a difference in the velocity between the two orthogonal components. The fast principal axis of the wave plate has a lower refractive index in which makes possible a faster wave velocity. The slower velocity is created by the slow axis which has a higher refractive index. The real phase shift produced is dependent on the properties of the material, the thickness of the wave plate and the wavelength of the signal, characterized as:

$$\Delta\phi = \frac{2\pi d(n_1 - n_2)}{\lambda} \quad (3.2)$$

Where  $\lambda$  is the wavelength of the pulse created by the laser.

symbolized by  $n_1$  as the refractive index of the principal plane,  $n_2$  as the refractive index of the orthogonal plane, and  $d$  as the thickness of the wave plate [54].

### 3.2.6.2 Using a wave plate

Wave plates are typically available as  $\lambda/4$  or  $\lambda/2$  meaning a phase shift of quarter of a wave or half a wavelength (respectively) is created [54].

### 3.2.6.3 Half-wave

As per the description above, a wave plate maintains two principal axes: fast and slow, where each axis has a different refractive index and, thus, a different wave velocity. When a linearly polarized beam is wave plate, and the polarization of this beam does not coincide with one of these axes, the output polarization will be linear and rotated with respect to the polarization of the input beam. When implementing a circularly polarized beam, a clockwise (counter-clockwise) circular polarization will convert into a counter-clockwise (clockwise) circular polarization. The behaviour at the photon entering the half wave plate is shown in **Figures 3.4 and 3.5**.

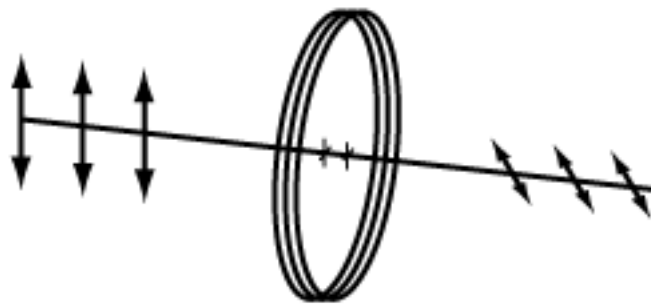


**Figure 3.4** Half Plate representation [54].

The output polarization will be linear and rotated with respect to the polarization of the input beam as can be seen in **Figure 3.4**. When applying a circularly polarized beam, a clockwise (counter-clockwise) circular polarization will transform into a counter-clockwise (clockwise) circular polarization.

Half-wave ( $\lambda/2$ ) plates are typically used as polarization rotators. Mounted on a rotation mount, a  $\lambda/2$  wave plate can be used as a continuously adjustable

polarization rotator, as shown below in **Figure 3.5**. Additionally, when used in conjunction with a Polarizing Beamsplitter a  $\lambda/2$  wave plate can be used as a variable ratio beamsplitter.

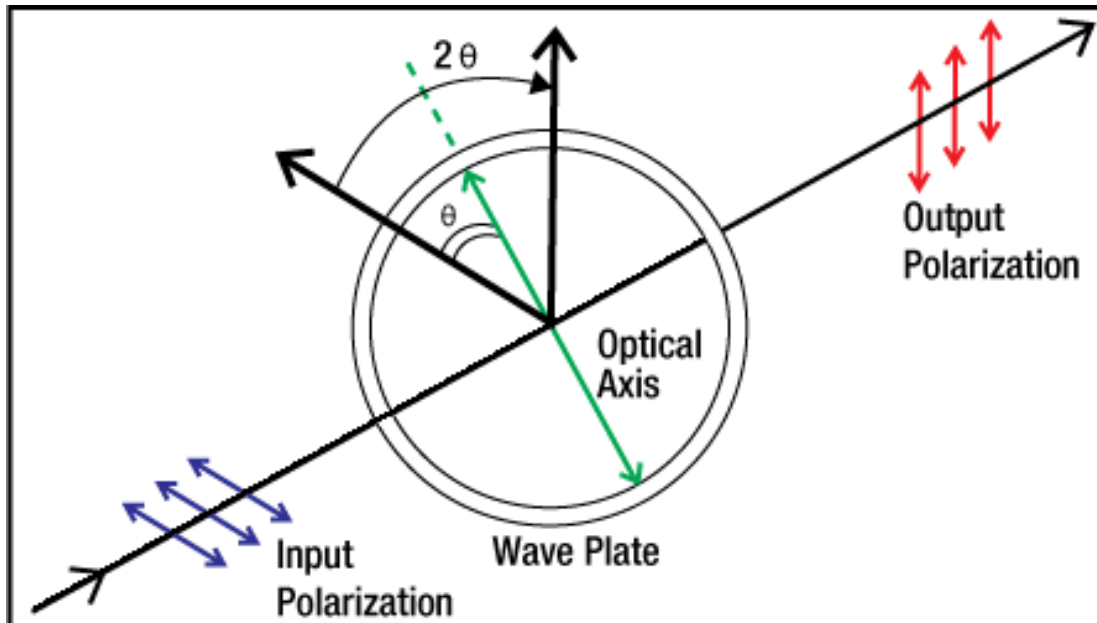


**Figure 3.5** Wave Plate operating mechanisms [54].

The angle between the output polarization and the input polarization will be twice the angle between the input polarization and the wave plate's axis as seen again in **Figure 3.5**. When the polarization of the input beam is directed along one of the axes of the wave plate, the polarization direction will remain unchanged [54].

#### 3.2.6.4 Quarter-wave

A quarter-wave plate is designed in a way that the phase shift created between the fast and slow axes represents a quarter wavelength ( $\lambda/4$ ) or a multiple of  $\lambda/4$ . When implementing a linearly polarized beam with the polarization plane aligned at  $45^\circ$  to the wave plate's principal plane, the output beam will be circularly polarized. Similarly, when applying a circularly polarized beam to a  $\lambda/4$  wave plate the output beam will be linearly polarized. Quarter wave plates are used in Optical Isolators, Optical pumps, and EO modulators. The behaviour of the photon after entering the quarter wave plate is shown in **Figure 3.6**.

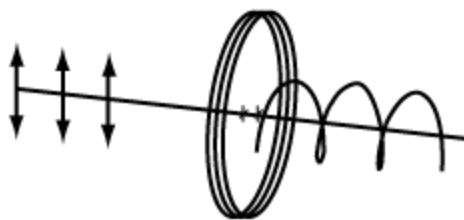


**Figure 3.6** Quarter Wave representation [54].

We use a half-plate on our setup.

After leaving the wave-plate, the photon enters the sonar polarizer. The purpose of the polarizer is to turn the photon manually in perpendicular or in parallel to the desired angle

Polarizers with Calcite do not pass any photons different from the desired angle [54].

### **3.2.6.5 Principles of polarizers with calcite (polarization-dependent refraction – glan laser calcite polarizer)**

Between two orthogonally polarized waves traveling in the crystal, a differential delay is created due to the birefringent structure of calcite. This birefringent structure creates a polarization-dependent refraction which effectively steers the polarization planes in two angles. Whereas the ordinary plane will travel straight through the crystal, the extraordinary plane will exit the crystal at an angle proportional to the wavelength and the length of the crystal as well.

As shown in **Figure 3.7** a calcite polarizer can be designed either as a polarization splitter/combiner or as a polarizer element that serves to remove the angled, orthogonally polarized component of a beam.

The beam output was adjusted through the waveplate, while changing the polarization angle with the polarizer. Either 1030 nm wavelength beam, or 515 nm wavelength beam was used, shifted from 1030 nm by crystals.

for 1030 nm wavelength, Thorlabs E03 Mirror was used, and for 515 nm wavelength Thorlabs E02 was used. The broadband of these mirrors are shown in **Table 3**.

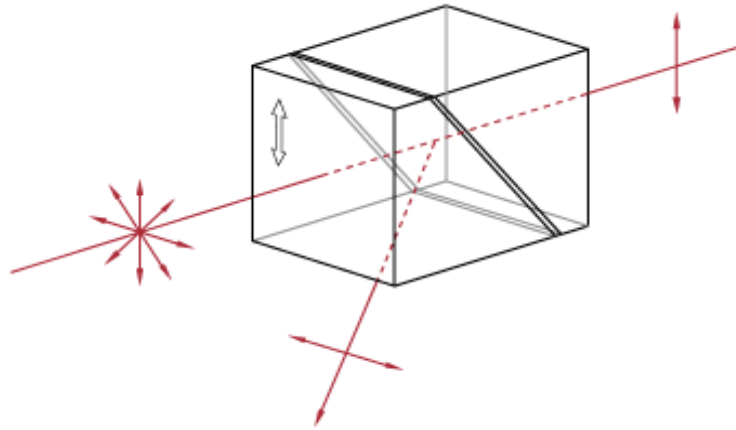


**Figure 3.7** Drawing of polarizer [54].

These mirrors are made up of multiple layers of dielectric films deposited on a fused silica substrate, supplying excellent thermal stability. The thickness of the film is controlled in a way that the reflections from each surface interfere constructively over a certain wavelength range. Owing to the structure of the multilayer dielectric coating, the spectral range over which the mirror is highly reflective shifts toward longer wavelengths as the angle of incidence decreases toward zero [54].

**Table 3** Thorlabs Broadband Dielectric Mirror Specifications [54].

<b>Substrate Material</b>	Fused Silica
<b>Clear Aperture</b>	>90% of Diameter
<b>Front Surface Flatness</b>	$\lambda/10$ at 633 nm
<b>Front Surface Quality</b>	10-5 Scratch-Dig
<b>Back Surface</b>	Fine Ground
<b>Diameter Tolerance</b>	+0/-0.1 mm
<b>Thickness Tolerance</b>	$\pm 0.2$ mm
<b>Wedge</b>	$\geq 3$ arcmin
<b>Chamfers</b>	0.50 mm x 45° Both sides
<b>Laser Damage Threshold</b>	2 kW/cm <sup>2</sup> CW, 100 mJ/cm: (10 ns Pulse)
<i><math>R_{avg} &gt; 99\%</math> for S and P Polarization for Angles of Incidence from 0° to 45°</i>	

### 3.3 $\lambda$ for 515nm

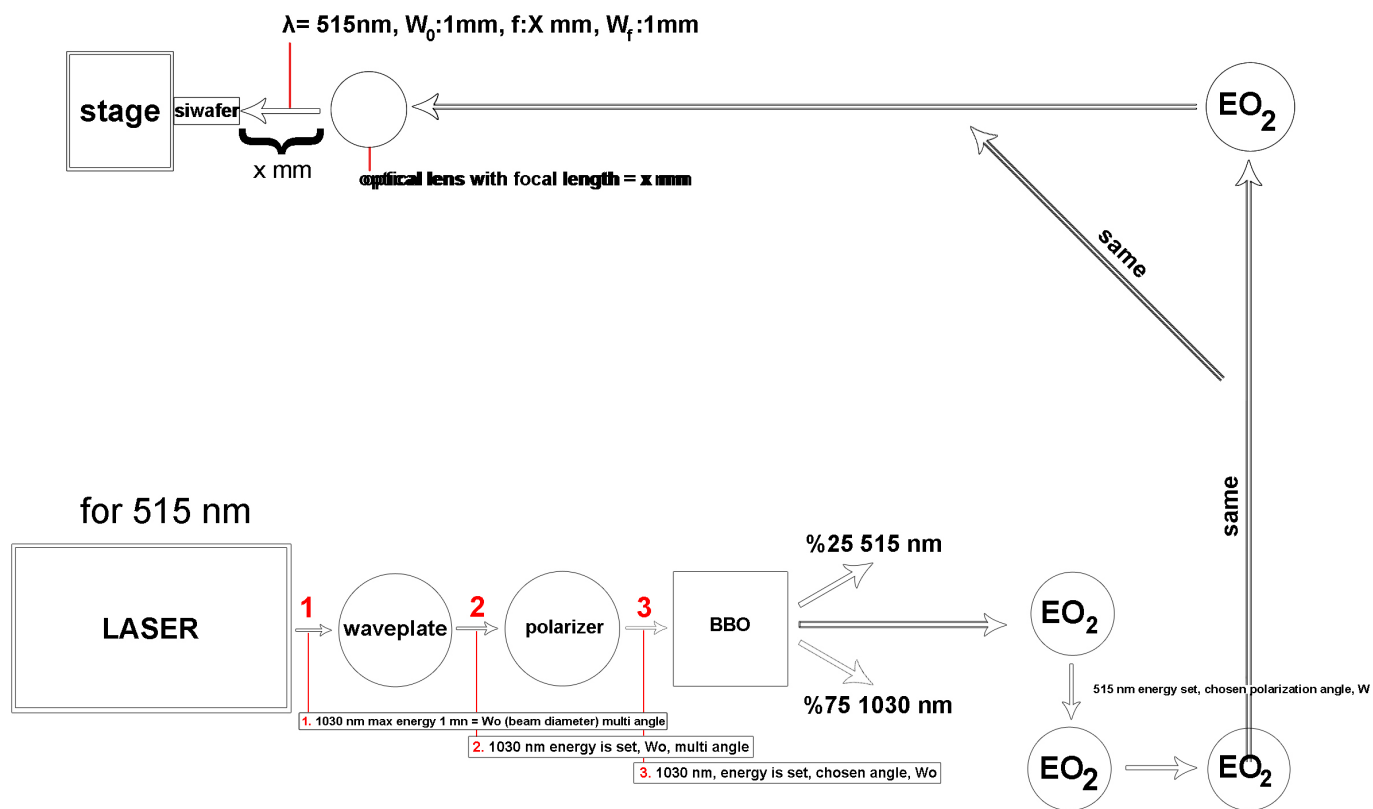
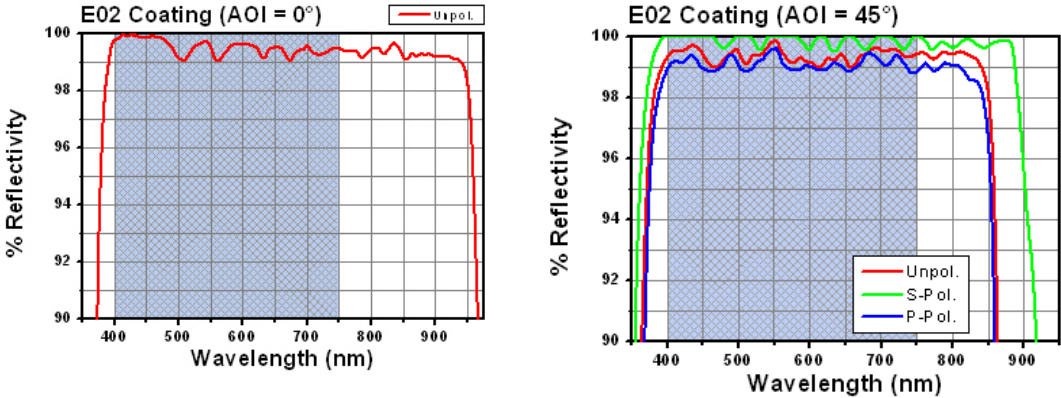


Figure 3.8 Setup for Achieving 515 nm wavelength

The process for creating a 515 nm photon is presented in **Figure 3.8**. The photons are sent into a Beta Barium Borat (BBO) crystal and in effect divided into two wavelengths. The ratio of the divided wavelengths is 75% 1030 nm and 25% 515 nm. After which the light beam enters facing E02 mirrors, that are used to eliminate the 1030 nm wavelength. The main attribute of the E02 mirrors is their ability to absorb the 1030 nm wavelength reflecting only the 515 nm wavelength. The E02 mirrors work like a bridge in a network system. Thus the 75% 1030 nm wavelength is eliminated, and the 25% 515 nm wavelength is directed towards the lens. As can be seen on Figures 3.8 and 3.9 the E02 mirrors operate between the wavelengths of 400 nm to 750 nm at 0° and 45° polarization.



**Figure 3.9** 0° E02 mirror coating, reflectivity vs. wavelength [54].

The process for creating a 1030 nm photon is presented in **Figure 3.10**. The 1030nm photon which has switched directions can be reflected off of the E03 mirrors after leaving the polarizers, to be transported to the desired location. E03 mirrors like the E02’s work like a bridge in a network system. As seen in **Figure 3.11** the E03 mirror can directly reflect 700nm to 1200nm wavelength photons at a 99% rate.

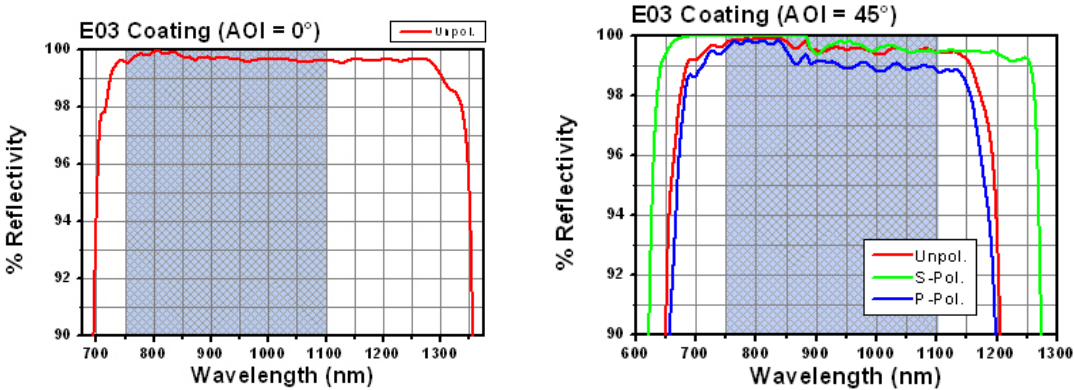


**Figure 3.10** 0° E03 mirror coating, reflectivity vs. wavelength [54].

### 3.4 $\lambda$ for 1030nm

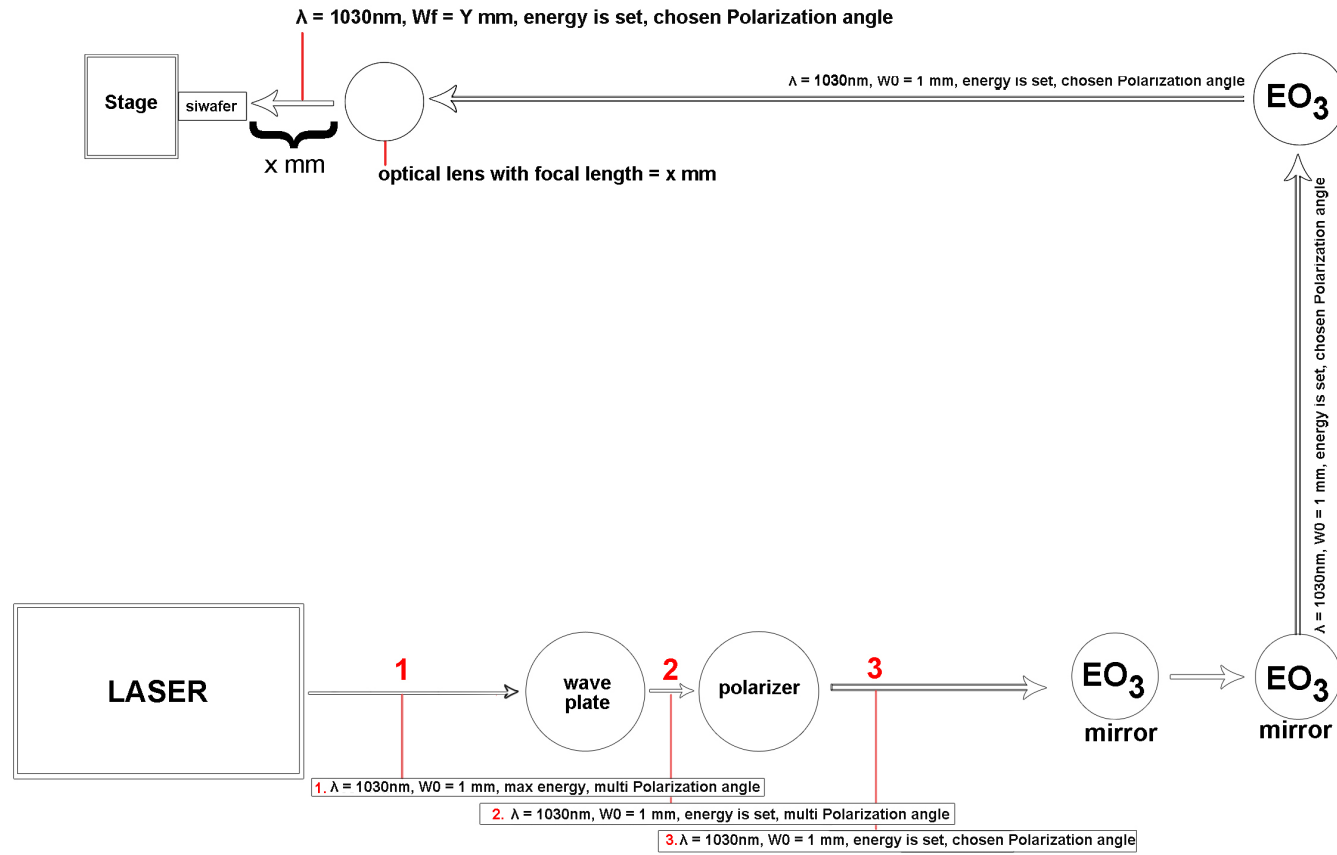


**Figure 3.11** The Process for creating a photon of 1030 nm

The E03 mirrors operate between 750 nm to 1100 nm range at 0° and 45° polarization angles. The mirror specifications are given below on **Table 4** and continued on **Table 5**.

**Table 4** Mirror specifications [54].

Specifications		
Material	Fused Silica	
Flatness	$\lambda/10$	
Surface Quality	10-5 Scratch-Dig	
Back Surface	Fine Ground	
Clear Aperture	>90% of diameter	
Parallelism	$\leq 3$ arc min	
Thickness	Ø1/2" Optics	6 mm (0.236°)
	Ø1" Optics	6 mm (0.236°)
	Ø2" Optics	12 mm (0.472°)
	Ø3" Optics	19.05 mm (0.75°)
	Ø4" Optics	19.05 mm (0.75°)
Thickness Tolerance	$\pm 0.2$ mm	
Diameter Tolerance	+0.00 mm / -0.10 mm	

**Table 5** E02 and E03 mirror specifications [54].

Coating Designation	Damage Threshold
E02	0.25 J/cm <sup>2</sup> (532 nm, 10 ns, 10 Hz, Ø0.803 mm)
E03	1 J/cm <sup>2</sup> (810 nm, 10 ns, 10 Hz, Ø0.133 mm)

### 3.5 Optical Lenses

After the photons are directed in the desired direction, lenses are used to focus them. The lenses are chosen based on the wavelength (1030nm or 515nm), focus radius (in other words the desired cavity radius), radius of the incoming laser and therefore the achieved focus distance.

In short the lenses are determined by using the given photon parameters and considering the desired cavity radius.

The distance between the material and the lens must be the same as the focus distance of the lens. The focus distance of a lens is the distance in which the light is concentrated in to a point [54].

### 3.6 Focal Length

Focal Length is the measurement of an optical systems ability to focus or defocus light as seen in **Figure 3.12**.

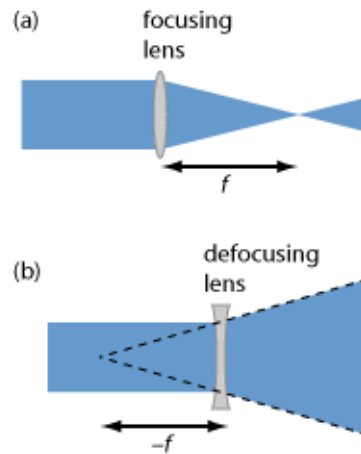


**Figure 3.12** Focal length of focusing and defocusing lenses. [54]

There are various optical systems which can focus/defocus light. The focal length is used to quantify the length in which the light is focused [54].

### 3.7 Focal Length Of A Curved Mirror

To focus or defocus light curved mirrors can be used. The radius of curved mirrors is usually between 10 mm and 5 mm. Concave mirror with curvature radius of the surface has a focal length of  $f = R/2$ . Whereas a convex mirror uses the formula  $f = -R/2$ . The formula assumes  $R$  is always positive. If the angle between the beam axis and the normal direction is not 0 ( $\theta$ ), then:

$$f_{tan} = (R/2) \cdot \cos\theta \quad (3.3)$$

is used to calculate the focal length. This definition can't be used for an optical system with multiple lenses (other optical elements) because where to measure the distance from is unclear.

### 3.8 Achievable Beam Waist Radius

The formula  $W_f = \lambda/\pi W_0$  is used to calculate the beam waist after it exits the lens. The beam waist in the formula must be much smaller than  $W_0$ . This equation shows that  $f$ 's ratio to the radius of the open aperture of the lens is used to determine focal length.

The experiments were run using a beam radius  $W_0$  of 0.8 mm and a wavelength of 1030 nm.  $W_f$  is equal to the radius of a given cavity.

LB1471-B and LA1131-B lenses with a focal length of 50 mm was used to create cavities at 40.98 radius. LB1092-B lens with a focal length of 15 mm was used for cavities with 12.29 radius and for cavities with 20.85 radius LB1761-B lens with 25.44 focal length was used. All the lenses used were between 650 nm and 1050 nm wavelength and different lenses need to be used for 515 nm wavelength experiments.

### **3.9 Surface Characteristics**

To observe surface characteristics at almost nano dimension Zeiss EVO MA10 SEM was used. To observe mm and micron sizes BX-RPA Optical Microscope with a DP72 Camera was used. The SEM works via charging the surface electrons. Both devices reside in the Clean Room in ITU Maslak Campus.

### **3.10 Substrate**

P-Type Si-Wafer (100) was used for all of the experiments. As observed from the literature Si-Wafer (100) and Si-Wafer (111) show differences in ablation process [2, 13, 16, 48, 53, 54, 55, 56, 57, 84].

The P-Type Si-Wafer is a test grade wafer with a thickness of  $525 \pm 25 \mu\text{m}$ , diameter of 100 mm and orient of  $\langle 1-0-0 \rangle$ , has a 1 side polished surface.

### **3.11 Experimental Parameters**

The substrate was placed on a stage capable of moving in 3 axis, connected to a computer where it was possible to input acceleration and scan length values.

The laser power could be used directly at 1 kHz limitlessly, or a function generation was put in place to control frequency and pulse numbers.

Parameters used in the following experiments were:

**Scan Speed** [ $\mu\text{m/s}$ ]: This could be set from the computer and dictates which direction and acceleration and with what speed the stage moves (thus the laser moves on the substrate). As the scan speed is lowered more pulses accumulate over the area hit by the laser beam.

**Scan Length:** Equal to the length of the created cavity.

**Cycle:** The amount of passes over the irradiated area. Every single pass over the cavity is equal to one cycle.

**Passover:** How many times the laser makes a round trip over the cavity. Passover equals two cycles.

**Pulse Duration:** 500 femtoseconds for 1 khz 1030 nm laser beam (effected by fluence thresholds).

**Frequency:** Amount of pulses per second, for the following experiments either 1 kHz or 0.1 kHz was used. Fluence threshold increases when frequency does.

**Number of Pulses:** Could be configured with the function generator, or the naked laser could be used for 1000 pulses per second.

**Desired Cavity Diameter:** Can be filtered to configure the beam waist hitting the substrate.

**Energy, Power:** Configured via the wave plate.

**Polarizer Angle:** Sets the angle of the photon using the polarizer.

**Fluence:** Obtained by the ratio of the incoming energy to the beam waist radiused circle

**Laser Time:** How long the operation takes.

**Scan Time:** Movement time of the stage.

**Actual Cavity Diameter:** Diameter of the created cavity.

**Melting Threshold:** The fluence level where Silisium begins to abrade (changes depending on pulse duration and wavelength [68])

**Ablation Threshold:** The fluence level where silisium begins to get damaged [2, 13, 16, 48, 53, 54, 55, 56, 57, 84].



## **4. EXPERIMENTS AND RESULT DISCUSSION**

### **4.1 Focus Calibration**

As a starting step focuses were calibrated. Lenses with a focal length of 25.4 mm were used. Therefore the distance between the Si-Wafer and the lens was set to 25.4 mm's as well.

At first pulses with high energy and repetition rates were irradiated from the laser, achieving spot sized holes. But since the setup was handmade it wasn't clear whether it was accurate on a micro scale. It was decided that to confirm the accuracy of the focal length, the fluence was to be set to the melting threshold. Because the melting threshold is the lowest intensity of energy required to create a visible change on the Si-Wafer so that surface modifications that may have occurred can be examined [48,85]. Because if the focal length was truly accurate, the target material would be abraded even with the lowest energy intensity level of melting threshold.

No ablation occurred as the distance drew further away from the exact focal length, since the lowest energy level that can ablate the Si-Wafer was used. The lowest energy / fluence levels mentioned are the limits required to start ablation as found in the literature [2, 13, 16, 48, 53, 54, 55, 56, 57, 84].

Using the minimum energy level that can ablate Si-Wafer's, the only physical change in the wafer occurs when the lens with the focal length is set to the exact position. Even a few micrometers can break the equation.

After several manual attempts for focus calibration, the focus calibration was set. This was ascertained as the lowest energy intensity levels for ablation as denoted in the literature was used, and ablation did in fact occur.

### **4.2 First Laser Pulses**

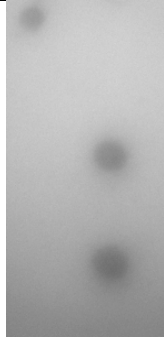
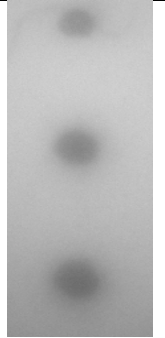
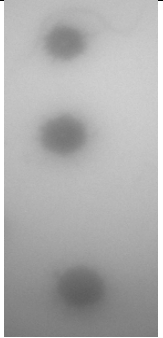
First pulses were irradiated using a function generator to manually set the repetition rate to desired values, instead of sending fixed beams from the laser. The exact number of pulses hitting the substrate couldn't be attained because the shutter was

switched on and off manually. To calculate the exact number of pulses a function generator was used. The function generator has also shown the exact amount of frequency and as a result the exact duration of the scan time according to the given calibration.

#### 4.2.1 Spot shots

Material surface was irradiated with 1, 5, 10 shots respectively at different fluence levels. A low magnification optical camera was used to take the images. Even though the resulting images are indistinctive, the increase in Hole diameter based on energy levels and number of pulses is clear. The images in **Table 6** indicate that as the energy transferred with light increases the diameters of the holes widen.

**Table 6** Optical camera images of Si-Wafer irradiated with differing fluence levels and number of pulses.

1030 nm, 0° polarization, 500 fs pulse duration				
				
Fluence:0.294 J/cm <sup>2</sup>	Fluence:0.587 J/cm <sup>2</sup>	Fluence:0.881 J/cm <sup>2</sup>	Fluence: 1.47 J/cm <sup>2</sup>	Fluence:2.94 J/cm <sup>2</sup>
Irradiations of 1, 5 and 10 pulses, at an energy level of 2 μJ with afocal length of 25.4 mm				

A 1030 nm wavelength laser with a pulse duration of 500 fs and a frequency of 1 kHz at a polarization angle of 0°, was used for the spot shot experiment. The 25.4 mm focal length lens was used. Energy levels were sequentially set to 1 mW, 2 mW, 3 mW, 5 mW and 10 mW. At every energy level respectively 1, 5 and 10 pulses are sent to create 3 different holes for each energy level as shown in **Table 7**.

As a result there is no image for the ablation after a single pulse shot with the fluence of 0.294 J/cm<sup>2</sup>. This could have one of several different meanings as listed below:

If the fluence of 0.294 J/cm<sup>2</sup> was below the melting threshold. This was unlikely considering the literature [2, 13, 16, 48, 53, 54, 55, 56, 57, 84], where melting threshold was said to be 0.15 J/cm<sup>2</sup>.

**Table 7** Experiment statistics for pulse shots with varying number of pulses power and fluence.

Cavity No.	Scan Speed [ $\mu\text{m/s}$ ]	Pulses	Power [mW]	Frequency [kHz]	Fluence [J/cm <sup>2</sup> ]	Energy [ $\mu\text{J}$ ]	Focal Length [mm]	W0 [mm]	Polarizer Angle
Hole 1	3000	1	1	1	0.294	1	25.4	0.8	0°
Hole 2	3000	5	1	1	0.294	1	25.4	0.8	0°
Hole 3	3000	10	1	1	0.294	1	25.4	0.8	0°
Hole 4	3000	1	2	1	0.587	2	25.4	0.8	0°
Hole 5	3000	5	2	1	0.587	2	25.4	0.8	0°
Hole 6	3000	10	2	1	0.587	2	25.4	0.8	0°
Hole 7	3000	1	3	1	0.881	3	25.4	0.8	0°
Hole 8	3000	5	3	1	0.881	3	25.4	0.8	0°
Hole 9	3000	10	3	1	0.881	3	25.4	0.8	0°
Hole 10	3000	1	5	1	1.47	5	25.4	0.8	0°
Hole 11	3000	5	5	1	1.47	5	25.4	0.8	0°
Hole 12	3000	10	5	1	1.47	5	25.4	0.8	0°
Hole 13	3000	1	10	1	2.94	10	25.4	0.8	0°
Hole 14	3000	5	10	1	2.94	10	25.4	0.8	0°
Hole 15	3000	10	10	1	2.94	10	25.4	0.8	0°

Because only a single laser beam is sent to ablate the bulk material.

The image is indistinctive, so the ablated area cannot be differentiated from the rest of the substrate.

### 4.3 Cavities

In this setup the stage is moved while the laser shoots pulses to create cavities instead of holes. The repetition rate was manually set with the function generator. The aim is to achieve cavities of 10  $\mu\text{m}$  in diameter and 120  $\mu\text{m}$  in length. To achieve these results the lens must be substituted by a beam waist (a lens that will create 10  $\mu\text{m}$  diameter cavities).

The below formula was used to calculate which focal length lens was required to achieve the Desired Cavity Diameter [85]:

$$W_f = \frac{\lambda f}{\pi W_0} \quad (4.1)$$

Where  $W_f$  is,

$\lambda$  is

According to the formula, when a cavity with a diameter of 10  $\mu\text{m}$  is aimed;

$$0.005 \text{ mm} = \left( \frac{1.030 \text{ mm} \times \text{focal length}}{\pi \times 0.8 \text{ mm}} \right) \quad (4.2)$$

Thus the focal length is found to be approximately 15 mm. Therefore a lens with a focal length of 15mm is necessary.

The repetition rate to create the 120  $\mu\text{m}$  cavity is calculated as:

To manufacture a cavity with 5  $\mu\text{m}$  radius, with a laser pulse duration of 500 fs, moving a quarter radius after each pulse was preferred. Thus between every single pulse a distance of 1,25  $\mu\text{m}$  is covered as seen in **Figure 4.1**.

For a repetition rate of 1 kHz and length of 120  $\mu\text{m}$  the interval between each pulse should be  $T = 1/F = 10^{-3}$ .  $F$  equals frequency. So to relocate the center of the beam a radius away, it was required to have 5 pulses, considering each after each shot a distance of 1,25  $\mu\text{m}$  was covered as represented in **Figure 4.2**.

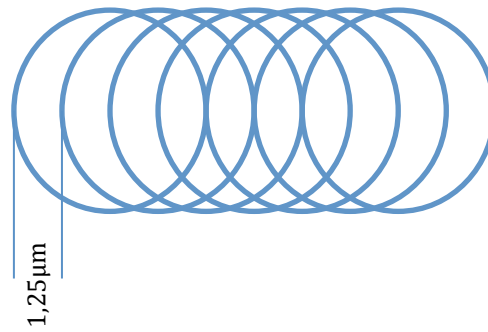


**Figure 4.1** Distance between overlapping pulses

5 μm distance was covered in  $4 \times 10^{-3}$  s. Using the formula:

$$\text{Distance} = \text{Velocity} \times \text{Time Interval} \rightarrow x = v \times t \Rightarrow 5 \mu\text{m} = v \times 4 \times 10^{-3} \text{ s.}$$

Thus the scan speed would be  $v = 1.25$  mm/s (scan speed),

to achieve a 120 μm cavity  $t = 0.096$  s is required. and 120 pulses are needed.

As the number of pulses and scan speed needed to form a 120 μm long cavity with a radius of 5 μm was attained, the parameters were tested at a power level of 0.6 mW and a polarization angle of  $0^\circ$ , with frequency set to 1 kHz as represented in **Figure 4.2**.

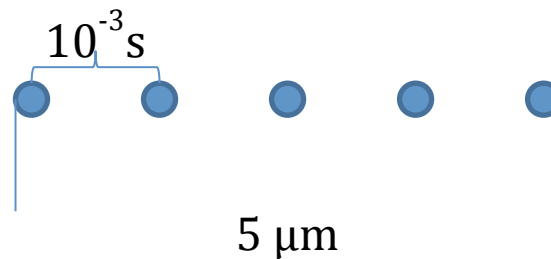


**Figure 4.2** Distance and time interval for five consecutive Femtosecond shots

Ripple like structures formed on the ablated areas as can be seen in **Figure 4.3**. It was discussed in literature [33, 58, 60, 62, 86, 87] that these ripple like structures were formed by the different variations of polarization angle, pulse, fluence and scan speed parameters.

To study the different results of the parameter changes used in the experiment, it was determined to use 1/10 of the frequency amount used in the prior experiment.

The same formula is to be used to calculate how many pulses are required to create a cavity of desired length at the desired scan speed and desired frequency.

**Table 8** Statistical results on the first experiment.

Cavity No.	Scan Speed [ $\mu\text{m/s}$ ]	Pulses	Power [mW]	Frequency [kHz]	Desired Cavity			Actual Cavity			Pulses x Pass Over	Focal Length [mm]	W0 [mm]	Polarizer Angle [ $^\circ$ ]	Ripple Width [ $\mu\text{m}$ ]	Ripple Spacing [ $\mu\text{m}$ ]
					Diameter [ $\mu$ ]	Fluence [ $\text{J/cm}^2$ ]	Energy [ $\mu\text{J}$ ]	Diameter [ $\mu$ ]	Passovers							
Cavity 1	1250	120	0.6	1	12.29	0.506	2	13.424	1	120	15	0.8	$0^\circ$	0.6	0.35	
Cavity 2	1250	120	0.6	1	12.29	0.506	2	13.54	1	120	15	0.8	$0^\circ$	0.52	0.31	
Cavity 3	1250	120	0.6	1	12.29	0.506	2	12.295	1	120	15	0.8	$0^\circ$	0.7	0.49	

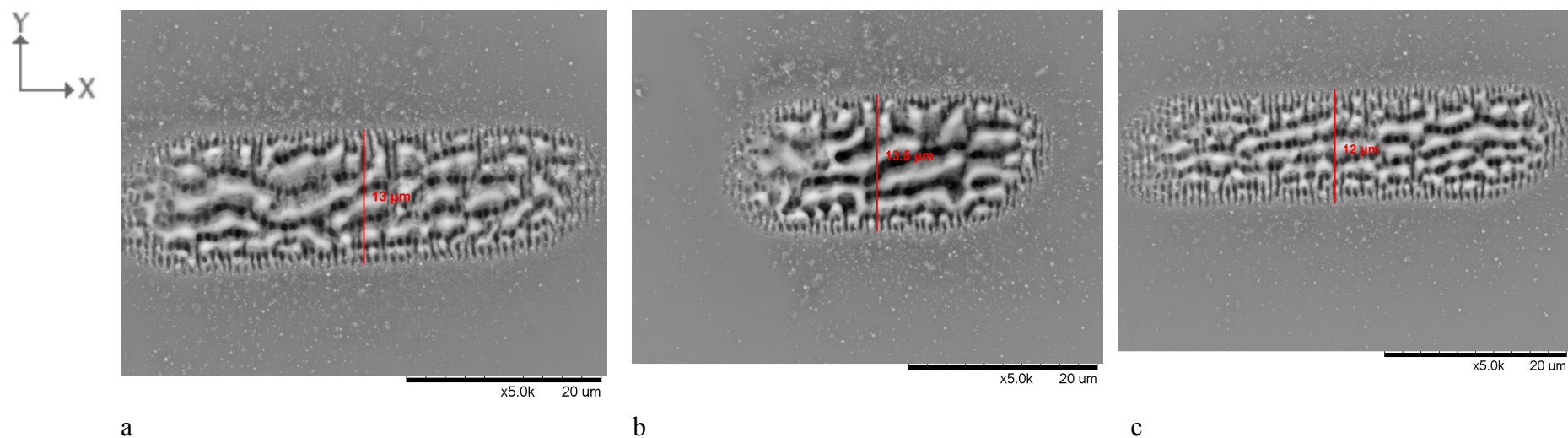


**Figure 4.3** Cavity images showing the formation of ripple like structures. The values are: (a) Focal Length 15 mm, Fluence  $0.506 \text{ J/cm}^2$ , Polarization Angle  $0^\circ$ , Frequency 1 kHz, Scan Speed 1250 (b) Focal Length 15 mm, Fluence  $1.506 \text{ J/cm}^2$ , Polarization Angle  $0^\circ$ , Frequency 1 kHz, Scan Speed 1250 (c) Focal Length 15 mm, Fluence  $0.506 \text{ J/cm}^2$ , Polarization Angle  $0^\circ$ , Frequency 1 kHz, Scan Speed 1250

#### 4.4 Analysis Of Change In Frequency

The aim of this experiment was to achieve a cavity with 5  $\mu\text{m}$  radius and 120  $\mu\text{m}$  length at a laser pulse duration of 500 fs with 1/10 scan speed and a repetition rate of 0.1 kHz at a polarization angle of  $0^\circ$ . Using the same formula from the above mentioned experiment, the parameters to create 120  $\mu\text{m}$  long cavities were determined. With reduced scan speed and frequency, the total pulse number per cavity remains the same, however the pulse amount per second is different.

Comparing the data presented on **Table 8** and **Table 9**, although the total pulse number and pulse per area remains the same, the scan speed and frequency are both reduced to one tenth their original value (**Table 8** to **Table 9**). This means that with ablation at higher frequencies both the cavities and ripples are wider. So even though the total pulse number stays the same, by reducing the scan speed and ablating a cavity of the same length but for ten times the duration, the cavity ablated with higher frequency is wider and deeper. Conclusively the frequency (pulse amount per second) is much more effective than scan speed, total pulse amount and pulse per area.

The comparison of the Actual Cavity Diameter, Ripple Width and Spaces are shown in **Figure 4.4**. As seen in the graphs the ripple spacing and ripple width are directly proportional while the actual cavity diameter is inversely proportional to the others.

Examination of the results of this experiment has shown that ripples as seen on **Figure 4.5** are formed on the material surface. As discussed in the literature [10, 16, 64, 67, 87, 108] the ripples differ based on scan speed, fluence, polarization angle and total pulse amount. Considering the images the cavity diameter is wider at the starting and ending points. These wider parts are due to the excess number of pulses compared to the other parts of the cavity. This excess number of pulses occurs as the shutter is used manually. Thus the lasers start and end time might differ from the actual time (in microseconds) of the beginning to ending of the scan time. So even if the shutter is opened early by a few microseconds, an excess amount of pulses hits the starting point of the cavity since scanning time may start after the laser pulses start hitting the surface area. This had resulted in wider cavity diameters at the end points.

The same principle applies if the shutter is opened later than the beginning of the scan time, even by a few microseconds. This would result in an excess amount of pulses at the end of the cavity since the scanning movement would stop but the pulses continue to accumulate at the end point.

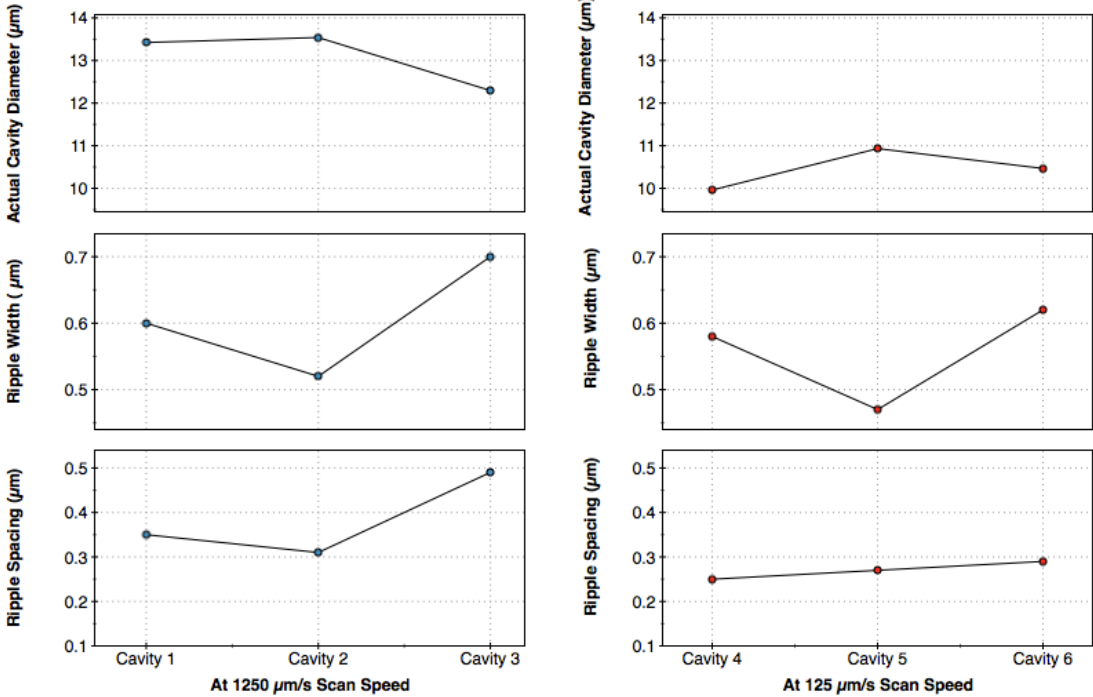


**Figure 4.4** Actual Cavity Diameter, Ripple Width and Spacing comparisons for 1250 μm/s and 125 μm/s Scan Speeds.

Wider and perpendicular ripples were observed at the spots where more pulses than the desired amount accumulated. As discussed in the literature [10, 64, 67, 86, 87, 108] it is reportedly known that these perpendicular ripples are affected by the polarization angle.

Further testing would be required in order to see the differences in ripple formation at 90° and 0° polarization angles. Before continuing with this experiment the spacing between ripples was examined.

**Table 9** Statistical results on the second experiment.

Cavity No.	Scan Speed	Pulses	Power	Frequency	Desired Cavity Diameter	Fluence	Energy	Actual Cavity Diameter	Passovers	Pulses x Pass Over	Focal Length	W0	Polarizer Angle	Ripple Width	Ripple Spacing
	[ $\mu\text{m/s}$ ]		[mW]	[kHz]	[ $\mu$ ]	[J/cm <sup>2</sup> ]	[ $\mu\text{J}$ ]	[ $\mu$ ]			[mm]	[mm]		[ $\mu\text{m}$ ]	[ $\mu\text{m}$ ]
Cavity 4	125	120	0.6	0.1	12.29	0.506	20	9.961	1	120	15	0.8	0°	0.58	0.25
Cavity 5	125	120	0.6	0.1	12.29	0.506	20	10.933	1	120	15	0.8	0°	0.47	0.27
Cavity 6	125	120	0.6	0.1	12.29	0.506	20	10.466	1	120	15	0.8	0°	0.62	0.29

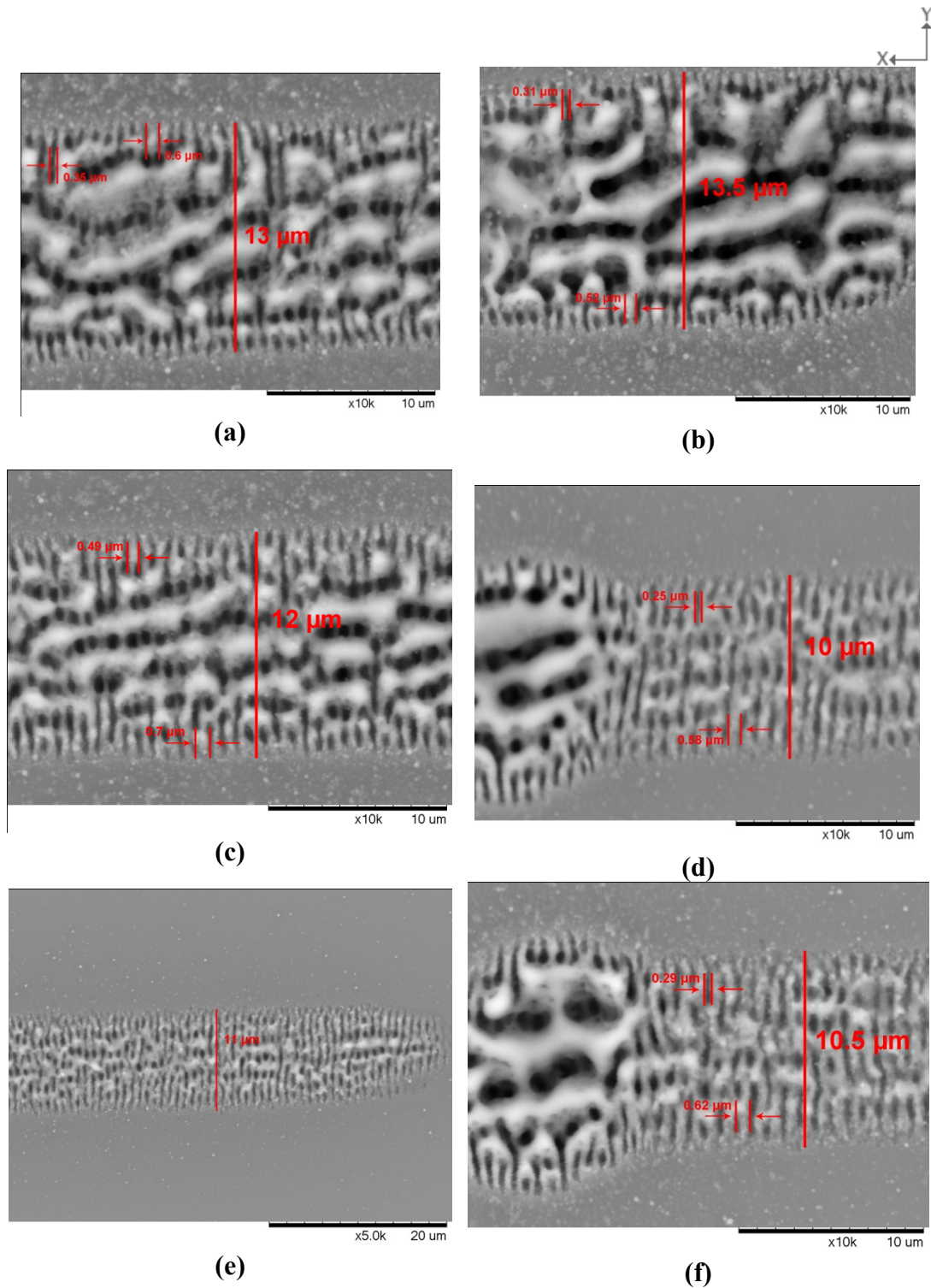


**Figure 4.5** SEM images of cavities 1 to 6 from experiments in 4.3 and 4.4 // (a) F.Length 15 mm, Fluence 1.69 J/cm<sup>2</sup>, P.Angle 0°, Fre. 1 kHz, S.Spd 1250, ripple w. 0.6 // (b) F.Length 15 mm, Fluence 1.69 J/cm<sup>2</sup>, P.Angle 0°, Fre. 1 kHz, S.Spd 1250, ripple w. 0.52 // (c) F.Length 15 mm, Fluence 1.69 J/cm<sup>2</sup>, P.Angle 0°, Fre. 1 kHz, S.Spd 1250, ripple w. 0.7 // (d) F.Length 15 mm, Fluence 16.9 J/cm<sup>2</sup>, P.Angle 0°, Fre. 0.1 kHz, S.Spd 125, ripple w. 0.58 // (e) F.Length 15 mm, Fluence 16.9 J/cm<sup>2</sup>, P.Angle 0°, Fre. 0.1 kHz, S.Spd 125, ripple w. 0.47 // (f) F.Length 15 mm, Fluence 16.9 J/cm<sup>2</sup>, P.Angle 0°, Fre. 0.1 kHz, S.Spd 125, ripple w. 0.62

## 4.5 Ripple Spacing

As observed in the previous experiment, ripples were formed perpendicularly and horizontally successively.

Observing **Figure 4.5** there were white areas within the ripples referred to as ripple width, and black areas referred to as ripple spacing. The ripple width is always greater than the ripple spacing, comparatively around double the size. **Table 10** shows the results of ripple formation at the same fluence rating with different amount of frequencies (pulses per second). As seen on this table both the ripple width and ripple spacing is effected by the change in the amount of pulses per second. The ripple spacing and width increases with the amount of pulses per second.

Referring to **Figure 4.4**, ripple spacing and width is also directly proportional to the Actual Cavity Diameter. This proves ripple formation is a key concept for the creation of a cavity. Further examination has shown that although the amount of pulses is fixed by reducing the scanning speed (ablation time) and the fluence is constant, as the number of pulses per second (frequency) increases both Actual Cavity Diameter and ripple widths increase. While this fact is solid, the change in frequency could not be the only factor in the formation of ripples and changes in their characteristics. As discussed in the literature the polarization angle plays a key part in the formation of ripples, their directions and development [33, 60, 61]. Thus the following experiment was focused on the effects of polarization.

**Table 10** Statistical results of ripple spacing.

Cavity No.	Scan Speed [ $\mu\text{m/s}$ ]	Pulses	Power [mW]	Frequency [kHz]	Desired Cavity Diameter [ $\mu$ ]	Fluence [J/cm <sup>2</sup> ]	Energy [ $\mu\text{J}$ ]	Actual Cavity Diameter [ $\mu$ ]	Passovers	Pulses x Pass Over	Focal Length [mm]	W0 [mm]	Polarizer Angle	Ripple Width [ $\mu\text{m}$ ]	Ripple Spacing [ $\mu\text{m}$ ]
Cavity 1	1250	120	0,6	1	12.29	0,506	2	13.424	1	120	15	0.8	0°	0.6	0.35
Cavity 2	1250	120	0,6	1	12.29	0,506	2	13.54	1	120	15	0.8	0°	0.52	0.31
Cavity 3	1250	120	0,6	1	12.29	0,506	2	12.295	1	120	15	0.8	0°	0.7	0.49
Cavity 4	125	120	0,6	0.1	12.29	0,506	20	9.961	1	120	15	0.8	0°	0.58	0.25
Cavity 5	125	120	0,6	0.1	12.29	0,506	20	10.933	1	120	15	0.8	0°	0.47	0.27
Cavity 6	125	120	0,6	0.1	12.29	0,506	20	10.466	1	120	15	0.8	0°	0.62	0.29

**Table 11** Effects of polarizer angle on surface structures.

Cavity No.	Scan Speed [ $\mu\text{m/s}$ ]	Pulses	Power [mW]	Frequency [kHz]	Desired Cavity Diameter [ $\mu$ ]	Fluence [J/cm <sup>2</sup> ]	Energy [ $\mu\text{J}$ ]	Actual Cavity Diameter [ $\mu$ ]	Passovers	Pulses x Pass Over	Focal Length [mm]	W0 [mm]	Polarizer Angle	Ripple Width [ $\mu\text{m}$ ]	Ripple Spacing [ $\mu\text{m}$ ]
Cavity 7	1000	100	2	1	12.29	1.69	5	16.731	1	100	15	0.8	0°	0.43	0.43
Cavity 8	1000	100	2	1	12.29	1.69	5	23.222	1	100	15	0.8	90°	0.46	0.31

#### 4.6 Effects Of Polarization

As discussed in the literature ripples form proportional to the direction of polarization (the Electric Field Polarization) [33, 58, 60, 62, 86, 87]. Examining **Figure 4.3**, it was observed that ripples are formed bidirectional and they perpendicular to each other. Especially in the areas where too many pulses overlap or where higher levels of energy was used.

Experiments have been run to test the effects of changing polarization angles between  $90^\circ$  and  $0^\circ$  to understand the directional differences in ripples. Laser was set at a pulse duration of 500 fs and a repetition rate of 1 kHz.

SEM images were examined, and the observations have shown that the ripples formed on the irradiated area are parallel to each other.

As seen in **Figure 4.6 (a)**, at  $0^\circ$  polarization the ripples were formed perpendicular to the scanning direction (the x axis). In **Figure 4.6 (b)**, at  $90^\circ$  polarization the ripples were parallel to the scanning direction (the x axis). This explains that the first set of ripples are formed perpendicular to the polarization angle. Furthermore as more pulses convene or higher fluence levels are used a second set of ripples are formed perpendicular to the first type of ripples, horizontal to the polarization angle.

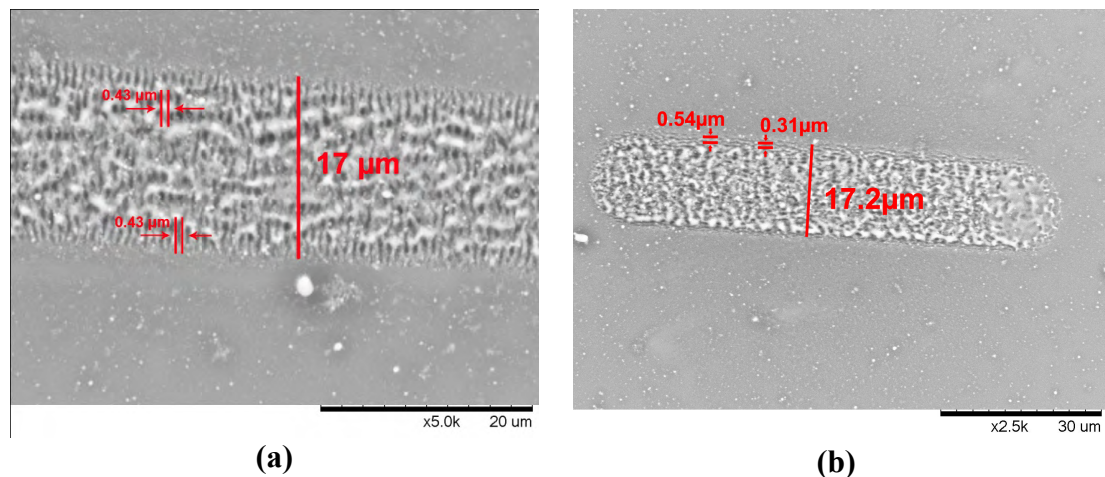


**Figure 4.6** Effects of polarizer angle on surface formations. **(a)** Focal Length 15 mm, Fluence  $4.21\ \text{J}/\text{cm}^2$ , Polarizer Angle  $0^\circ$ , Frequency 1 kHz, Scan Speed 1000. SEM magnification at 5.0k **(b)** Focal Length 15 mm, Fluence  $4.21\ \text{J}/\text{cm}^2$ , Polarizer Angle  $90^\circ$ , Frequency 1 kHz, Scan Speed 1000, SEM magnification at 2.5k

As results of ablations with polarization angles of  $0^\circ$  and  $90^\circ$  are analyzed, it was seen that the increase in the number of pulses results in increased ablation in both x

and y directions, first perpendicular then parallel to the polarization angle. Furthermore this results with an increase of both cavity width and depth.

Since deeper cavities are required for certain applications (i.e. microfluidics), it was decided to increase the laser pulse amount for unit  $\mu\text{m}^2$ . The function generator can increase the number of pulses, but to increase the amount of pulses in unit  $\mu\text{m}^2$  the scanning speed must be reduced. Thus the following experiment was focused on the effects of scan speeds and changes in fluence.

#### 4.7 Effects Of Scan Speed

Experiments were run to observe the effects of power, energy and fluence with different scan speeds with 500 fs laser pulse duration, and a repetition rate of 1 kHz. The experiments values are shown in **Table 12**.

For these experiments the number of pulses was kept fixed at 100. At the first part of the experiment the energy levels of 5, 10, 15, 20  $\mu\text{J}$  was used respectively, at a fixed scan speed of 1000  $\mu\text{m}/\text{s}$ . In the second part of the experiment the energy levels were again set to 5, 10, 15, 20  $\mu\text{J}$ , however this time the scan speed was set to a higher rating of 1500  $\mu\text{m}/\text{s}$ .

The Actual Cavity Diameter and ripple width are directly proportional with the amount of transferred energy as can be seen in **Figure 4.7**. As the fluence increases, so does the Actual Cavity Diameter and ripple width.

**Figure 4.8 (a) and (b)** shows the effects of setting the scan speed at 1000  $\mu\text{m}/\text{s}$  versus setting it to 1500  $\mu\text{m}/\text{s}$ . It was observed that slowing down the scan speed results in wider cavities and ripples, which was expected, since the more number of pulses per area is a direct consequence of reducing the scan speed.

Observing the resulting graphs on **Figure 4.9** that the cavity and ripple widths change according to changes in energy and number of pulses per area, but the ripple spacing is not changed effected by these parameter changes.

**Table 12** Scan Speed comparisons for differing energy fluence and power ranges.

Cavity No.	Scan Speed	Pulses	Power	Frequency	Desired Cavity Diameter	Fluence	Energy	Actual Cavity Diameter	Passovers	Pulses x Pass Over	Focal Length	W0	Polarizer Angle	Ripple Width	Ripple Spacing
	[ $\mu\text{m/s}$ ]		[mW]	[kHz]	[ $\mu$ ]	[J/cm <sup>2</sup> ]	[ $\mu\text{J}$ ]	[ $\mu$ ]			[mm]	[mm]		[ $\mu\text{m}$ ]	[ $\mu\text{m}$ ]
Cavity 9	1000	100	5	1	12.29	4.21	5	17.2	1	100	15	0.8	90°	0.54	0.313
Cavity 10	1000	100	10	1	12.29	8.43	10	20.6	1	100	15	0.8	90°	0.62	0.315
Cavity 11	1000	100	15	1	12.29	12.6	15	23.5	1	100	15	0.8	90°	0.63	0.316
Cavity 12	1000	100	20	1	12.29	16.9	20	25.64	1	100	15	0.8	90°	0.67	0.319
Cavity 13	1500	100	5	1	12.29	4.21	5	11.3	1	100	15	0.8	90°	0.36	0.150
Cavity 14	1500	100	10	1	12.29	8.43	10	13.78	1	100	15	0.8	90°	0.41	0.153
Cavity 15	1500	100	15	1	12.29	12.6	15	22.29	1	100	15	0.8	90°	0.46	0.156
Cavity 16	1500	100	20	1	12.29	16.9	20	24.74	1	100	15	0.8	90°	0.54	0.159

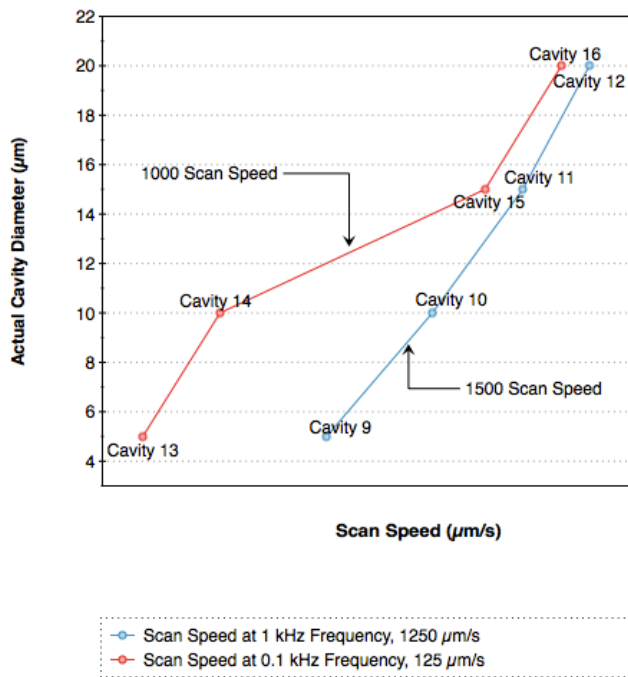


**Figure 4.7** Graph showing the effects of scan speed energy and fluence on cavity depth.

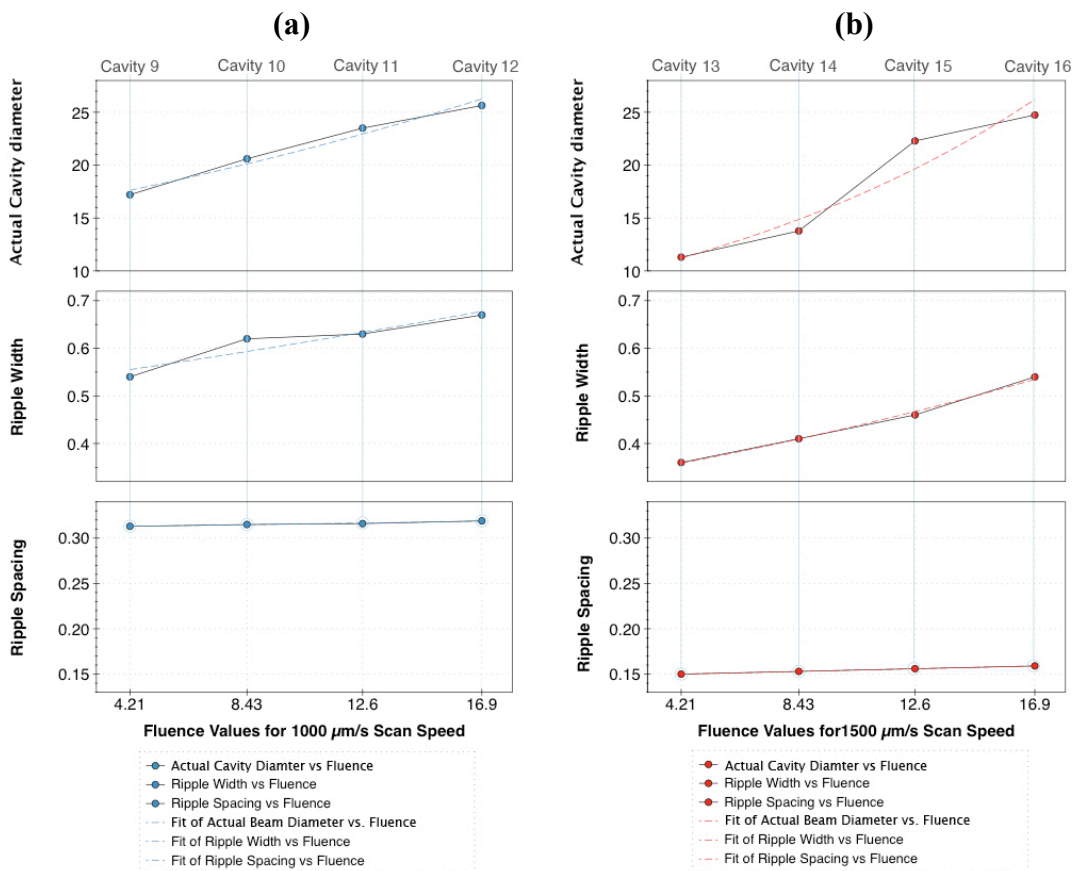


**Figure 4.8** Actual Cavity Diameter, Ripple Width and Spacing compared for 1000 µm/s and 1500µm/s scan speeds. Focal Length: 15 mm.

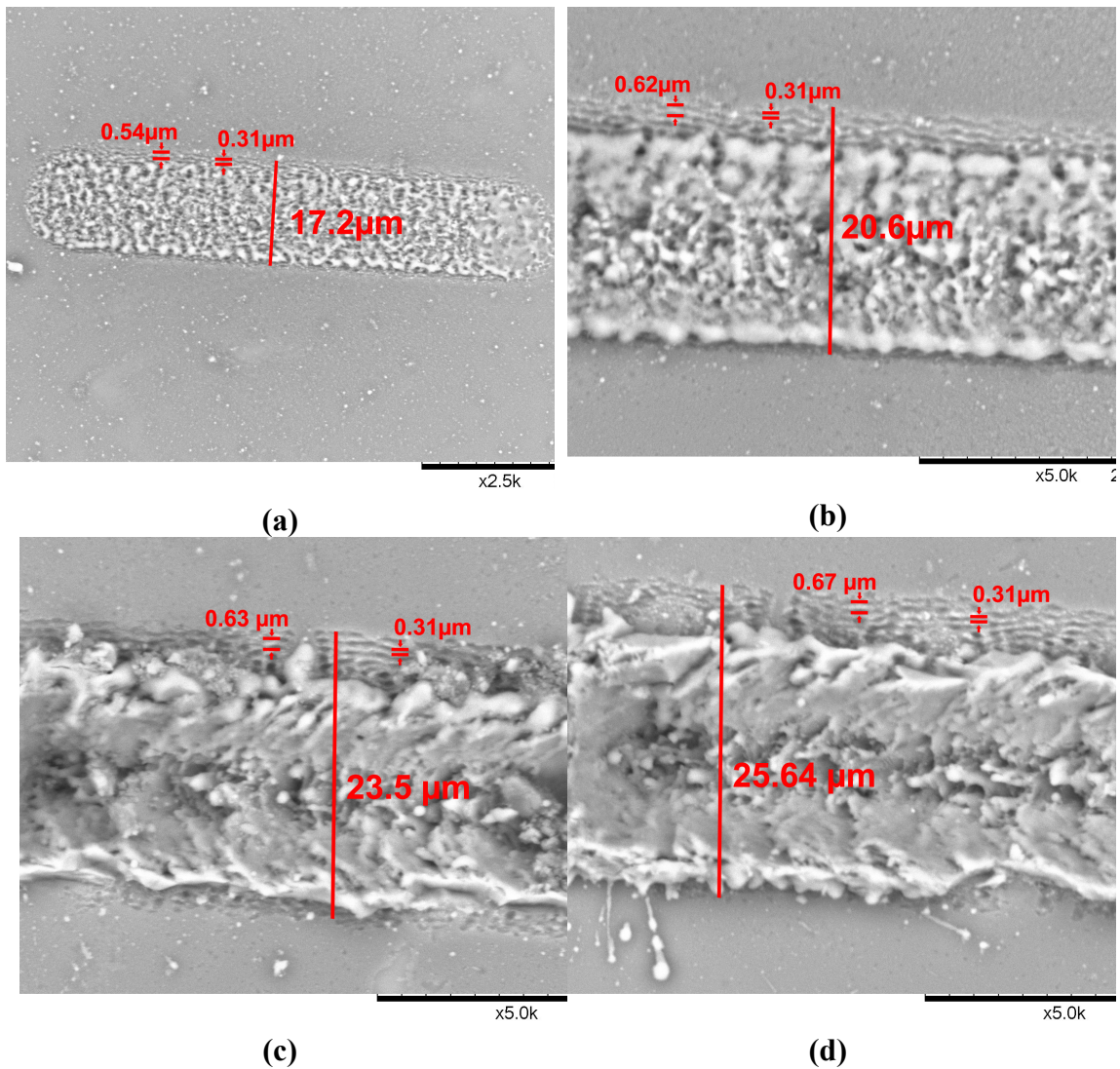


**Figure 4.9** Sem images of cavities 2 through 5 for cavity depth comparison at 1000 scan speed. The values for ripple spacing on these images were approximated. **(a)** Focal Length 15 mm, Fluence  $4.21 \text{ J/cm}^2$ , magnification 2.5k Polarizer Angle  $90^\circ$ , Frequency 1 kHz, Scan Speed 1000, **(b)** Focal Length 15 mm, Fluence  $8.43 \text{ J/cm}^2$ , magnification 2.5k Polarizer Angle  $90^\circ$ , Frequency 1 kHz, Scan Speed 1000, **(c)** Focal Length 15 mm, Fluence  $12.6 \text{ J/cm}^2$ , magnification 5.0k Polarizer Angle  $90^\circ$ , Frequency 1 kHz, Scan Speed 1000, **(d)** Focal Length 15 mm, Fluence  $16.9 \text{ J/cm}^2$ , magnification 5.0k Polarizer Angle  $90^\circ$ , Frequency 1 kHz, Scan Speed 1000

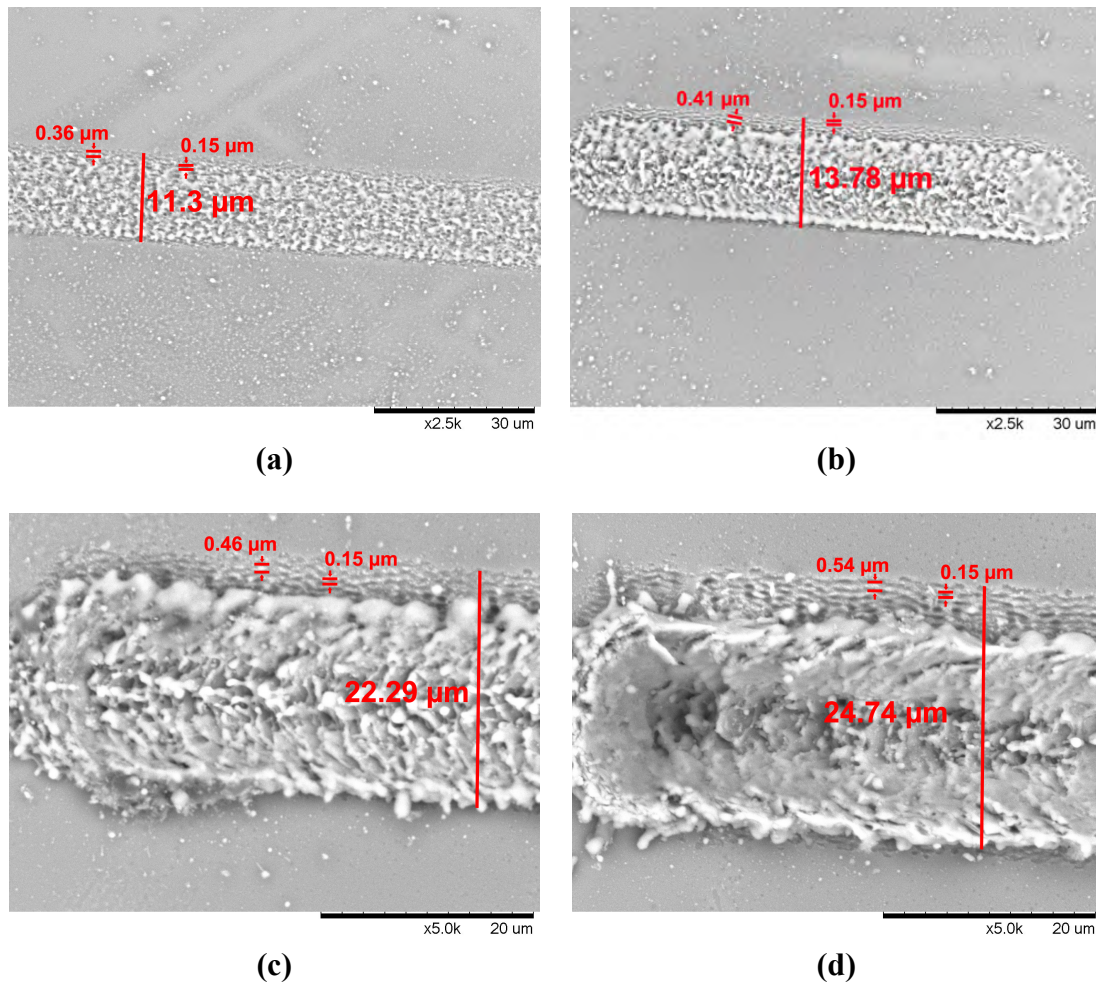


**Figure 4.10** SEM images of cavities 6 through 9 for cavity depth comparison at 1500 scan speed. The values for ripple spacing on these images were approximated. **(a)** Focal Length 15 mm, Fluence  $4.21 \text{ J/cm}^2$ , Polarizer Angle  $90^\circ$ , Frequency 1kHz, Scan Speed 1500, **(b)** Focal Length 15 mm, Fluence  $8.43 \text{ J/cm}^2$ , Polarizer Angle  $90^\circ$ , Frequency 1kHz, Scan Speed 1500, **(c)** Focal Length 15 mm, Fluence  $12.6 \text{ J/cm}^2$ , Polarizer Angle  $90^\circ$ , Frequency 1kHz, Scan Speed 1500, **(d)** Focal Length 15 mm, Fluence  $16.9 \text{ J/cm}^2$ , Polarizer Angle  $90^\circ$ , Frequency 1kHz, Scan Speed 1500.

During these analysis, it was also discussed that the cavities so far were ragged. It would be hard for the fluids to flow smoothly in them. Thus it was decided that more precise holes should be drilled before moving on to cavities. This idea was based on the fact that once precise holes are micromilled, it was only necessary to move the stage to acquire precise cavities. Further experimentation was required to micromill more precise holes.

#### 4.8 Hole Drilling Adjustments

In previous experiments, the surface characteristics of the cavities were rough and weren't deep enough for the microfluidics to flow through. More micromilling

experiments would have to be conducted to achieve these parameters for holes. As holes with desired characteristics is achieved, the data accumulated would be used to create cavities with desired parameters. For this the same mentality in micromilling would be used, except the stage would be moved after desired amount of pulses, the resulting overlapping holes as can be seen in **Figure 4.11** would theoretically result in the creation of cavities with desired characteristics.

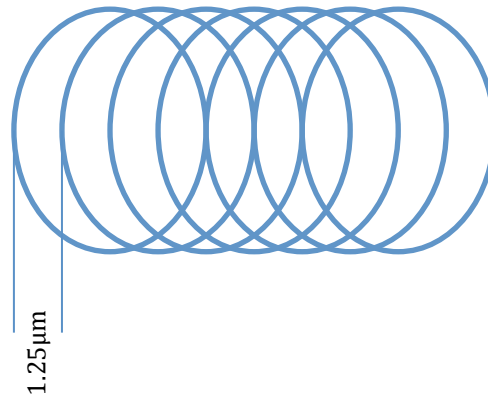


**Figure 4.11** Schematics of overlapping holes to create cavities.

As listed in **Table 13** for this setup laser pulse duration was set to 500 fs with a repetition rate of 1 kHz, with a fixed fluence rate but variable amount of pulses at  $0^\circ$  and  $90^\circ$  polarization angles was used. The resulting data would show which polarization angle is more suitable to create precise holes. Ripples, hole diameters, and hole symmetry was to be examined after the experiments.

As the results were examined in **Figure 4.12** and comparing the cavity lengths in **Table 13**, it was decided that polarization angle of  $90^\circ$  is more suitable to create precise and symmetrical holes, as the holes micromilled with polarization angle of  $90^\circ$  had less ripples and dimples. These results are also to be tested for cavities to observe if they show the same characteristics as the micromilled holes do when ablated with the polarization angle of  $90^\circ$ . After this point it was necessary to test which parameters for pulse amount, energy levels and different parameters of focal length of lens would have to be used to create holes deep and precise enough.

**Table 13** Detailed statistics for holes drilled at experiment 7

Cavity No.	Pulses	Power [mW]	Frequency [kHz]	Desired Cavity Diameter [ $\mu$ ]	Fluence [J/cm <sup>2</sup> ]	Energy [ $\mu$ J]	Actual Cavity Diameter [ $\mu$ ]	Focal Length [mm]	W0 [mm]	Polarizer Angle	Ripple Width [ $\mu$ m]	Ripple Spacing [ $\mu$ m]
Hole 16	300	10	1	12.29	8.43	10	14.163	15	0.8	90°	n/a	n/a
Hole 17	350	10	1	12.29	8.43	10	14.941	15	0.8	90°	n/a	n/a
Hole 18	400	10	1	12.29	8.43	10	15.291	15	0.8	0°	0.5	0.43
Hole 19	600	10	1	12.29	8.43	10	17.743	15	0.8	0°	0.43	0.35
Hole 20	250	10	1	12.29	8.43	10	12.918	15	0.8	0°	0.47	0.31
Hole 21	150	10	1	12.29	8.43	10	11.295	15	0.8	90°	0.35	0.23
Hole 22	500	10	1	12.29	8.43	10	15.603	15	0.8	90°	0.47	0.31
Hole 23	200	10	1	12.29	8.43	10	12.109	15	0.8	90°	0.47	0.31

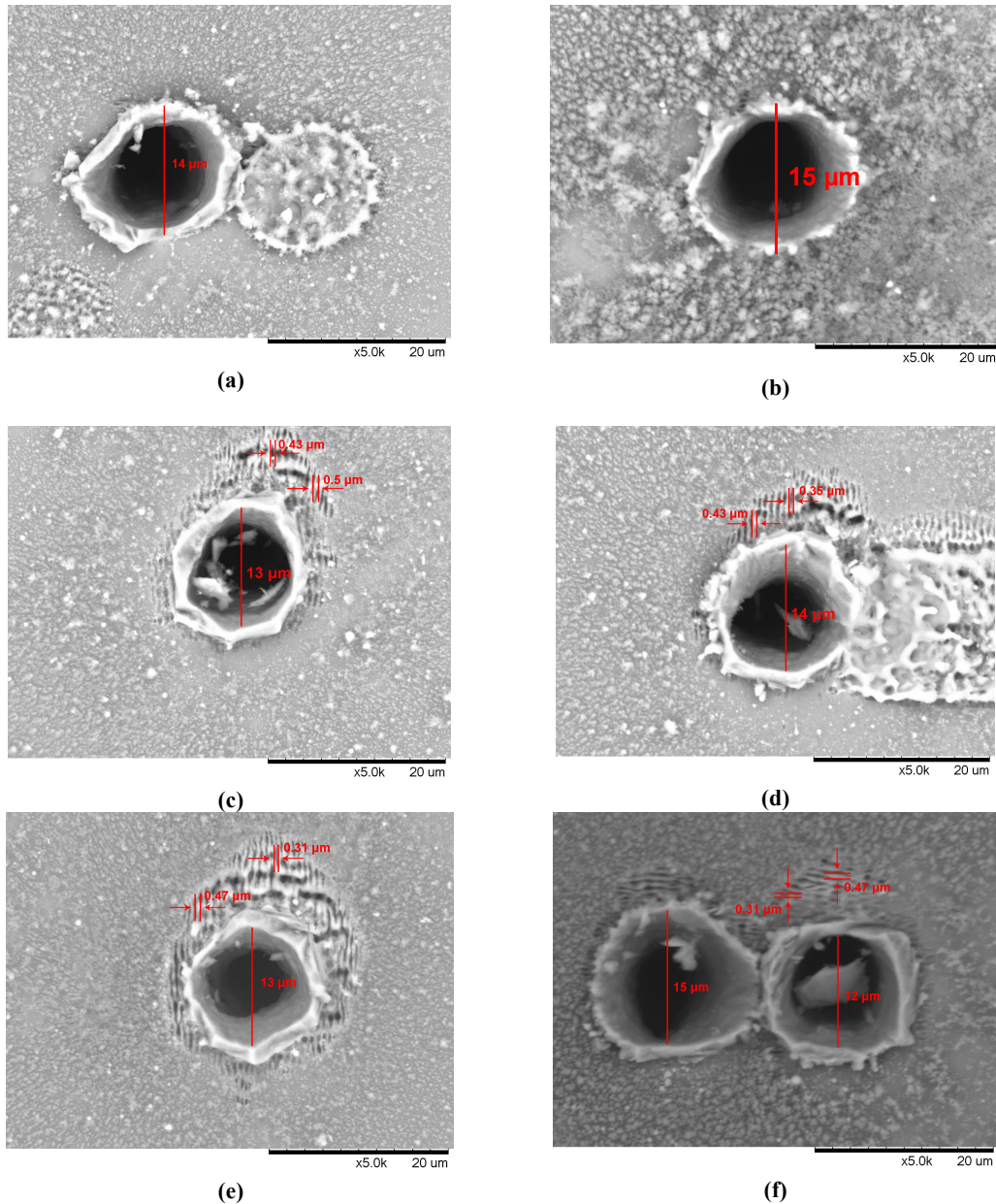


**Figure 4.12** Sem images of holes drilled with different polarization angles (a) Focal Length 15 mm, Fluence 8.43 J/cm<sup>2</sup>, Polarizer 90°, Frequency 1 kHz (b) Focal Length 15 mm, Fluence 8.43 J/cm<sup>2</sup>, Polarizer 90°, Frequency 1 kHz (c) Focal Length 15 mm, Fluence 8.43 J/cm<sup>2</sup>, Polarizer 0°, Frequency 1 kHz (d) Focal Length 15 mm, Fluence 8.43 J/cm<sup>2</sup>, Polarizer 0°, Frequency 1 kHz, (e) Focal Length 15 mm, Fluence 8.43 J/cm<sup>2</sup>, Polarizer 0°, Frequency 1 kHz, (f) Focal Length 15 mm, Fluence 8.43 J/cm<sup>2</sup>, Polarizer 90°, Frequency 1 kHz

#### 4.9 Hole Micromilling With 90° Polarization Angle At 25.4 mm Focal Length

As the results of previous experiments have shown that 90° polarization was much more effective in creating desired holes, the other influential parameters (pulse

amount and fluence) were tested. To create more precise holes using a lens with a focal length of 25.4 mm.

To figure out the differences between various parameters of pulse amount and fluence, holes were micromilled with a fixed polarization angle of  $90^\circ$ , pulse duration of 500 fs, 1 kHz frequency, with varying pulses between 5 and 500 and fluences between  $0.4 \text{ J/cm}^2$  and  $6 \text{ J/cm}^2$ , as listed in **Table 14**.

Considering the data in **Figure 4.13**, it was certain that the hole diameter was directly proportional to the pulse number and fluence. But the SEM images would have to be observed closely to figure out whether the increase in pulse amount or the increase in fluence would be more effective in creating more symmetrical, precise and smooth holes. Since the more effective parameter would be the prioritized parameter to be used in testing the previous results for cavities, using the overlapping technique previously discussed.

As can be seen in **Figure 4.14** both the increase in pulse amount and fluence resulted in wider holes. The holes created with increased number of pulses were much more symmetrical and smoother compared to those created with increased fluence levels. This examination has shown that keeping the pulse per area high and fluence low would result in precise microholes.

Furthermore the resulting asymmetrical holes may have been a result of using lenses with longer focal lengths since they scatter the laser beams to a wider area. So further experimentation would be required to test shorter focal length lenses. Using lenses with less focal length would result in thinner cavities. However the requirements for microfluidics to flow through cavities was wider than what was achieved. But since the primary goal was to create smoother and precise cavities, the wider cavities would have to be achieved by overlapping these thinner cavities side by side later on.

To see whether this theory would apply to creating cavities, experiments with increased number of pulses (achieved by multiple passes over the ablated area) would be run at low fluence levels.

**Table 14** Parameters and results for the twenty one holes drilled with differing energy and fluence ratings.

Cavity No.	Pulses	Power [mW]	Frequency [kHz]	Desired Cavity			Actual Cavity		Focal Length [mm]	W0 [mm]	Polarizer Angle
				Diameter [ $\mu$ ]	Fluence [J/cm <sup>2</sup> ]	Energy [ $\mu$ J]	Diameter [ $\mu$ ]				
Hole 7	50	10	1	20.82	2.94	10	19	25.4	0.8	90°	
Hole 8	50	2	1	20.82	0.587	2	13	25.4	0.8	90°	
Hole 9	50	2	1	20.82	0.587	2	14	25.4	0.8	90°	
Hole 10	25	8	1	20.82	2.35	8	20	25.4	0.8	90°	
Hole 11	25	8	1	20.82	2.35	8	13	25.4	0.8	90°	
Hole 12	50	1.5	1	20.82	0.441	1.5	12	25.4	0.8	90°	
Hole 13	25	3	1	20.82	0.881	3	12	25.4	0.8	90°	
Hole 14	25	4	1	20.82	1.17	4	13	25.4	0.8	90°	
Hole 15	25	8	1	20.82	2.35	8	21	25.4	0.8	90°	
Hole 16	400	20	1	20.82	5.87	20	38	25.4	0.8	90°	
Hole 17	200	15	1	20.82	4.41	15	30	25.4	0.8	90°	
Hole 18	300	18	1	20.82	5.29	18	35	25.4	0.8	90°	
Hole 19	5	2	1	20.82	0.587	2	28.5	25.4	0.8	90°	
Hole 20	5	2	1	20.82	0.587	2	28	25.4	0.8	90°	
Hole 21	50	4	1	20.82	1.17	4	13	25.4	0.8	90°	
Hole 22	25	3	1	20.82	0.881	3	11	25.4	0.8	90°	
Hole 23	500	1.5	1	20.82	0.441	1.5	11	25.4	0.8	90°	
Hole 24	500	1.5	1	20.82	0.441	1.5	9	25.4	0.8	90°	
Hole 25	500	1.5	1	20.82	0.441	1.5	10	25.4	0.8	90°	
Hole 26	500	1.5	1	20.82	0.441	1.5	10	25.4	0.8	90°	
Hole 27	500	1.5	1	20.82	0.441	1.5	9	25.4	0.8	90°	
Hole 28	300	2	1	20.82	0.587	2	11	25.4	0.8	90°	
Hole 29	500	1	1	20.82	0.294	1	13	25.4	0.8	90°	

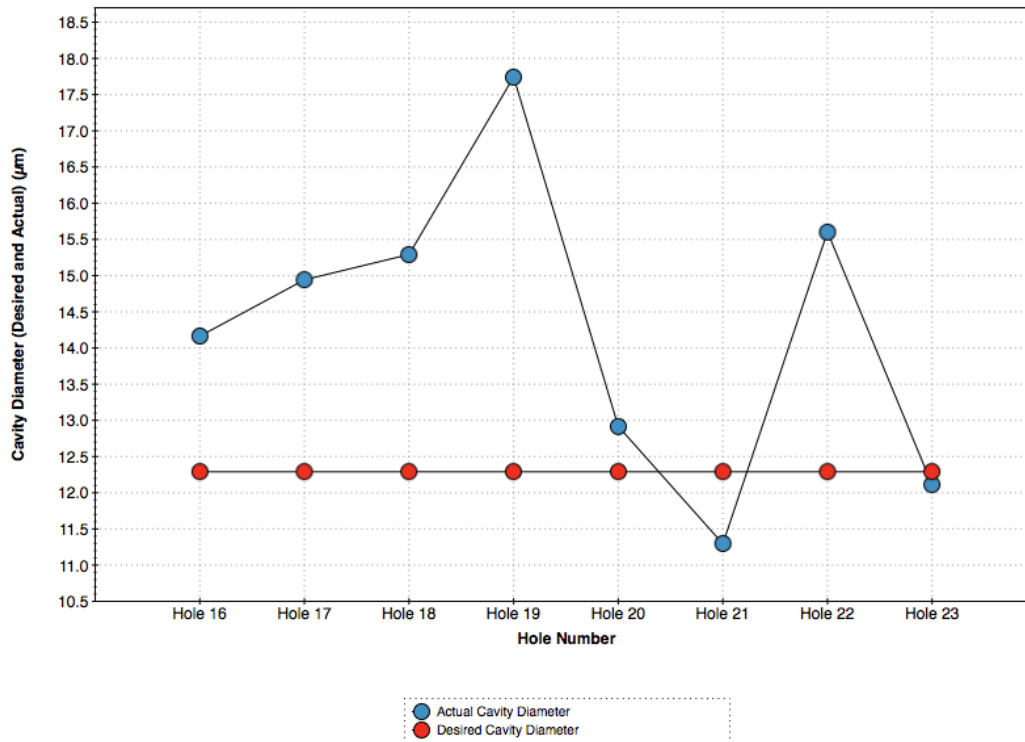


**Figure 4.13** Comparison of Actual Cavity Diameter and Desired Cavity Diameter.

The data gathered from previous experiments was used to resolve issues in cavity precision. Further cavities were to be drilled, this time taking into consideration that low focal length lenses that would have to be used, resulting in thinner cavities.

The next goal in these series of experiments was to go back to creating cavities. To achieve thinner cavities low focal length lenses must be used. But since using lenses with shorter focal length would transform energy per area to higher fluence ratings at given energy levels; the energy levels had to be lowered as well.

Even though some cavities had much better surface properties than others, they were not structured deep enough for certain microfluidics applications. Various cavities with different Passover and cycle numbers have been compared in literature [8, 32]. Differences in multiple Passovers were stated that more pulse per area resulted in wider and deeper cavities. Another factor effecting these differences is the polarization angle. It has been observed in previous experiments that micromilling holes with 90° polarization angle was much more effective compared to 0°, the observation was only for holes, not for cavities. Thus the following experiments were aimed to study the effects of polarization angle and multiple Passovers on cavities using lenses with shorter focal length at polarization angles of 0° and 90°.

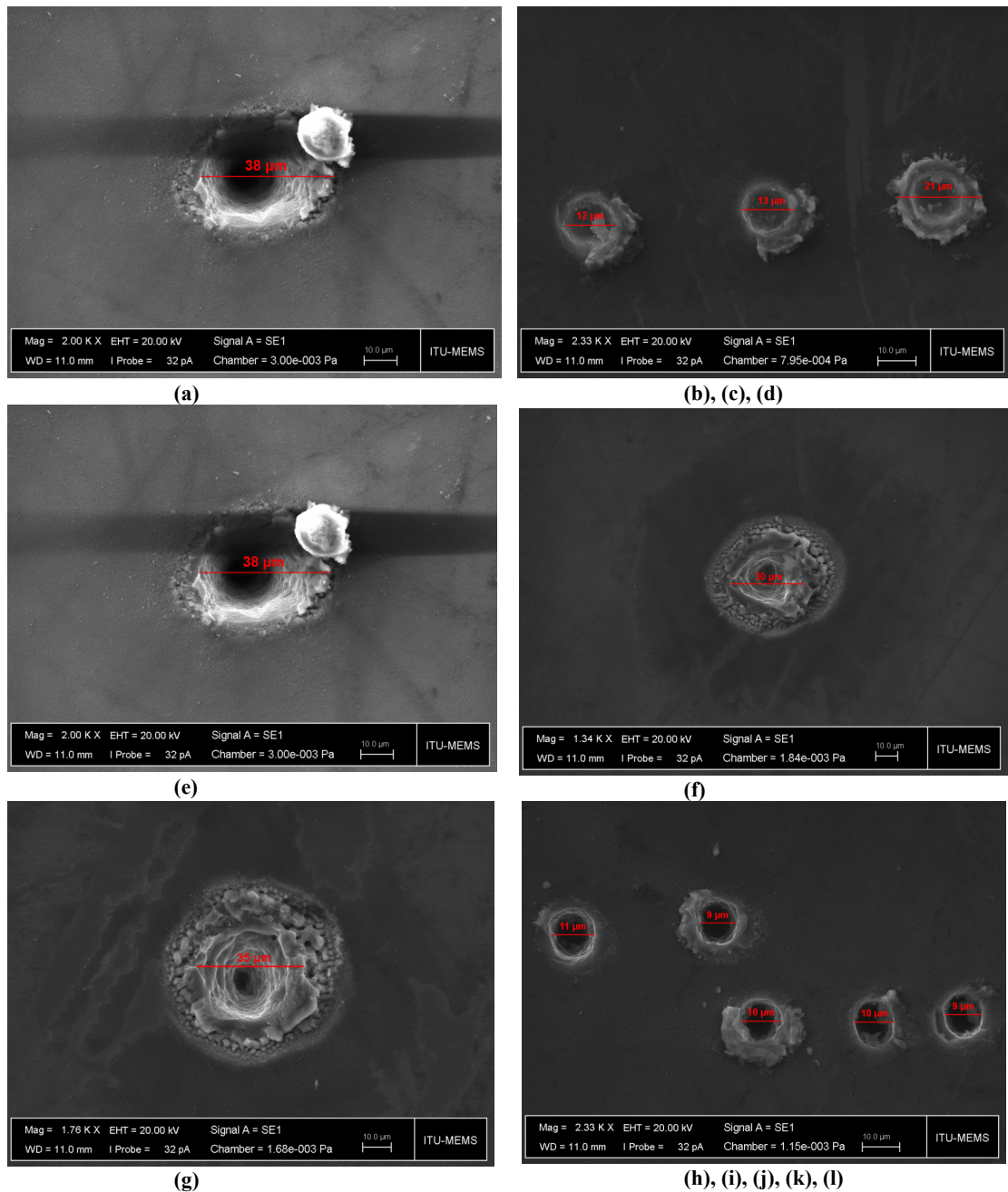


**Figure 4.14** Thumbnail images and statistics for the holes micromilled in this experiment. (a) Focal Length 25.4 mm, Fluence 2.94 J/cm<sup>2</sup>, Polarization Angle 90 °, Frequency 1 kHz (b) Focal Length 25.4 mm, Fluence 0.881 J/cm<sup>2</sup>, Polarization Angle 90 °, Frequency 1 kHz (c) Focal Length 25.4 mm, Fluence 1.17 J/cm<sup>2</sup>, Polarization Angle 90 °, Frequency 1 kHz (d) Focal Length 25.4 mm, Fluence 2.35 J/cm<sup>2</sup>, Polarization Angle 90 °, Frequency 1 kHz (e) Focal Length 25.4 mm, Fluence 5.87 J/cm<sup>2</sup>, Polarization Angle 90 °, Frequency 1 kHz (f) Focal Length 25.4 mm, Fluence 4.41 J/cm<sup>2</sup>, Polarization Angle 90 °, Frequency 1 kHz (g) Focal Length 25.4 mm, Fluence 5.29 J/cm<sup>2</sup>, Polarization Angle 90 °, Frequency 1 kHz (h) Focal Length 25.4 mm, Fluence 0.441 J/cm<sup>2</sup>, Polarization Angle 90 °, Frequency 1 kHz (i) Focal Length 25.4 mm, Fluence 0.441 J/cm<sup>2</sup>, Polarization Angle 90 °, Frequency 1 kHz (j) Focal Length 25.4 mm, Fluence 0.441 J/cm<sup>2</sup>, Polarization Angle 90 °, Frequency 1 kHz (k) Focal Length 25.4 mm, Fluence 0.587 J/cm<sup>2</sup>, Polarization Angle 90 °, Frequency 1 kHz (l) Focal Length 25.4 mm, Fluence 0.294 J/cm<sup>2</sup>, Polarization Angle 90 °, Frequency 1 kHz.

#### 4.10 Passover Studies With Differing Polarization Angles

Effects of multiple Passovers with different polarization angles were tested, with a fixed laser pulse duration of 500 fs and a repetition rate of 1 kHz and a focal length of 15 mm with same amount of pulses for each cavity. Polarization angle differs from cavity to cavity from exactly  $0^\circ$  to  $90^\circ$ . Multiple Passovers would result in increasing the pulse per area. In the experiment the values listed in **Table 15** are used.

As can be seen in **Figure 4.15**, it is obvious that at a high fluence level of  $8.43 \text{ J/cm}^2$  the increase in pulse amount and using  $90^\circ$  polarization angle instead of  $0^\circ$  is much more effective in creating wider cavities. It would still be necessary to observe the SEM images closely to examine whether these cavities are smooth enough for microfluidics

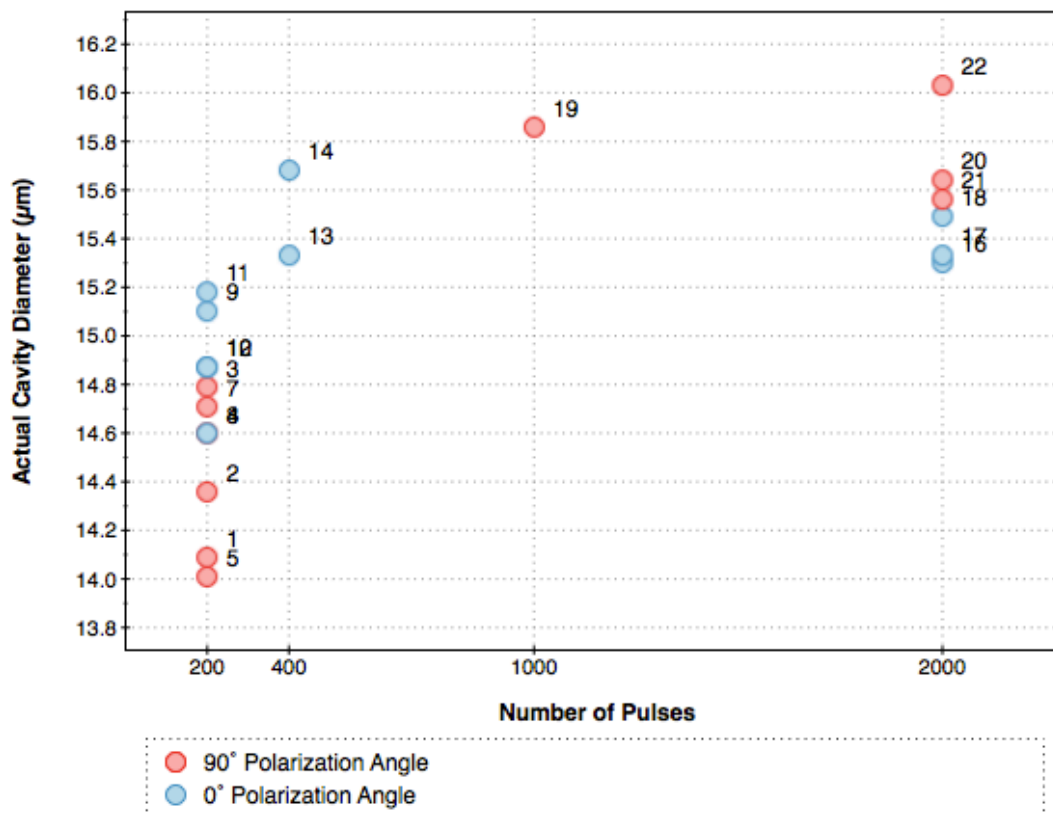


**Figure 4.15** Comparison of Actual Cavity Diameters on various pulses at  $0^\circ$  and  $90^\circ$  polarization. Focal Length: 15 mm. Scan speed is fixed to  $3000 \mu\text{m/s}$  and fluence to  $8.43 \text{ J/cm}^2$ .

**Table 15** Effects of Passover with differentiating polarizer angles

Cavity No.	Scan Speed	Pulses	Power	Frequency	Desired Cavity Diameter	Fluence	Energy	Actual Cavity Diameter	Passovers	Pulses x Pass Over	Focal Length	W0	Polarizer Angle
	[ $\mu\text{m/s}$ ]		[mW]	[kHz]	[ $\mu$ ]	[J/cm <sup>2</sup> ]	[ $\mu\text{J}$ ]	[ $\mu$ ]			[mm]	[mm]	
Cavity 17	3000	200	10	1	12.29	8.43	10	14.09	1	200	15	0.8	90°
Cavity 18	3000	200	10	1	12.29	8.43	10	14.36	1	200	15	0.8	90°
Cavity 19	3000	200	10	1	12.29	8.43	10	14.79	1	200	15	0.8	90°
Cavity 20	3000	200	10	1	12.29	8.43	10	14.60	1	200	15	0.8	90°
Cavity 21	3000	200	10	1	12.29	8.43	10	14.01	1	200	15	0.8	90°
Cavity 22	3000	200	10	1	12.29	8.43	10		1	200	15	0.8	90°
Cavity 23	3000	200	10	1	12.29	8.43	10	14.71	1	200	15	0.8	90°
Cavity 24	3000	200	10	1	12.29	8.43	10	14.60	1	200	15	0.8	0°
Cavity 25	3000	200	10	1	12.29	8.43	10	15.10	1	200	15	0.8	0°
Cavity 26	3000	200	10	1	12.29	8.43	10	14.87	1	200	15	0.8	0°
Cavity 27	3000	200	10	1	12.29	8.43	10	15.18	1	200	15	0.8	0°
Cavity 28	3000	200	10	1	12.29	8.43	10	14.87	1	200	15	0.8	0°
Cavity 29	3000	200	10	1	12.29	8.43	10	15.33	2	400	15	0.8	0°
Cavity 30	3000	200	10	1	12.29	8.43	10	15.68	2	400	15	0.8	0°
Cavity 31	3000	200	10	1	12.29	8.43	10		2	400	15	0.8	0°
Cavity 32	3000	1000	10	1	12.29	8.43	10	15.30	2	2000	15	0.8	0°
Cavity 33	3000	1000	10	1	12.29	8.43	10	15.33	2	2000	15	0.8	0°
Cavity 34	3000	1000	10	1	12.29	8.43	10	15.49	2	2000	15	0.8	0°
Cavity 35	2000	1000	10	1	12.29	8.43	10	15.86	1	1000	15	0.8	90°
Cavity 36	3000	1000	10	1	12.29	8.43	10	15.64	2	2000	15	0.8	90°
Cavity 37	3000	1000	10	1	12.29	8.43	10	15.56	2	2000	15	0.8	90°
Cavity 38	3000	1000	10	1	12.29	8.43	10	16.03	2	2000	15	0.8	90°

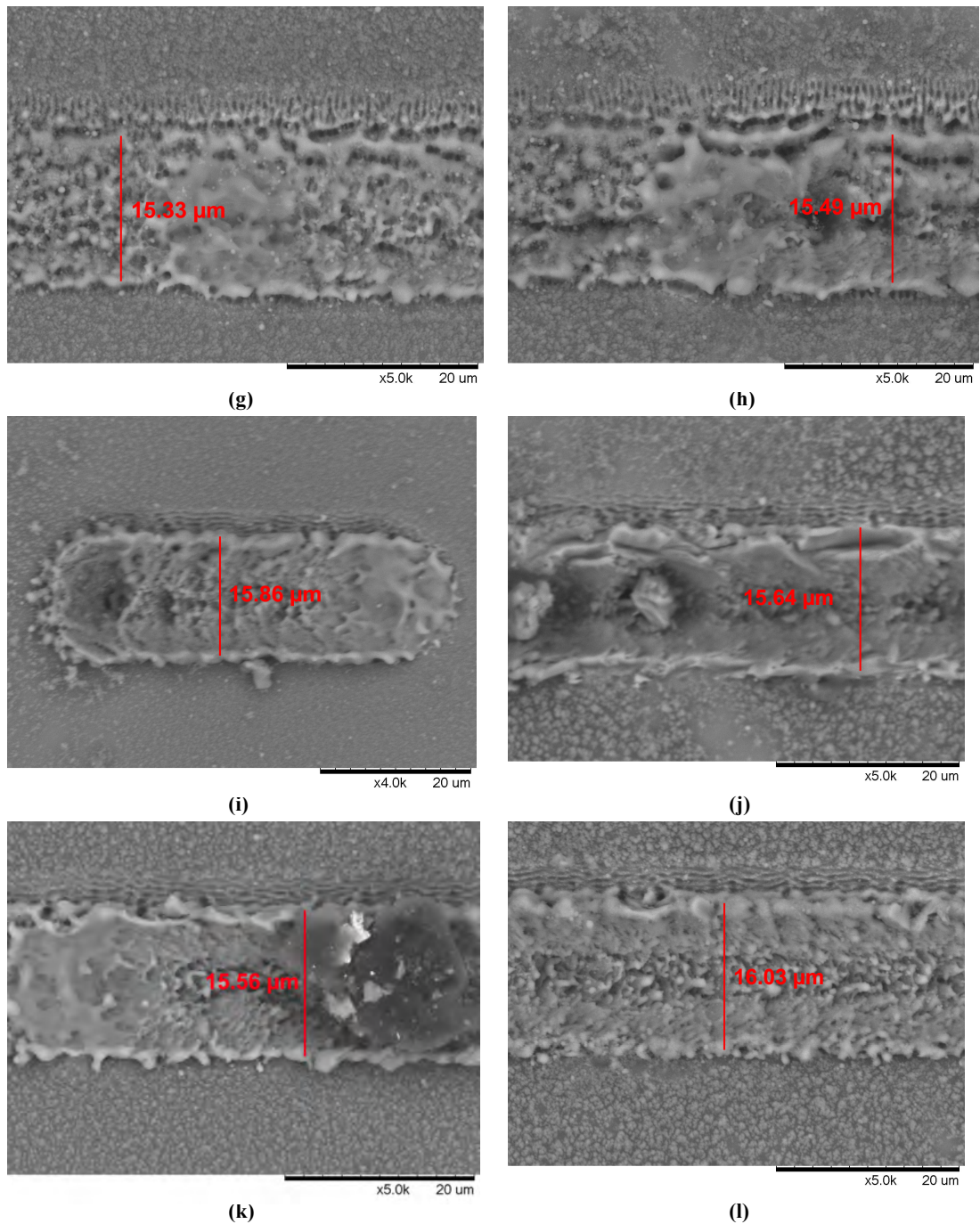


**Figure 4.17** SEM images of the resulting cavities, with Actual Cavity Diameter values. (g) Focal Length 15 mm, Fluence  $8.43 \text{ J/cm}^2$ , Polarization Angle  $0^\circ$ , Frequency 1 kHz, Scan Speed 3000, (h) Focal Length 15 mm, Fluence  $8.43 \text{ J/cm}^2$ , Polarization Angle  $0^\circ$ , Frequency 1 kHz, Scan Speed 3000, (i) Focal Length 15 mm, Fluence  $8.43 \text{ J/cm}^2$ , Polarization Angle  $90^\circ$ , Frequency 1 kHz, Scan Speed 2000, (j) Focal Length 15 mm, Fluence  $8.43 \text{ J/cm}^2$ , Polarization Angle  $90^\circ$ , Frequency 1 kHz, Scan Speed 3000, (k) Focal Length 15 mm, Fluence  $8.43 \text{ J/cm}^2$ , Polarization Angle  $90^\circ$ , Frequency 1 kHz, Scan Speed 3000, (l) Focal Length 15 mm, Fluence  $8.43 \text{ J/cm}^2$ , Polarization Angle  $90^\circ$ , Frequency 1 kHz, Scan Speed 3000

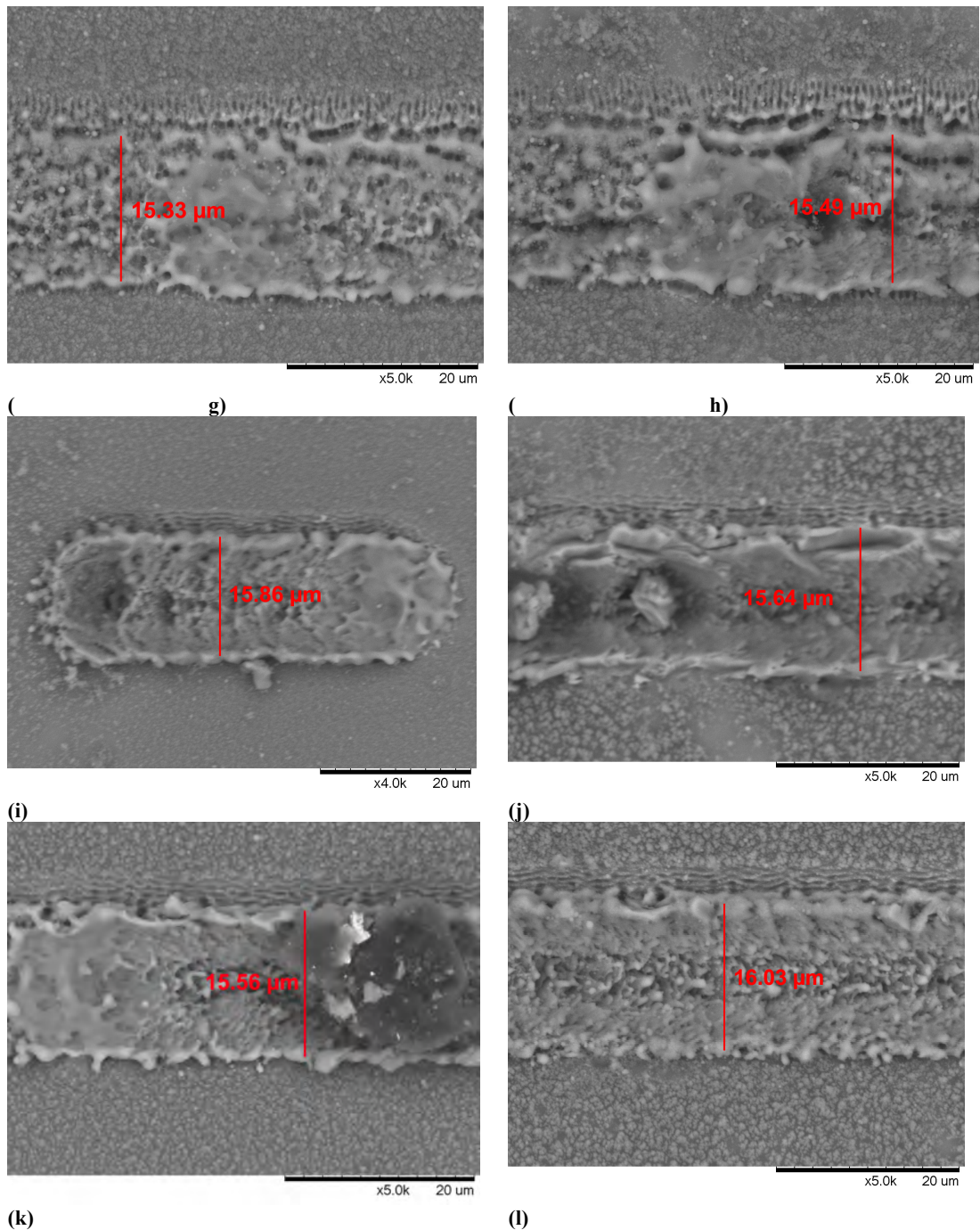


**Figure 4.17** SEM images of the resulting cavities, with Actual Cavity Diameter values. (g) Focal Length 15 mm, Fluence  $8.43 \text{ J/cm}^2$ , Polarization Angle  $0^\circ$ , Frequency 1 kHz, Scan Speed 3000, (h) Focal Length 15 mm, Fluence  $8.43 \text{ J/cm}^2$ , Polarization Angle  $0^\circ$ , Frequency 1 kHz, Scan Speed 3000, (i) Focal Length 15 mm, Fluence  $8.43 \text{ J/cm}^2$ , Polarization Angle  $90^\circ$ , Frequency 1 kHz, Scan Speed 2000, (j) Focal Length 15 mm, Fluence  $8.43 \text{ J/cm}^2$ , Polarization Angle  $90^\circ$ , Frequency 1 kHz, Scan Speed 3000, (k) Focal Length 15 mm, Fluence  $8.43 \text{ J/cm}^2$ , Polarization Angle  $90^\circ$ , Frequency 1 kHz, Scan Speed 3000, (l) Focal Length 15 mm, Fluence  $8.43 \text{ J/cm}^2$ , Polarization Angle  $90^\circ$ , Frequency 1 kHz, Scan Speed 3000

Comparing the thumbnails in **Figure 4.16** and **Figure 4.17** it was seen that the cavities were indeed wide but they were also too rough surfaced with increased amount of dimples, not ideal for microfluidics. This result was decided to be a result of fluence levels much higher than the ablation threshold levels stated in the literature [13, 16, 34, 48, 53, 54, 55, 56, 84, 88]. To figure out the ablation and melting thresholds for this experimental setup and under these circumstances, further experimentation was required.

Experimenting with differentiating pulse and Passovers with different polarization angles has shown that when Passovers are increased so does the depth and width of the cavity. 90° polarization angle is found to be more effective. While proving the effectiveness of 90° polarization angle, the next phase of the experiments is to test which lens is ideal.

To test the results of using different lenses rather than just the 15 mm lens, experiments would have to be run with differing pulse numbers and different scan speeds and energy levels of fluences.

#### **4.11 Scan Speed And Energy Level Tests With 25.4 mm Focal Length**

Experiments were run with a different lens with a focal length of 25.4 mm instead of the previous 15 mm lens. Laser pulse duration was set at 500 fs, with a repetition rate of 1 kHz, differing amount of pulses, with various energy levels at a polarization angle of 90°. The values of the different fluences used in the experiment are listed in **Table 16**.

Examining **Figure 4.18** it was observed that cavity width had increased when the lens was switched with a 25.4 mm focal length lens as expected, while using the same parameters used in previous experiments. To see the effects of the new lens and various parameters of fluence the SEM images were inspected.

While comparing the cavities shown in **Figure 4.19**, drastic differences in Actual Cavity Diameter and Desired Cavity Diameter were observed when energy levels and lens focal length were changed. This has shown that Actual Cavity Diameter is below the Desired Cavity Diameter at very low fluences, the direct contrary effect was observed with very high fluences (Actual Cavity Diameter was above the Desired Cavity Diameter rating).

**Table 16** Statistics of the experiments run to test the effectiveness of 25.4mm Focal Length Lens

	Cavity No.	Scan Speed [ $\mu\text{m/s}$ ]	Pulses	Power [mW]	Frequency [kHz]	Desired Cavity			Scan Length [ $\mu$ ]	Actual Cavity		Pulses x Pass Over	Focal Length mm	W0 mm	Polarizer Angle
						Diameter [ $\mu$ ]	Fluence [J/cm <sup>2</sup> ]	Energy [ $\mu\text{J}$ ]		Diameter [ $\mu$ ]	Passovers				
<b>1<sup>st</sup> Set</b>	Cavity 39	100	20000	2.5	1	20.82	0.734	10	2000	20	1	20000	25.4	0.8	90°
	Cavity 40	100	20000	2.5	1	20.82	0.734	10	2000	18.5	1	20000	25.4	0.8	90°
	Cavity 41	100	20000	2.5	1	20.82	0.734	10	2000	18	1	20000	25.4	0.8	90°
<b>2<sup>nd</sup> Set</b>	Cavity 42	100	20000	1.5	1	20.82	0.441	2	2000	11.5	1	20000	25.4	0.8	90°
	Cavity 43	100	20000	1.5	1	20.82	0.441	2	2000	11	1	20000	25.4	0.8	90°
	Cavity 44	100	20000	1.5	1	20.82	0.441	2	2000	11.5	1	20000	25.4	0.8	90°
	Cavity 45	100	20000	1.5	1	20.82	0.441	2	2000	12	1	20000	25.4	0.8	90°
<b>3<sup>rd</sup> Set</b>	Cavity 46	200	10000	2	1	20.82	0.587	8	2000	16	1	20000	25.4	0.8	90°
	Cavity 47	200	10000	2	1	20.82	0.587	8	2000	18.5	1	20000	25.4	0.8	90°
	Cavity 48	200	10000	2	1	20.82	0.587	8	2000	16	1	20000	25.4	0.8	90°

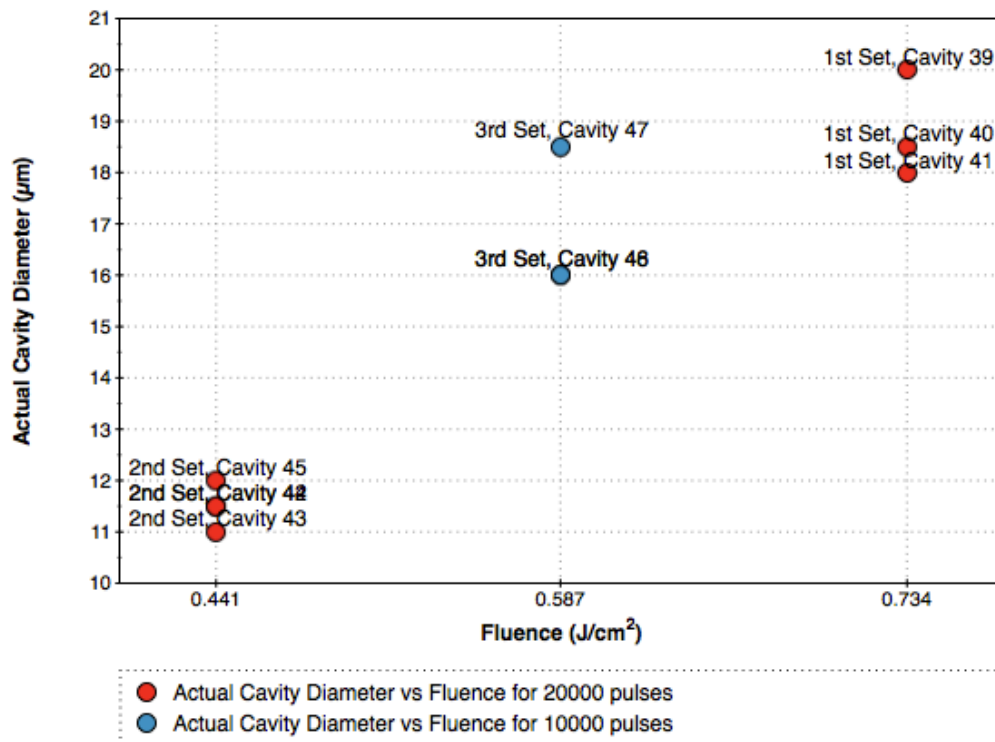


**Figure 4.18** Fluence versus Actual Cavity Diameter Graph. Pulses are 10000 and 20000. Focal Length: 25.4 mm.

The reason behind ripples not occurring in these cavities (as can be seen in the images above) was probably due to the fluences used being above ablation threshold, even though the fluences were very low compared to the other experiments done before. There are indications of ablation and melting threshold values in various references in the literature. [34 , 41, 43, 55, 84] Coupled with these experiments, this shows that melting threshold and ablation threshold affect the dimensions of the cavities and not just their characteristics.

Particularizing this data, experiments were to be run to attain the ablation and melting thresholds. These thresholds are affected by the experimental setup, laser wavelength, pulse duration and various other parameters. Taking into account this wide range of factors, new cavity experiments were run while trying to acquire the Ablation and Melting Thresholds.

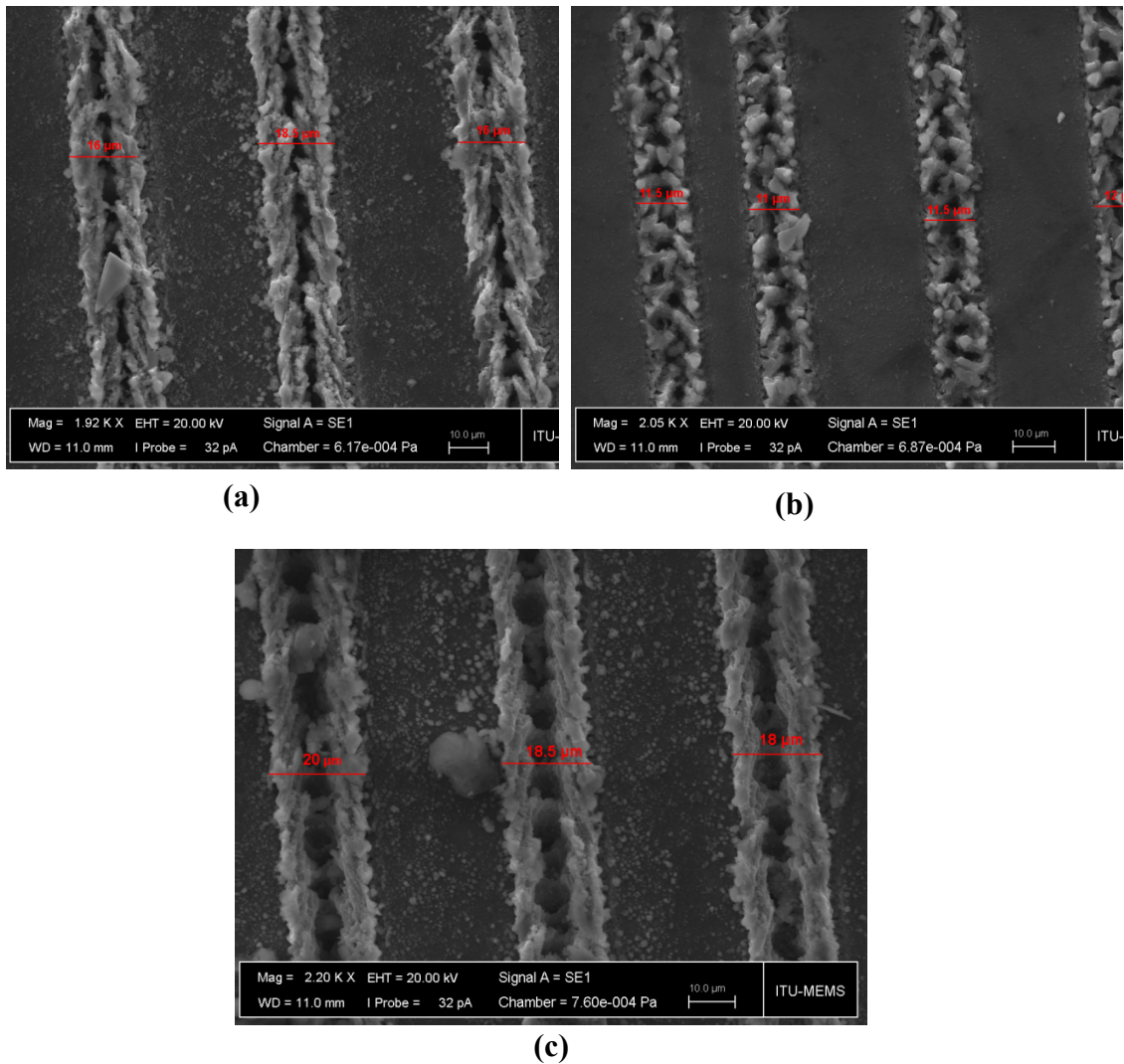


**Figure 4.19** Collective SEM images of cavities micromachined with 25.4 mm Focal Length Lens. (a) Focal Length 25.4 mm, Fluence  $8.43 \text{ J/cm}^2$ , Polarization Angle  $90^\circ$ , Frequency 1 kHz, Scan Speed 100, (b) Focal Length 25.4 mm, Fluence  $1.69 \text{ J/cm}^2$ , Polarization Angle  $90^\circ$ , Frequency 1 kHz, Scan Speed 100, (c) Focal Length 25.4 mm, Fluence  $12.29 \text{ J/cm}^2$ , Polarization Angle  $90^\circ$ , Frequency 1 kHz, Scan Speed 200.

#### 4.12 Melting And Ablation Threshold

To find the melting and ablation thresholds very low levels of fluence was used. There wouldn't be any ablation below the melting threshold, so the lowest fluence level that could ablate the surface area would be the melting threshold of the Si-Wafer. As observed from the literature [13, 16, 34, 48, 53, 54, 55, 56, 84, 88], the ripples did not occur in the center of the ablated area and start to disappear after the ablation threshold is crossed. So the point at which the ripples stop occurring would be the ablation threshold of the Si-Wafer.

For this experiment the laser pulse duration was set at 500 fs, with a repetition rate of 1 kHz, keeping the number of pulses and scan speed constant at a very low level of 10  $\mu\text{m}$  per second, while differentiating energy levels. The polarization angle was  $90^\circ$  with a focal length of 15 mm. The reason of keeping the scan speed as low as it was to increase the pulse per area amount at very low levels of fluence. Since it would be difficult to ablate the bulk material with smaller amounts of pulse per area. The different parameters used in the experiment are listed in **Table 17**.

The surface was irradiated below 0.19 mw energy and  $0.16 \text{ J/cm}^2$  fluence.  $0.16 \text{ J/cm}^2$  is the melting threshold. During this experiment it was noted that the surface could not be machined with the given parameters. As seen in the above images ripples did not occur at fluence level  $0.421 \text{ J/cm}^2$ . So the ablation threshold is confirmed to be between  $0.337$  and  $0.421 \text{ J/cm}^2$ . Furthermore it is observed that when fluence is driven closer to the threshold, the Desired Cavity Diameter is approached.

Referring to the images and the results in **Figure 4.21**, the ablation started at the melting threshold level of  $0.16 \text{ J/cm}^2$ . The ripples started forming after the threshold perpendicular to the polarization. Ripples parallel to the electric field polarization started forming as the pulse amount or fluence is increased. It was observed in the previous experiments that these secondary formation of parallel ripples is mostly the result of increased amount of pulses per area rather than the increase in fluence levels. Increasing the fluence does effect the formation but not as much as increasing the pulse per area amount. Since the pulse number of fluence levels are increased slowly, these ripples start to grow apart from each other and disappear completely when the fluence level reaches that of the ablation threshold.

After the fluence level has reached the ablation threshold, the ripple like formations start to turn into a shape of columnar trapezoid like structures, as the energy levels and/or pulse per area amounts rise the trapezoidal structures first turn into oval structures, then bubble like structures as diagrammed in **Figure 4.22**. As the fluence levels rise, the morphology of the cavities become rough, un-symmetrical and unpredictable.

**Table 17** Statistical data driven from the first cavities of 8 different sets of eperiments.

	Scan				Desired			Actual		Pulses x			Polarizer	
Cavity No.	Speed	Pulses	Power	Frequency	Diameter	Fluence	Energy	Diameter	Passovers	Pass	Focal	W0	Angle	
	[ $\mu\text{m/s}$ ]		[mW]	[kHz]	[ $\mu$ ]	[J/cm <sup>2</sup> ]	[ $\mu\text{J}$ ]	[ $\mu$ ]		Over	Length	[mm]		
1 <sup>st</sup> Set	Cavity 49	10	100000	0.19	1	12.29	0.16	0.19	5	1	100000	15°	0.8	90°
2 <sup>nd</sup> Set	Cavity 50	10	100000	0.25	1	12.29	0.211	0.25	6	1	100000	15	0.8	90°
3 <sup>rd</sup> Set	Cavity 51	10	100000	0.4	1	12.29	0.337	0.4	9	1	100000	15	0.8	90°
4 <sup>th</sup> Set	Cavity 52	10	100000	1	1	12.29	0.843	1	10	1	100000	15	0.8	90°
5 <sup>th</sup> Set	Cavity 53	10	100000	2	1	12.29	1.69	2	10	1	100000	15	0.8	90°
6 <sup>th</sup> Set	Cavity 54	10	100000	0.25	1	12.29	0.211	0.25	10	5	500000	15	0.8	90°
7 <sup>th</sup> Set	Cavity 55	10	100000	1	1	12.29	0.843	1	10	1	500000	15	0.8	90°
8 <sup>th</sup> Set	Cavity 56	10	100000	0.5	1	12.29	0.421	0.5	12	1	500000	15	0.8	90°

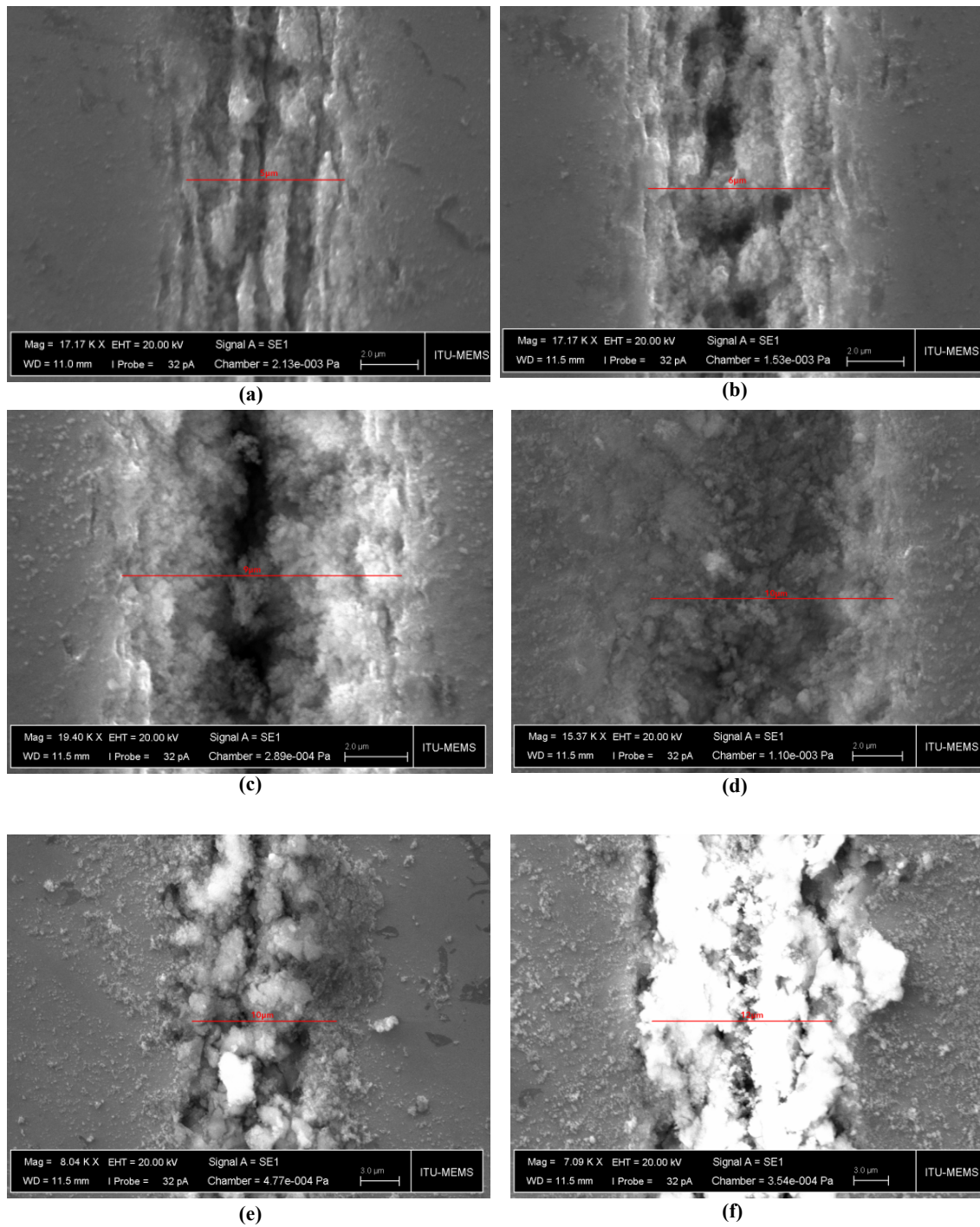


**Figure 4.20** SEM images of resulting cavities (a), Focal Length 15 mm, Fluence  $0.16 \text{ J/cm}^2$ , Polarization Angle  $90^\circ$ , Frequency 1kHz, Scan Speed 10 (b) Focal Length 15 mm, Fluence  $0.211 \text{ J/cm}^2$ , Polarization Angle  $90^\circ$ , Frequency 1 kHz, Scan Speed 10 (c) Focal Length 15 mm, Fluence  $0.337 \text{ J/cm}^2$ , Polarization Angle  $90^\circ$ , Frequency 1 kHz, Scan Speed 10 (d) Focal Length 15 mm, Fluence  $0.843 \text{ J/cm}^2$ , Polarization Angle  $90^\circ$ , Frequency 1 kHz, Scan Speed 10, (e) Focal Length 15 mm, Fluence  $0.843 \text{ J/cm}^2$ , Polarization Angle  $90^\circ$ , Frequency 1 kHz, Scan Speed 10, (f) Focal Length 15 mm, Fluence  $0.421 \text{ J/cm}^2$ , Polarization Angle  $90^\circ$ , Frequency 1 kHz, Scan Speed 10.

When the surface is irradiated between the melting and ablation thresholds, Actual Cavity Diameter is closer to the Desired Cavity Diameter. Aside from that the cavities were more predictable in diameter, the surface was more symmetrical and smoother compared to the cavities ablated at higher energy levels of fluence. But the cavities don't reach the required depth. Considering the literature [8, 32] to achieve cavities with the Desired Cavity Diameter all the while reaching the desired depth, number of laser beam radiating cycles on cavities were increased, while using a very low scan speed to increase the amount of pulses per area, to achieve smoother and symmetrical morphology of the cavities, the fluence is kept at low levels.

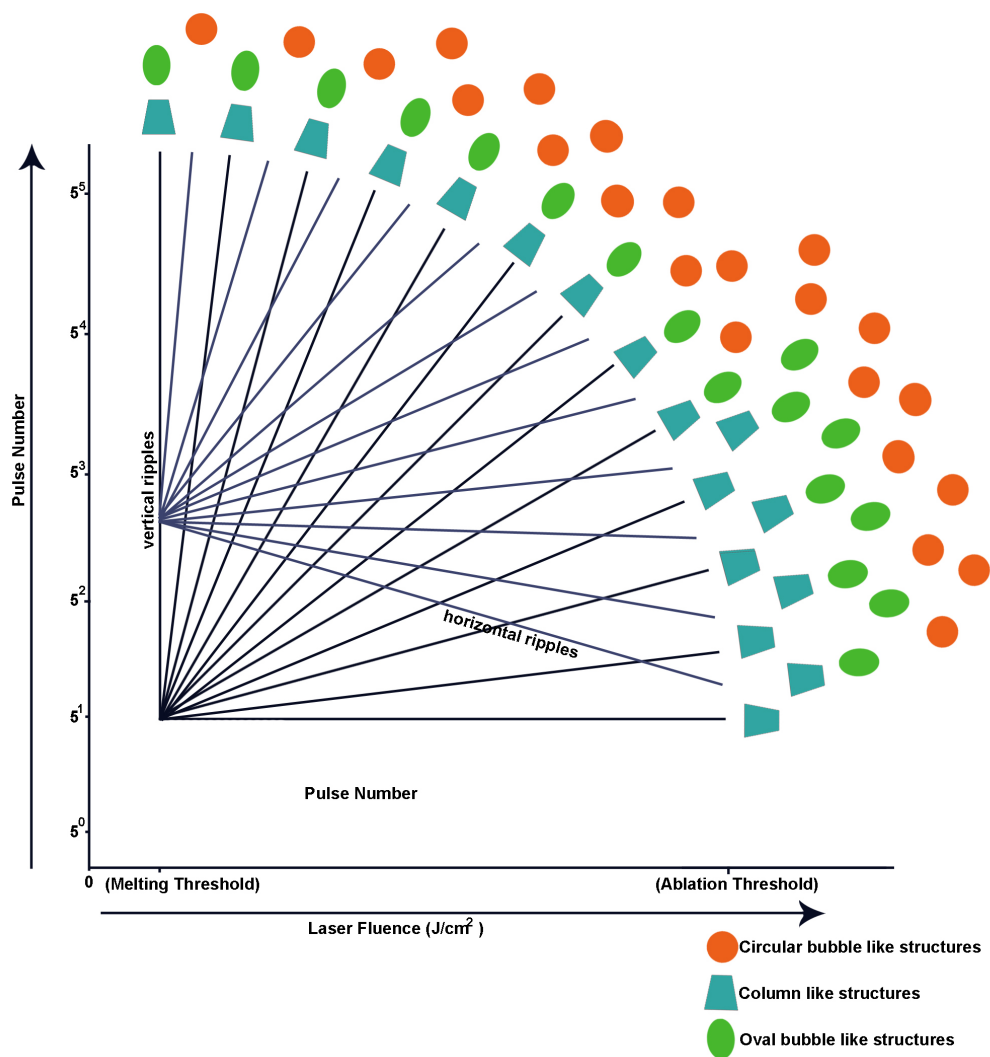


**Figure 4.21** Microstructures formed on SI-Wafer surface at threshold values.

According to these thresholds surface morphology is said to occur in the following sequence:

1. Ripples are formed
2. Spikes are formed
3. Bubbles are formed
4. Threshold is reached
5. Threshold is breached and surface excavation begins

#### 4.13 The Effects Of Scan Speed / Cycle-Passover / Pulse Amount On Ripple Formation At Threshold Fluence Levels

Experiments were run to find the effects of low scanspeed and very high amounts of cycle/Passover and pulse amount on surface morphologies using a fixed pulse duration of 500 fs, with a repetition rate of 1 kHz, at 90° polarization, using the 15mm focal length lens at different low fluence levels between the melting and ablation thresholds as shown in **Table 18**.

As seen in **Figure 4.22**, Actual Cavity Diameter, ripple spacing and width increase when the fluence is increased, as this also causes an increase in the number of pulses.

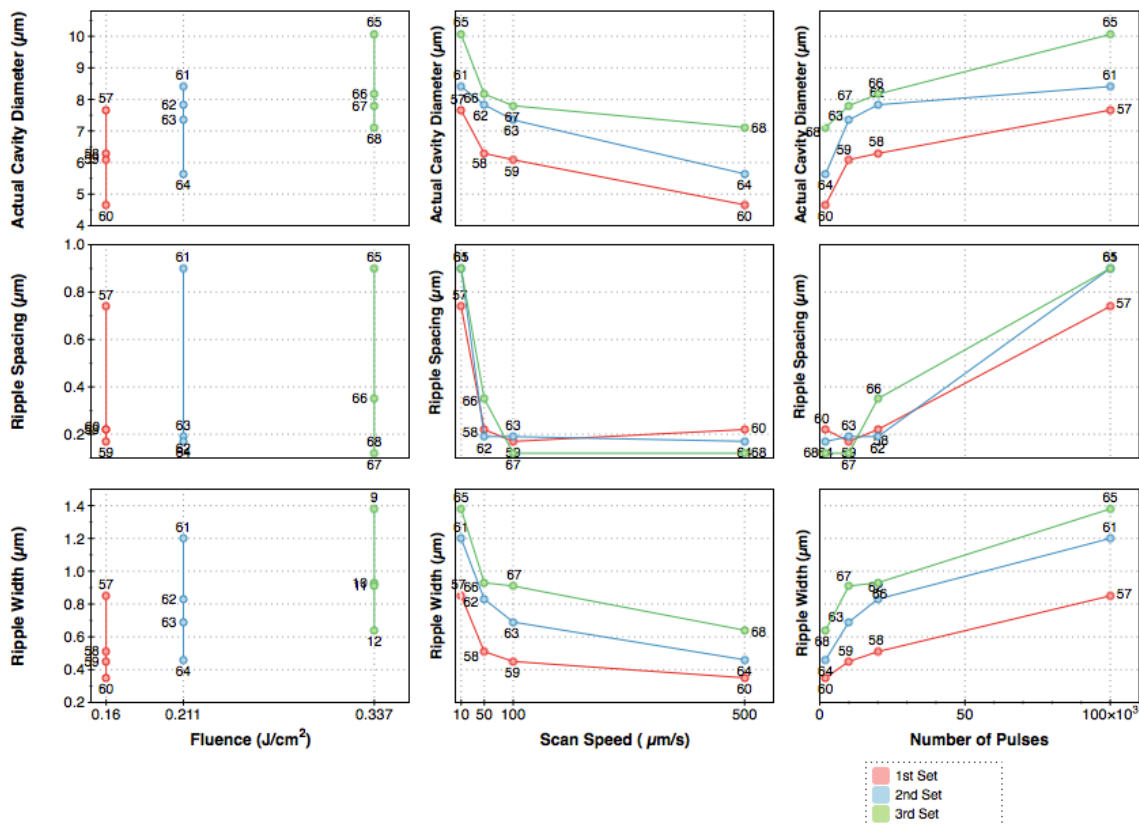


**Figure 4.22** Actual Cavity Diameter, Ripple Spacing and Width comparisons for different fluence, scan speed and numbers of pulses for the first 12 cavities. Focal Length: 15 mm.

**Table 18** Detailed comparisons for scan speed, cycles, and amount of pulses.

Cavity No.	Scan Speed	Pulses	Power	Frequency	Desired	Fluence	Energy	Actual	Pulses x Passovers	Pass Over	Focal Length	W0	Polarizer Angle	Ripple Width	Ripple Spacing
					Cavity Diameter			Cavity Diameter							
	[ $\mu\text{m/s}$ ]		[mW]	[kHz]	[ $\mu$ ]	[J/cm <sup>2</sup> ]	[ $\mu\text{J}$ ]	[ $\mu$ ]			[mm]	[mm]		[ $\mu\text{m}$ ]	[ $\mu\text{m}$ ]
Cavity 57	10	100,000	0.19	1	12.29	0.16	0.19	7.66	1	10000	15	0.8	90°	0.85	0.74
Cavity 58	50	20,000	0.19	1	12.29	0.16	0.19	6.29	1	20000	15	0.8	90°	0.51	0.22
Cavity 59	100	10,000	0.19	1	12.29	0.16	0.19	6.09	1	10000	15	0.8	90°	0.45	0.17
Cavity 60	500	2,000	0.19	1	12.29	0.16	0.19	4.66	1	2000	15	0.8	90°	0.35	0.22
Cavity 61	10	100,000	0.25	1	12.29	0.211	0.25	8.41	1	100000	15	0.8	90°	1.2	0.9
Cavity 62	50	20,000	0.25	1	12.29	0.211	0.25	7.83	1	20000	15	0.8	90°	0.83	0.19
Cavity 63	100	10,000	0.25	1	12.29	0.211	0.25	7.35	1	10000	15	0.8	90°	0.69	0.19
Cavity 64	500	2,000	0.25	1	12.29	0.211	0.25	5.64	1	2000	15	0.8	90°	0.46	0.17
Cavity 65	10	100,000	0.4	1	12.29	0.337	0.4	10.06	1	100000	15	0.8	90°	1.38	0.90
Cavity 66	50	20,000	0.4	1	12.29	0.337	0.4	8.17	1	20000	15	0.8	90°	0.93	0.35
Cavity 67	100	10,000	0.4	1	12.29	0.337	0.4	7.80	1	10000	15	0.8	90°	0.91	0.12
Cavity 68	500	2,000	0.4	1	12.29	0.337	0.4	7.11	1	2000	15	0.8	90°	0.64	0.12

Strangely the reaction of the ripples differs as the scan speed is increased. They react like an “Asymptote” in mathematics. They get smaller after reaching a certain scan speed and stay at that size without disappearing, like an “asymptote” in mathematics. As it gets closer to the axis but never reaches zero and lasts until infinity.

Using these parameters cavity width would be closer to Desired Cavity Diameter but the cavities were not deep enough, thus as seen in the literature [3, 7, 8, 28, 30, 31, 32, 33, 91] using low fluence ratings and low scan speeds to accumulate a high amount of pulses on the ablated area would result in cavities with desired diameters and depth, with less non-uniform surface characteristics which can be observed in **Figure 4.23** and **Figure 4.24**. The aim in the next part of this experiment was to find the effects different scan speeds with multiple cycles-passovers and eventually multiplied pulse amount on cavity width and depth. Laser pulse duration was set to 500 fs with a repetition rate of 1 kHz, with different amount of pulses and scan speed also with differing energy levels using a lens with a focal length of 15 mm as listed in **Table 19**.

Since SEM images are taken from 90° on top of the image, it is hard to tell if the cavities are deep, or the multiple passover theory of creating deeper cavities worked. Despite what is said in the literature [8, 32] and what has been observed in previous experiments, the SEM images show that the cavities, which are ablated with multiple passovers at higher pulse amounts per area, look chaotic with all the non-uniform surface involved. This could be a result of the pulse per area amount being much higher than previous experiments, or a result of the cavities depth. Since the SEM images in **Figure 4.25** and **Figure 4.26** are in two dimensions all the angles of the surface are projected onto a single axis. To make sure images were taken at a 45° angle to view the cavities in three dimensions, and observe the depth further.

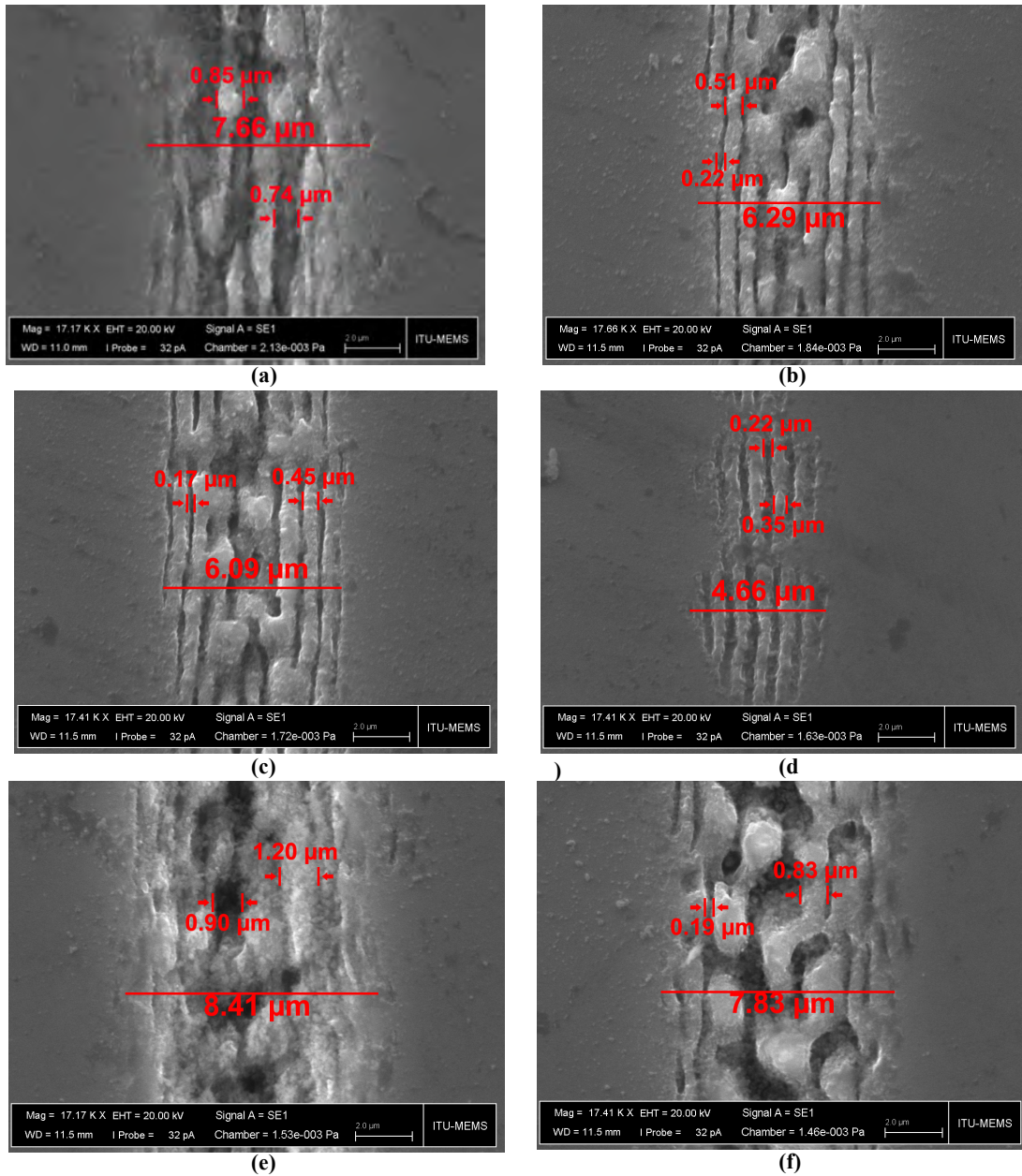


**Figure 4.23** SEM images of first series of 6 cavities. (a), Focal Length 15 mm, Fluence 0.16 J/cm<sup>2</sup>, Polarization Angle 90°, Frequency 1kHz, Scan Speed 10, (b) Focal Length 15 mm, Fluence 0.16 J/cm<sup>2</sup>, Polarization Angle 90°, Frequency 1kHz, Scan Speed 50, (c) Focal Length 15 mm, Fluence 0.16 J/cm<sup>2</sup>, Polarization Angle 90°, Frequency 1 kHz, Scan Speed 100, (d) Focal Length 15 mm, Fluence 0.16 J/cm<sup>2</sup>, Polarization Angle 90°, Frequency 1 kHz, Scan Speed 500, (e) Focal Length 15 mm, Fluence 0.211 J/cm<sup>2</sup>, Polarization Angle 90°, Frequency 1 kHz, Scan Speed 10, (f) Focal Length 15 mm, Fluence 0.211 J/cm<sup>2</sup>, Polarization Angle 90°, Frequency 1 kHz, Scan Speed 50

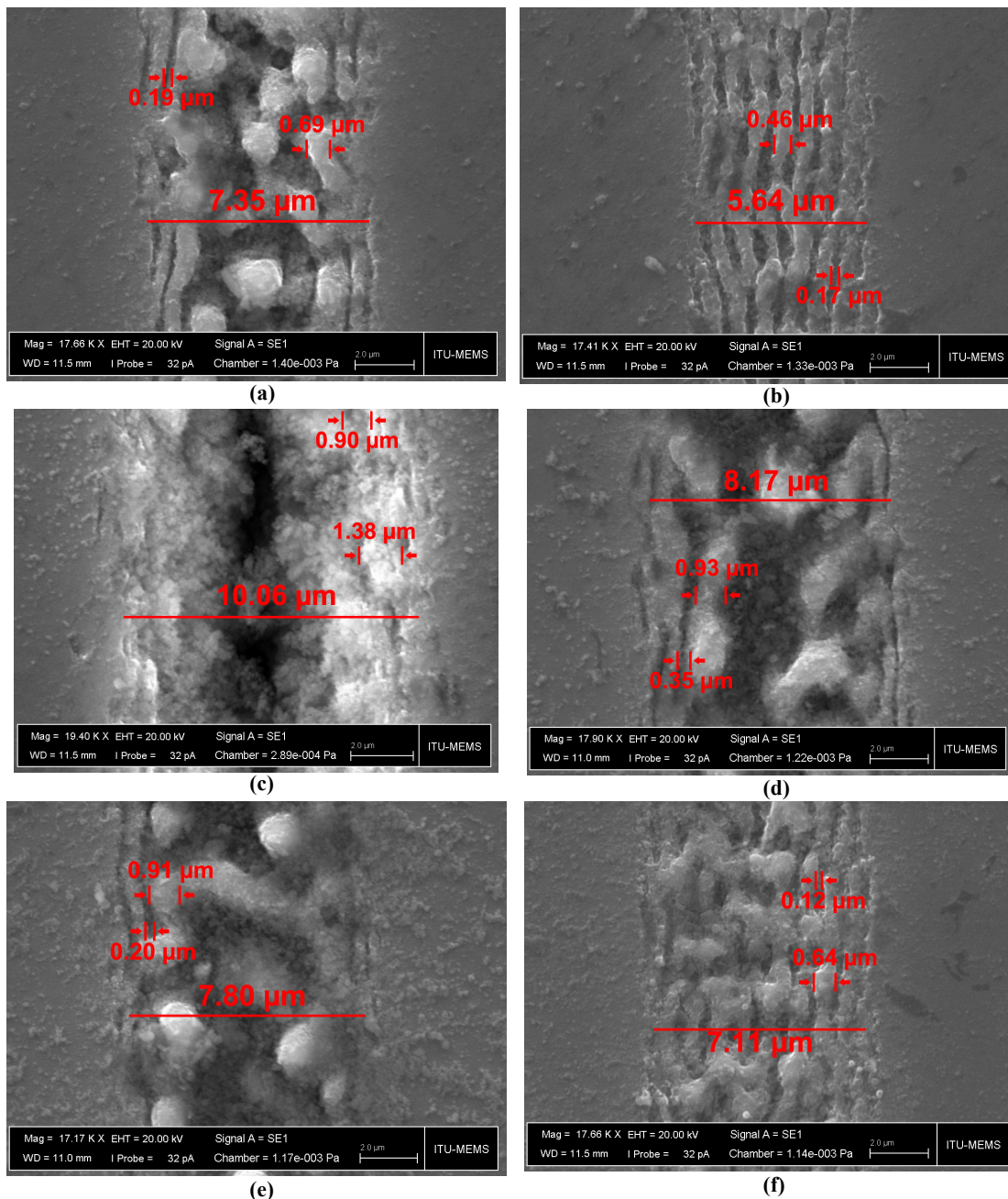


**Figure 4.24** SEM images of second series of 6 cavities, with ripple formations. (a) Focal Length 15 mm, Fluence 0.211 J/cm<sup>2</sup>, Polarization Angle 90 °, Frequency 1 kHz, Scan Speed 100, (b) Focal Length 15 mm, Fluence 0.211 J/cm<sup>2</sup>, Polarization Angle 90, Frequency 1 kHz, Scan Speed 500, (c) Focal Length 15 mm, Fluence 0.337 J/cm<sup>2</sup>, Polarization Angle 90 °, Frequency 1 kHz, Scan Speed 10, (d) Focal Length 15 mm, Fluence (J/cm<sup>2</sup>) 0.337, Polarization Angle 90 °, Frequency 1 kHz, Scan Speed 50, (e) Focal Length 15 mm, Fluence 0.337 J/cm<sup>2</sup>, Polarization Angle 90 °, Frequency 1 kHz, Scan Speed 100, (f) Focal Length 15 mm, Fluence 0.337 J/cm<sup>2</sup>, Polarization Angle 90 °, Frequency 1 kHz, Scan Speed 500

**Table 19** Statistics of cavities without ripples.

	Cavity No.	Scan Speed	Pulses	Power	Frequency	Desired Cavity Diameter	Fluence	Energy	Actual Cavity Diameter	Cycles	Pulses x Pass Over	Focal Length	W0	Polarizer Angle
		[ $\mu\text{m/s}$ ]		[mW]	[kHz]	[ $\mu$ ]	[J/cm <sup>2</sup> ]	[ $\mu\text{J}$ ]	[ $\mu$ ]			[mm]	[mm]	
4 <sup>th</sup> Set	Cavity 69	10	100,000	1	1	12.29	0.843	1	10	1	100000	15	0.8	90°
	Cavity 70	50	20,000	1	1	12.29	0.843	1	7	1	20000	15	0.8	90°
	Cavity 71	100	10,000	1	1	12.29	0.843	1	7	1	10000	15	0.8	90°
	Cavity 72	500	2,000	1	1	12.29	0.843	1	7.5	1	2000	15	0.8	90°
5 <sup>th</sup> Set	Cavity 73	10	100,000	2	1	12.29	1.69	2	10	1	100000	15	0.8	90°
	Cavity 74	50	20,000	2	1	12.29	1.69	2	10	1	20000	15	0.8	90°
	Cavity 75	100	10,000	2	1	12.29	1.69	2	9	1	10000	15	0.8	90°
	Cavity 76	500	2,000	2	1	12.29	1.69	2	10	1	2000	15	0.8	90°
1 <sup>st</sup> Set		[ $\mu\text{m/s}$ ]		[mW]	[kHz]	[ $\mu$ ]	[J/cm <sup>2</sup> ]	[ $\mu\text{J}$ ]	[ $\mu$ ]			[mm]	[mm]	
	Cavity 77	10	100,000	0.25	1	12.29	0.211	0.25	10	5	500000	15	0.8	90°
	Cavity 78	10	100,000	0.25	1	12.29	0.211	0.25	10	25	2500000	15	0.8	90°
	Cavity 79	50	20,000	0.25	1	12.29	0.211	0.25	11	5	100000	15	0.8	90°
	Cavity 80	50	20,000	0.25	1	12.29	0.211	0.25	8	25	500000	15	0.8	90°
2 <sup>nd</sup> Set	Cavity 81	50	20,000	0.25	1	12.29	0.211	0.25	8	50	1000000	15	0.8	90°
	Cavity 82	10	100,000	1	1	12.29	0.843	1	10	5	500000	15	0.8	90°
	Cavity 83	10	100,000	1	1	12.29	0.843	1	11	25	2500000	15	0.8	90°
	Cavity 84	50	20,000	1	1	12.29	0.843	1	11	5	100000	15	0.8	90°
	Cavity 85	50	20,000	1	1	12.29	0.843	1	11	25	500000	15	0.8	90°
3 <sup>rd</sup> Set	Cavity 86	50	20,000	1	1	12.29	0.843	1	10	50	1000000	15	0.8	90°
	Cavity 87	10	100,000	0.5	1	12.29	0.421	0.5	12	5	500000	15	0.8	90°
	Cavity 88	10	100,000	0.5	1	12.29	0.421	0.5	10	20	1000000	15	0.8	90°
	Cavity 89	50	20,000	0.5	1	12.29	0.421	0.5	10	5	100000	15	0.8	90°
	Cavity 90	50	20,000	0.5	1	12.29	0.421	0.5	11	25	500000	15	0.8	90°
	Cavity 91	50	20,000	0.5	1	12.29	0.421	0.5	9	50	1000000	15	0.8	90°

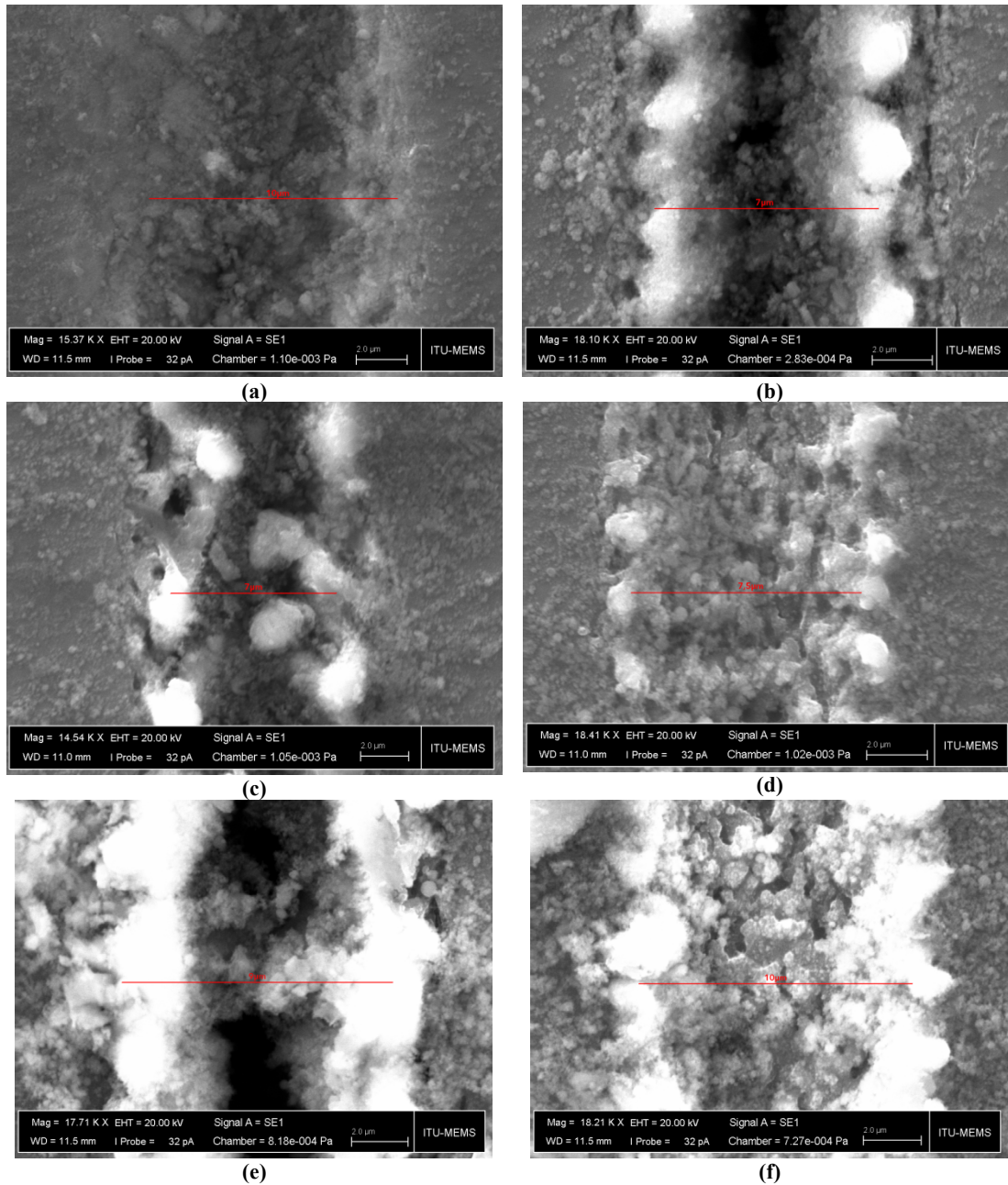


**Figure 4.25** (a) Focal Length 15 mm, Fluence 0.843 J/cm<sup>2</sup>, Polarization Angle 90 °, Frequency 1 kHz, Scan Speed 10, (b) Focal Length 15 mm, Fluence 0.843 J/cm<sup>2</sup>, Polarization Angle 90 °, Frequency 1 kHz, Scan Speed 50, (c) Focal Length 15 mm, Fluence 0.843 J/cm<sup>2</sup>, Polarization Angle 90 °, Frequency 1 kHz, Scan Speed 100, (d) Focal Length 15 mm, Fluence 0.843 J/cm<sup>2</sup>, Polarization Angle 90 °, Frequency 1 kHz, Scan Speed 100, (e) Focal Length 15 mm, Fluence 0.843 J/cm<sup>2</sup>, Polarization Angle 90 °, Frequency 1 kHz, Scan Speed 100, (f) Focal Length 15 mm, Fluence 0.843 J/cm<sup>2</sup>, Polarization Angle 90 °, Frequency 1 kHz, Scan Speed 100

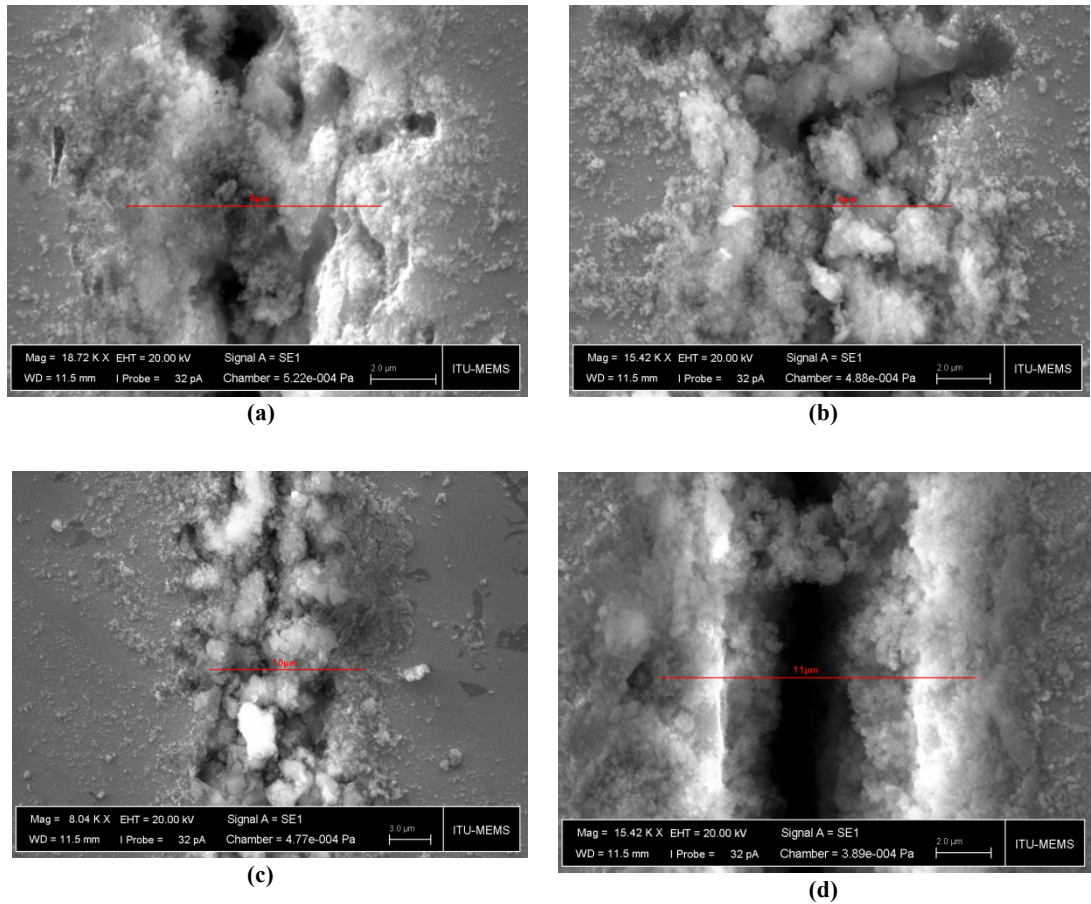


**Figure 4.26** SEM images of cavities drilled for this experiment. **(a)** Focal Length 15 mm, Fluence  $0.211 \text{ J/cm}^2$ , Polarization **(b)** Frequency 1 kHz, Scan Speed 50, **(c)** Focal Length 15 mm, Fluence  $0.211 \text{ J/cm}^2$ , Polarization Angle  $90^\circ$ , Frequency 1 kHz, Scan speed 50, **(d)** Focal Length 15 mm, Fluence  $0.843 \text{ J/cm}^2$ , Polarization Angle  $90^\circ$ , Frequency 1 kHz, Scan Speed 10

As seen in the below SEM images as seen in **Figure 4.27** were taken at  $45^\circ$  angle, it was obvious that multiple cycles and high amounts of pulses per area resulted in much deeper cavities. The chaotic and non-uniform look in the images taken at  $90^\circ$  angle was a result of the two dimensional effect of such deep cavities, looking as if all the layers of the deep cavities was at the same axis.

During this experiment it was observed that multiple cycles and slow scan speed results in deeper and wider cavities. But an exact measurement could not be achieved by the profileometer since the cavities were thinner in width than the needle of the profileometer, which is used to measure the depth. To get more precise depth measurements new cavities were to be micromachined at the edge of the wafers for evaluation.

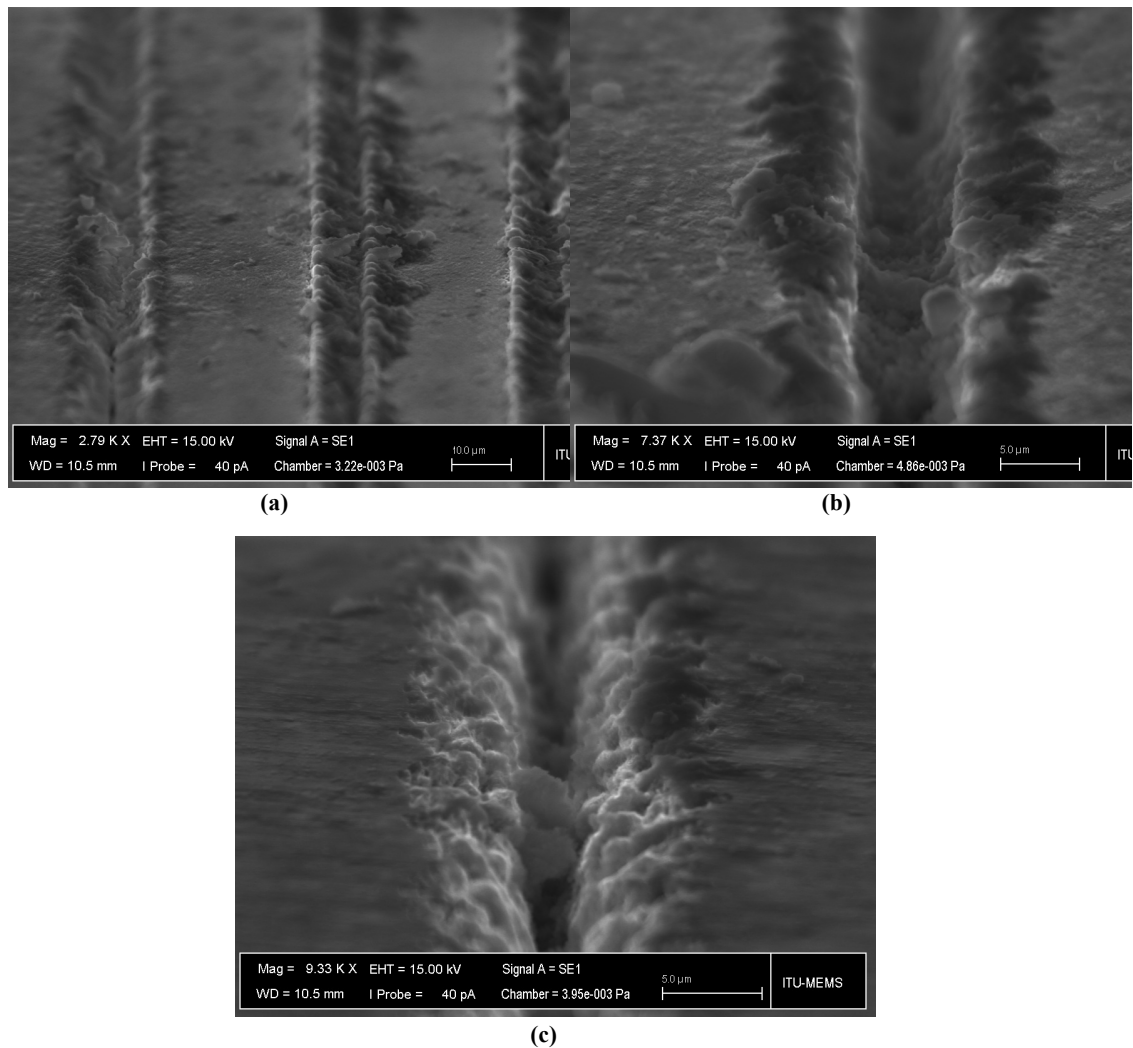


**Figure 4.27** SEM images of some of the cavities from **Figure 4.25** at a 45° angle. The 2<sup>nd</sup> and 3<sup>rd</sup> images are of the deeper cavities. **(a)** Focal Length 15mm, Fluence 0.16 J/cm<sup>2</sup>, Polarization Angle 90°, Frequency 1 kHz, Scan Speed 10, 50 and 100 respectively, **(b)** Focal Length 15mm, Fluence 0.421 J/cm<sup>2</sup>, Polarization Angle 90°, Frequency 1 kHz, Scan Speed 50 μm/s, **(c)** Focal Length 15mm, Fluence 0.843 J/cm<sup>2</sup>, Polarization Angle 90°, Frequency 1 kHz, Scan Speed 50 μm/s

Thus the decision was made to create cavities wide enough for measurement. For this goal increasing the energy, cycle and number of pulses while reducing the scan speed wouldn't be enough. It would require lenses with higher focal lengths to achieve these wider cavities, in other words expand the achievable beam radius or  $W_0$ .

According to the achievable beam waist formula (4.3) when using a focal length of  $f=100$  mm lens the achievable beam waist would be  $W_f = 81.96$  .

At first experiments were to be run using high scan speed with the  $f=100$  mm focal length lens only to examine the effects on the substrate when using such a high focal length lens.

It was known that a high speed of  $V=1$  m/s wouldn't create enough ablation to machine deep enough, but whether the ablation threshold at fluence levels would remain the same when the lens was changed in huge units, or a high focal length lens would ablate at all with all the photon scattering in a wider area was unknown. For this reason fluence of  $0.16 \text{ J/cm}^2$  (melting threshold from previous experiments) and  $0.4 \text{ J/cm}^2$  (approximate ablation threshold from previous experiments) would be used and later higher fluence levels would be tested, to observe the cavity width behavior compared to increase in fluence.

#### **4.14 Wider Cavity Micromachining**

The aim of this experiment was to achieve wider cavities while finding the effects of energy – fluence on wider cavity micromachining when using a lens with a much wider focal length. For this experiment the laser pulse duration was set to 500 fs at a repetition rate of 1 kHz, with varying energy and power levels at fixed scan speed and fixed amount of pulses. As seen in **Table 20**, the polarization angle was set to  $90^\circ$ , and the new lens with a focal length of 100 mm was used.

Referring to the images in **Figure 4.28**, achievable cavity width could not be estimated since the images were variant in huge intervals such as picture (b) and picture (e). This might have been a consequence of using lenses with wide focal lengths since they scatter the laser beam, making it lose its intensity and effectiveness, or it could be a result of using a very fast scan speed making the distribution of pulses non-uniform.

Resulting in unclear results as to the acquirable desired cavity width. Only clearly visible aspect of these cavities were the effects of ripples. According to this data, deeper and wider cavities would be drilled at higher energy ratings with very low scan speeds and lenses with shorter focal lengths. So  $f=50$  mm focal length lens was to be used for the first time.

**Table 20** Parameters and resulting beam diameters for this experiment

Cavity No.	Scan Speed	Pulses	Power	Frequency	Desired Cavity Diameter	Fluence	Energy	Actual Cavity Diameter	Passovers	Pulses x Pass Over	Focal Length	W0	Polarizer Angle
	[ $\mu\text{m/s}$ ]		[mW]	[kHz]	[ $\mu$ ]	[J/cm <sup>2</sup> ]	[ $\mu\text{J}$ ]	[ $\mu$ ]			mm	mm	
Cavity 92	1000	20000	220	1	81.96	4.17	220	118	1	20000	100	0.8	90°
Cavity 93	1000	20000	150	1	81.96	2.84	150	185	1	20000	100	0.8	90°
Cavity 94	1000	20000	100	1	81.96	1.9	100	188	1	20000	100	0.8	90°
Cavity 95	1000	20000	80	1	81.96	1.52	80	208	1	20000	100	0.8	90°
Cavity 96	1000	20000	50	1	81.96	0.948	50	229	1	20000	100	0.8	90°
Cavity 97	1000	20000	50	1	81.96	0.948	50	215	1	20000	100	0.8	90°
Cavity 98	1000	20000	50	1	81.96	0.948	50	231	1	20000	100	0.8	90°

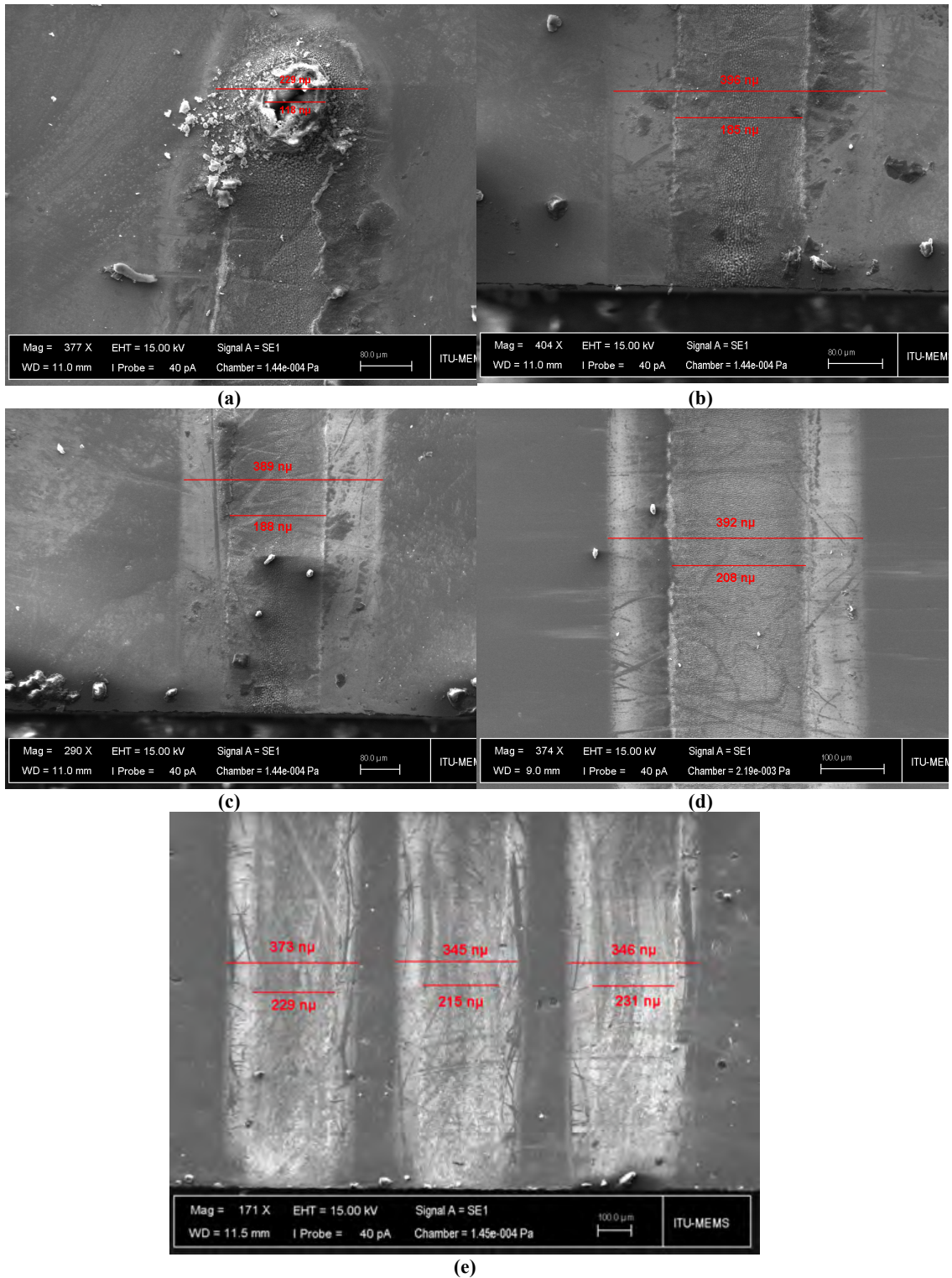


**Figure 4.28** SEM images for cavities created using a 100 mm Focal Length lens. **(a)** Focal Length 100 mm, Fluence  $4.17 \text{ J/cm}^2$ , Polarization Angle  $90^\circ$ , Frequency 1 kHz, Scan Speed 1000, **(b)** Focal Length 100 mm, Fluence  $4.17 \text{ J/cm}^2$ , Polarization Angle  $90^\circ$ , Frequency 1 kHz, Scan Speed 1000, **(c)** Focal Length 100 mm, Fluence  $1.9 \text{ J/cm}^2$ , Polarization Angle  $90^\circ$ , Frequency 1 kHz, Scan Speed 1000, **(d)** Focal Length 100 mm, Fluence  $1.52 \text{ J/cm}^2$ , Polarization Angle  $90^\circ$ , Frequency 1 kHz, Scan Speed 1000, **(e)** Focal Length 100 mm, Fluence  $0.948 \text{ J/cm}^2$ , Polarization Angle  $90^\circ$ , Frequency 1 kHz, Scan Speed 1000

#### 4.15 Effects Of Energy And Fluence On Wider Cavity Micromachining With 50mm Focal Length Lens

To achieve wider and deeper cavities and to figure the effects of energy and fluence on depth and width of cavities, tests were run at 500 fs, with a repetition rate of 1 kHz, using varying amounts of pulses as a consequence of the different scan speed and multi-passovers. Polarization angle was set to 90°, using a 50 mm focal length lens.

The scan speed was kept at very low values to benefit from the maximum pulse per area amounts to achieve deeper cavities. The cavities were ablated on the edge of the wafer to measure the exact depth. The data of the resulting cavities can be seen below in **Table 21**.

Since the pulse amount is directly proportional to the Passover parameter, and inversely proportional to scan speed, the combination of the two variables is used in the graphs to see the effects altogether.

The combination of the effects of Passover and scan speed together is named “Pulse Amount Coefficient”. It is found by dividing the absolute value of the Passover by the absolute value of the scan speed

$$\text{Pulse Amount Coefficient} = \frac{\text{Passover}}{\text{Scan Speed}} \quad (4.3)$$

Referring to **Figure 4.30**, Cavity depth vs. pulse amount coefficient graphs shows linear characteristics rather than the cavity width vs. pulse amount coefficient graph.

Results of the experiment were inspected and compared such as the cavity sets in **Figure 4.30**.

Considering the results of cavity widths and depths in this experiment, methods to excavate even wider cavities, since these cavities would have to allow the focusing of micro-particles. The cavities could in turn be transformed into a micro-fluidic-particle focusing mechanism.

**Table 21** Effects of scan speed and fluence on cavity depth and width, using a 50mm lens.

Cavity No.	Cycles	Scan Speed [ $\mu\text{m/s}$ ]	Power [mW]	Frequency [kHz]	Desired Cavity			Energy [ $\mu\text{J}$ ]	Passovers	Polarizer Angle	Focal Length [mm]	W0 [mm]	Cavity Width [ $\mu\text{m}$ ]	Cavity Depth [ $\mu\text{m}$ ]
					Diameter [ $\mu$ ]	Fluence [J/cm <sup>2</sup> ]								
Cavity 99	3	5	220	1	40.98	16.7	220	6	90°	50	0.8	40.0	308.6	
Cavity100	3	5	220	1	40.98	16.7	220	6	90°	50	0.8	40.0	321.4	
Cavity101	5	10	220	1	40.98	16.7	220	10	90°	50	0.8	37.1	308.6	
Cavity102	4	10	220	1	40.98	16.7	220	8	90°	50	0.8	41.1	295.9	
Cavity103	2	10	220	1	40.98	16.7	220	4	90°	50	0.8	34.4	224.8	
Cavity104	1	5	220	1	40.98	16.7	220	2	90°	50	0.8	46.0	258.0	
Cavity105	2	5	220	1	40.98	16.7	220	4	90°	50	0.8	32.9	309.0	

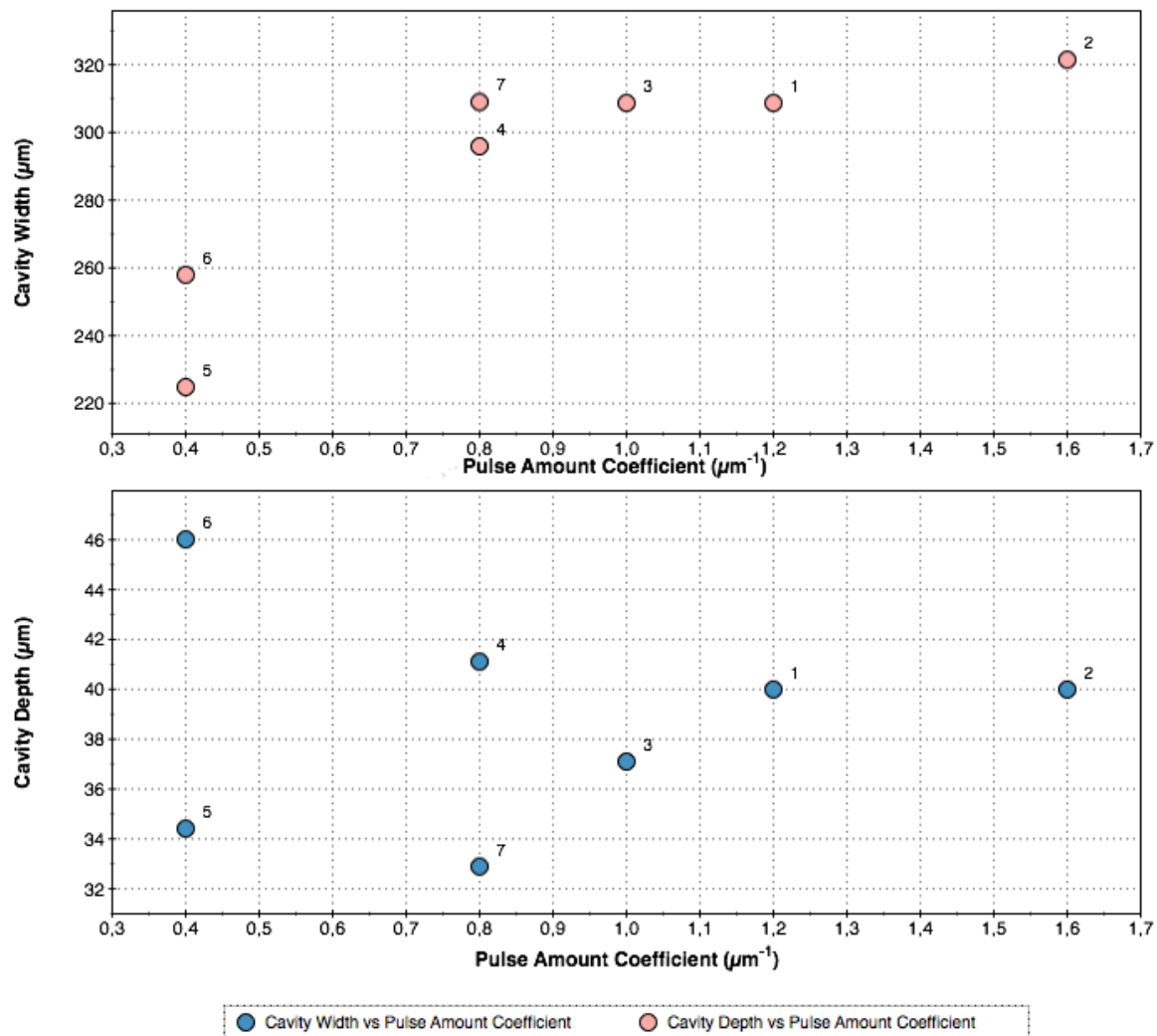


**Figure 4.29** Graph comparing the cavity width at differing Pulse Amount Coefficients, which equals Passovers/Scan Speed . Focal Length: 50 mm.

Referring to the SEM images and the collected data, the depth of the cavities were adequate enough for the microfluidics which would separate microparticle in future experiments. Thus more experiments using lenses with longer focal lengths had to be done again, but this time with slower scan speeds allowing the pulse per area amount to increase.

#### 4.16 Effects Of Energy And Fluence On Wider Cavity Micromachining with 100mm lens

In this experiment, laser pulse duration was set to 500fs, with a repetition rate of 1 kHz, using the same amount of pulses (because of the fixed scan speed) but with multiple Passovers. Polarization angle was set to  $90^\circ$ , a lens with a focal length of

100 mm was used to obtain wider cavities. To avoid the scatter effect of using lenses with wider focal lengths, the scan speed is at the slowest rate to increase the pulse per area amount as seen in **Table 22**.

It was observed during this experiment that using a higher focal length of 100 mm has caused a scatter effect. Referring to the graph in **Figure 4.31** although the pulse amount coefficient was much higher than the previous experiment. The depths were close to the cavities ablated with  $f = 50$  mm lens. The cavity widths were also just a little wider, which resulted in cavity widths ending up close to those that were ablated with  $f=50$  mm lens. This is because the laser is more powerful as the focus area is reduced. When the area gets larger the effects of the laser is scattered over that larger area resulting in reduced power.

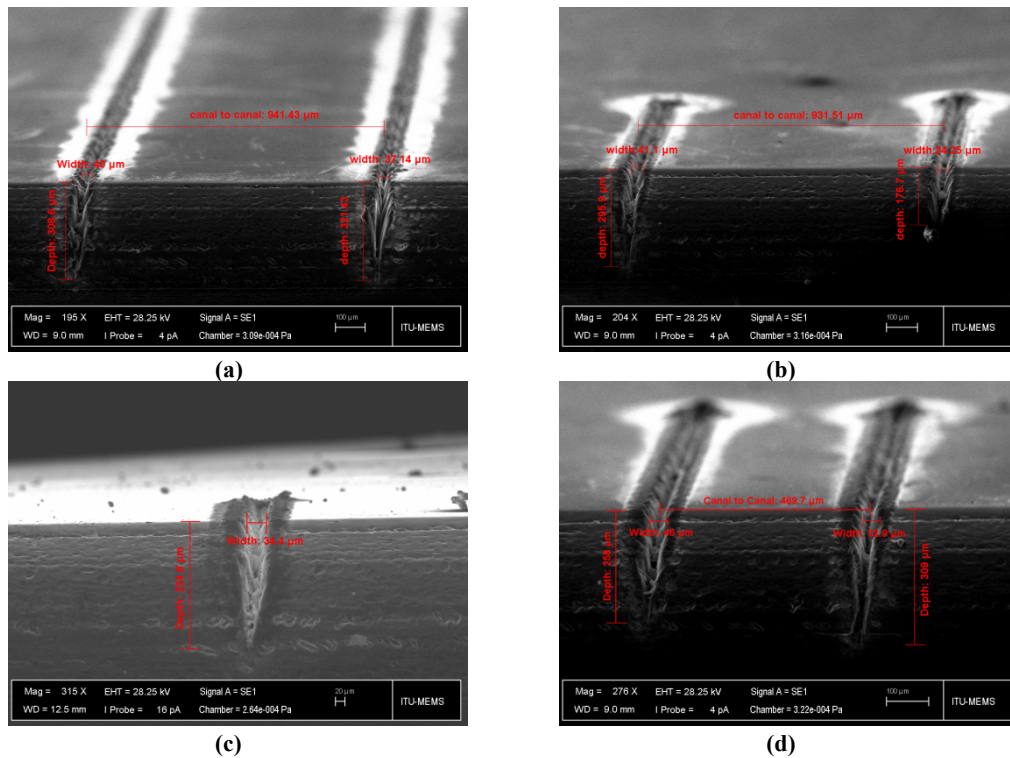


**Figure 4.30** Cross-Sectional SEM images showing changes in cavity width and depth at focal length 50 mm. **(a)** Focal Length 50 mm, Fluence 16.7 J/cm<sup>2</sup>, Polarization Angle 90°, Frequency 1 kHz, Scan Speed 5, **(b)** Focal Length 50 mm, Fluence 16.7 J/cm<sup>2</sup>, Polarization Angle 90°, Frequency 1 kHz, Scan Speed 10, **(c)** Focal Length 50 mm, Fluence 16.7 J/cm<sup>2</sup>, Polarization Angle 90°, Frequency 1 kHz, Scan Speed 10, **(d)** Focal Length 50 mm, Fluence 16.7 J/cm<sup>2</sup>, Polarization Angle 90°, Frequency 1 kHz, Scan Speed 5

**Table 22**  $f=100\text{mm}$  focal length lens is used to try and achieve wider cavity widths and depths

Cavity No.	Cycles	Scan			Desired Cavity			Actual Cavity		Polarizer Angle	Focal Length [mm]	W0 [mm]	Cavity Width [ $\mu\text{m}$ ]	Cavity Depth [ $\mu\text{m}$ ]
		Speed [ $\mu\text{m/s}$ ]	Power [mW]	Frequency [kHz]	Diameter [ $\mu$ ]	Fluence [ $\text{J/cm}^2$ ]	Energy [ $\mu\text{J}$ ]	Diameter [ $\mu$ ]	Passovers					
Cavity 106	2	5	225	1	81.96	4.26	225	68.6	12	90°	100	0.8	68.5	327.4
Cavity 107	3	5	225	1	81.96	4.26	225	82.3	18	90°	100	0.8	82.3	323.2
Cavity 108	2	5	225	1	81.96	4.26	225	68.8	12	90°	100	0.8	68.8	329.9
Cavity 109	0.5	5	225	1	81.96	4.26	225	44.8	3	90°	100	0.8	44.8	184.1

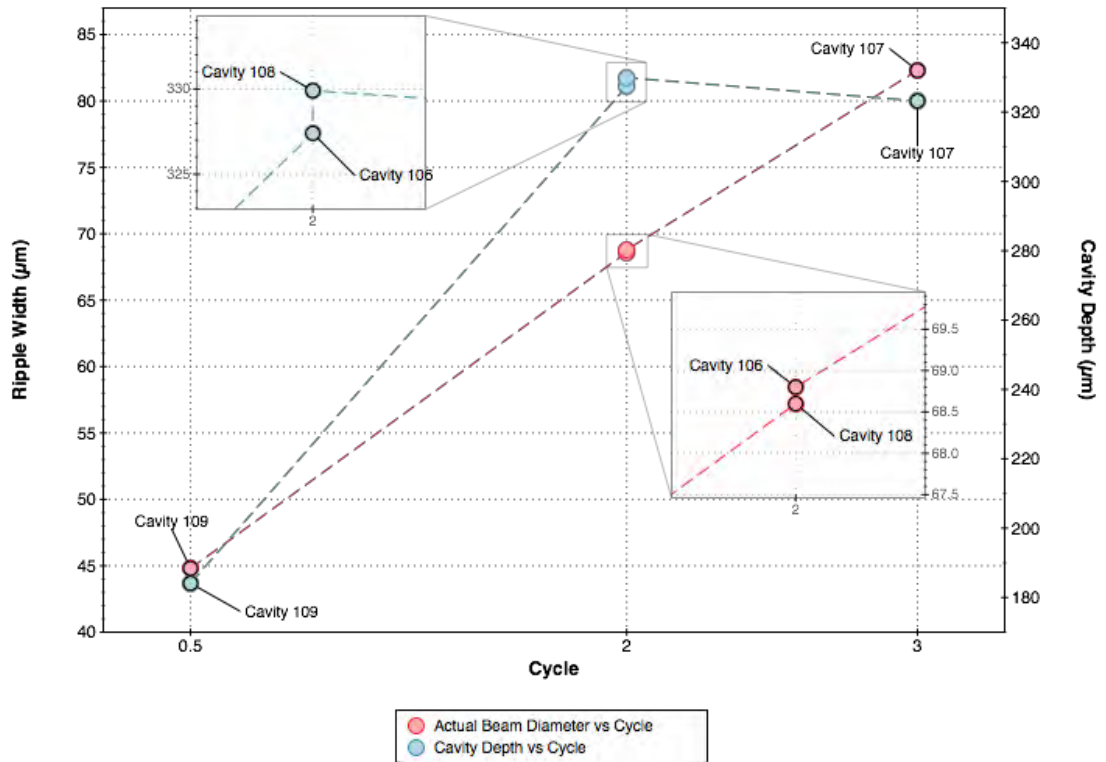
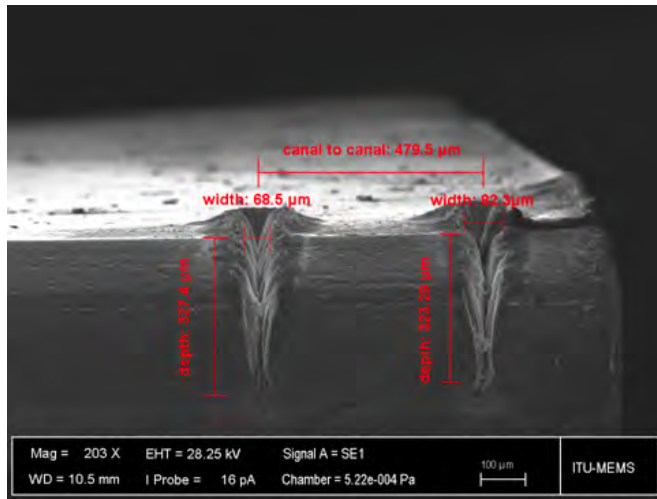


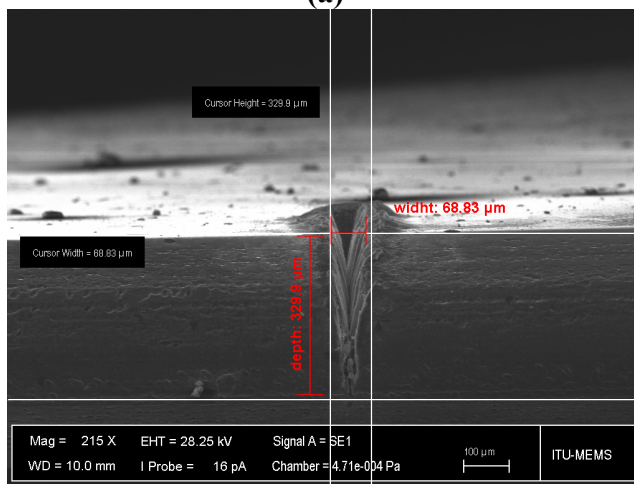
**Figure 4.31** Comparison of cavity depth and Actual Cavity Diameter to cycles. Focal Length: 100 mm.

#### 4.17 Further Experimentation With 100mm Lens

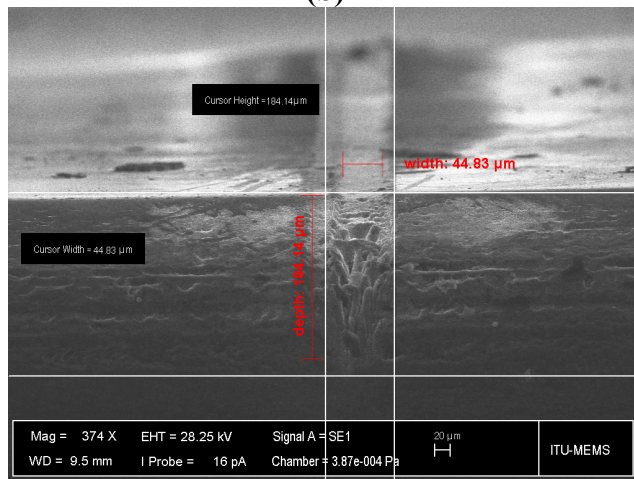
Further tests were run with 100 mm focal length lens to study it's effects on cavity width. Again laser pulse duration was set to 500 fs, with a repetition rate of 1 kHz, with the same amount of pulses (because of fixed scan speed), versus different energy, fluence rates as listed in **Table 23**.



(a)



(b)



(c)

**Figure 4.32** SEM cross-sectional images of cavities drilled with 100 mm focal length lens. **(a)** Focal Length 100 mm, Fluence  $4.26 \text{ J/cm}^2$ , Pol.n Angle  $90^\circ$ , Frequency 1 kHz, Scan Speed 5, **(b)** Focal Length 100 mm, Fluence  $4.26 \text{ J/cm}^2$ , Pol. Angle  $90^\circ$ , Frequency 1 kHz, Scan Speed 5 **(c)** Focal Length 100 mm, Fluence  $4.26 \text{ J/cm}^2$ , Pol.Angle  $90^\circ$ , Frequency 1 kHz, Scan Speed 5

**Table 23** 100mm Focal Length Lens cavity width tests.

Cavity No.	Cycles	Scan Speed [ $\mu\text{m/s}$ ]	Power [mW]	Frequency [kHz]	Desired Cavity Diameter [ $\mu$ ]	Fluence [J/cm <sup>2</sup> ]	Energy [ $\mu\text{J}$ ]	Time to travel desired radius [ms]	Passovers	Polarizer Angle	Focal Length f	Cavity Width [ $\mu\text{m}$ ]	Cavity Overlap [ $\mu\text{m}$ ]
Cavity 110	1	1	150	1	81.96	2.84	150	32800		90°	100	246.1	N/A
Cavity 111	1	1	150	1	81.96	2.84	150	32800		90°	100	298.0	?
Cavity 112	1	1	150	1	81.96	2.84	150	32800		90°	100	248.7	N/A
Cavity 113	1	1	100	1	81.96	1.90	100	32800		90°	100	259.0	N/A
Cavity 114	1	1	100	1	81.96	1.90	100	32800		90°	100	251.3	N/A
Cavity 115	1	1	100	1	81.96	1.90	100	32800		90°	100	266.8	N/A
Cavity 116	1	1	220	1	81.96	4.17	220	32800		90°	100	100.7	N/A
Cavity 117	1	1	220	1	81.96	4.17	220	32800		90°	100	151.6	23.0
Cavity 118	1	1	220	1	81.96	1.47	220	32800		90°	100	78.8	51.3

Referring to the SEM images in **Figure 4.34** the changes in width according to the fluence can be observed again.

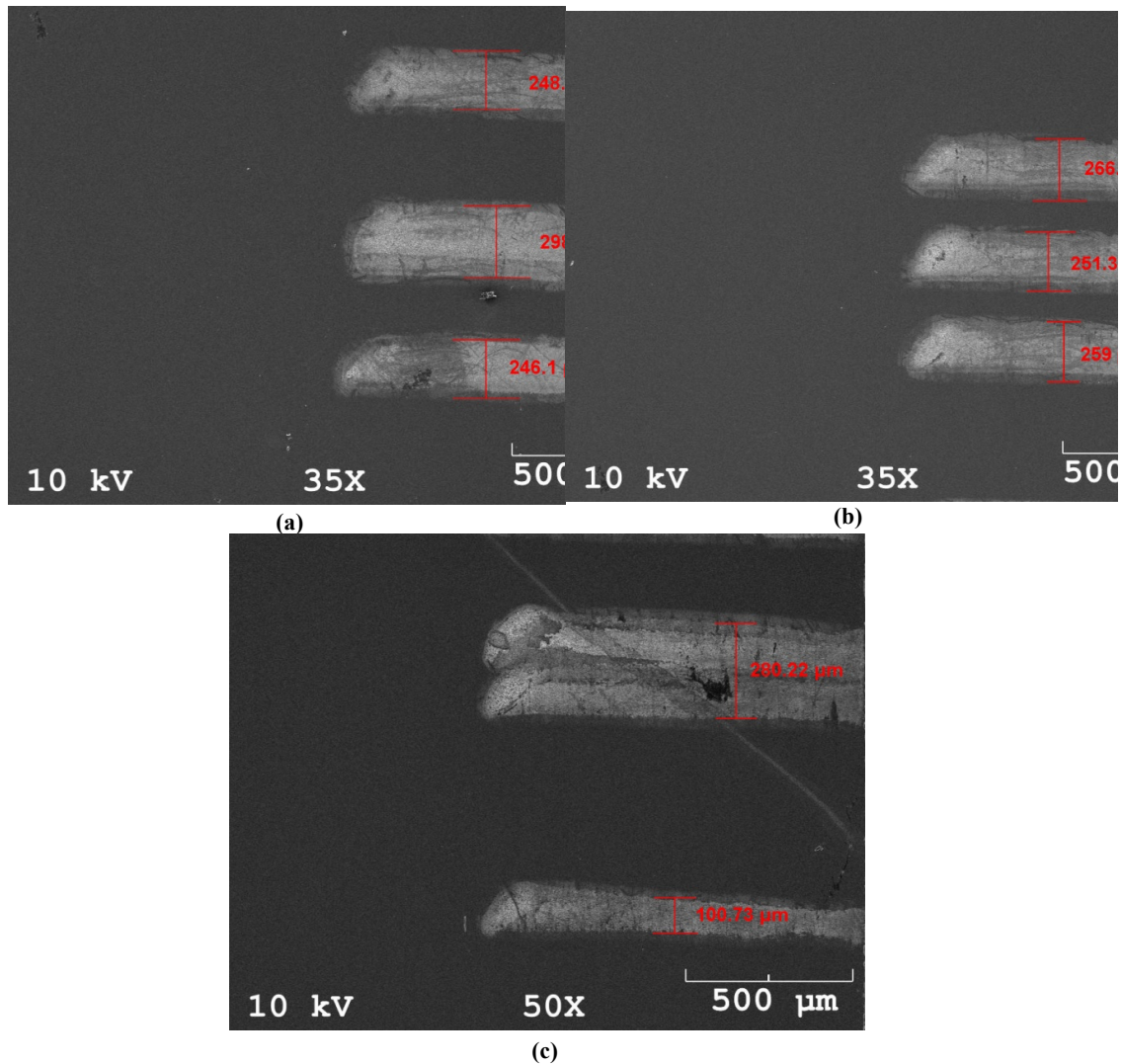


**Figure 4.33** Parameter details per cavity for 100 mm Focal Length Tests. **(a)** Focal Length 100 mm, Fluence  $2.84 \text{ J/cm}^2$ , Polarization Angle  $90^\circ$ , Frequency 1 kHz, Scan Speed 1, **(b)** Focal Length 100 mm, Fluence  $1.9 \text{ J/cm}^2$ , Polarization Angle  $90^\circ$ , Frequency 1 kHz, Scan Speed 1, **(c)** Focal Length 100 mm, Fluence  $4.17 \text{ J/cm}^2$ , Polarization Angle  $90^\circ$ , Frequency 1 kHz, Scan Speed 1

#### 4.18 Dumbbell Like Structures

After experimenting on various different parameter setups, it was decided to proceed to dumbbell shaped structure shown in **Figure 4.35** to present an example for microfluidic applications.

The aim of this dumbbell like microfluidic cavity formation is line up the micro particles that enter from one side, and pass them through the other side in order.

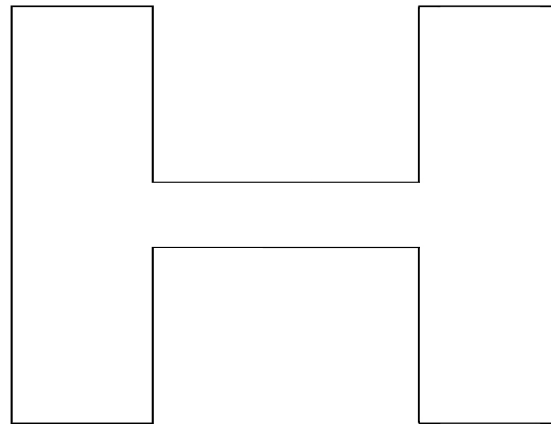
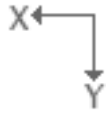


**Figure 4.34** Shape of the desired dumbbell like formation

To understand the effects of fixed polarization while the wafer is irradiated in both x and y directions high speed (1 mm/s) experiments were actualized.

#### **4.19 Ablation In Both X And Y Directions With Fixed Polarization Angle And Creating Dumbbell Shaped Channels**

The aim of this experiment was to understand the differences between four different energy-fluence levels of laser ablation in both x and y scanning directions and test whether there is enough room for PDMS to fill in between the 2 cavities when they're set to 100  $\mu\text{m}$  wide in theory.

These dumbbell like structures, are designed to, if wide, deep and smooth enough, be able to separate the micro particles using the laws of fluid mechanics.

The actual measurements and the SEM images of the dumbbell like structures ablated with a power of 60 mW, 100 mW, 170 mW, 200 mW respectively are represented in **Figure 4.35**, **Figure 4.36**, **Figure 4.37** and **Figure 4.38** displayed below:

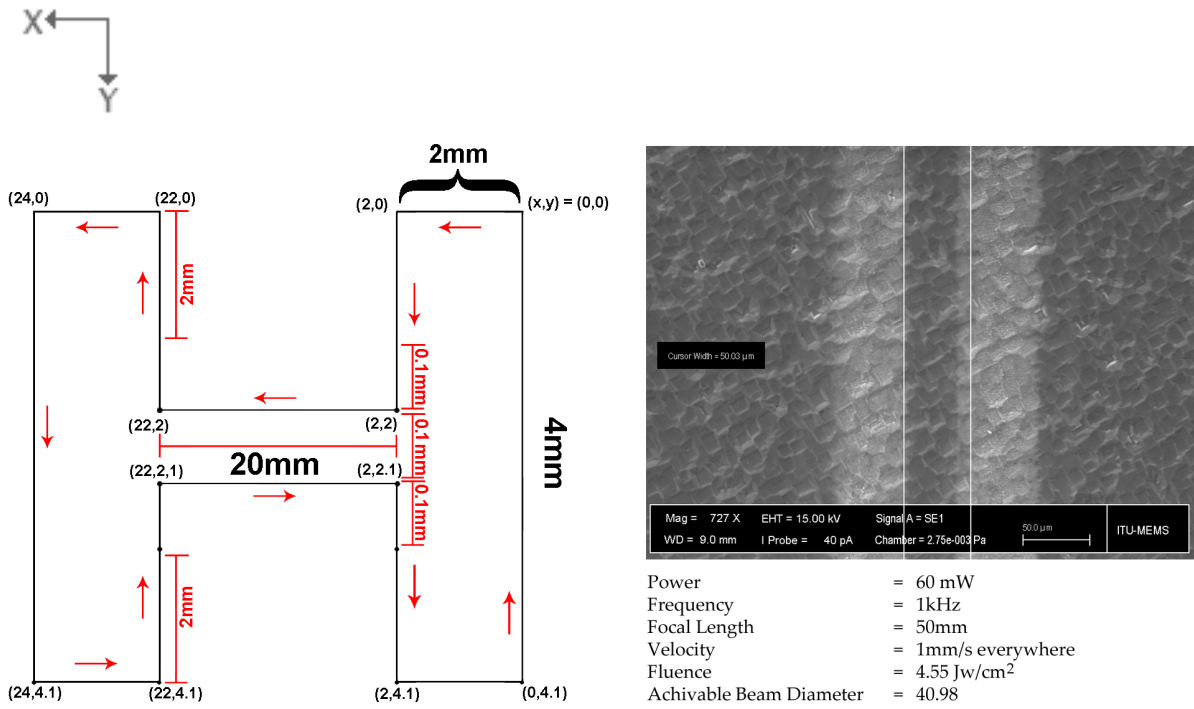


Figure 4.35 Dumbbell shape statistics and resulting SEM image for 60 mW.

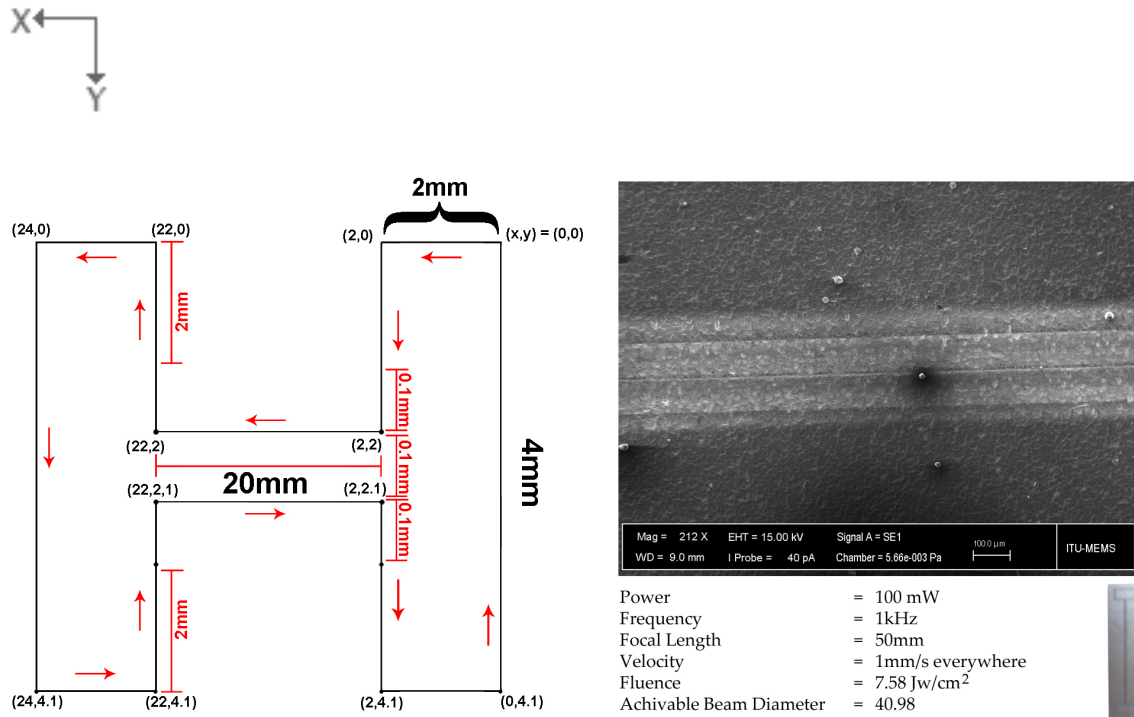
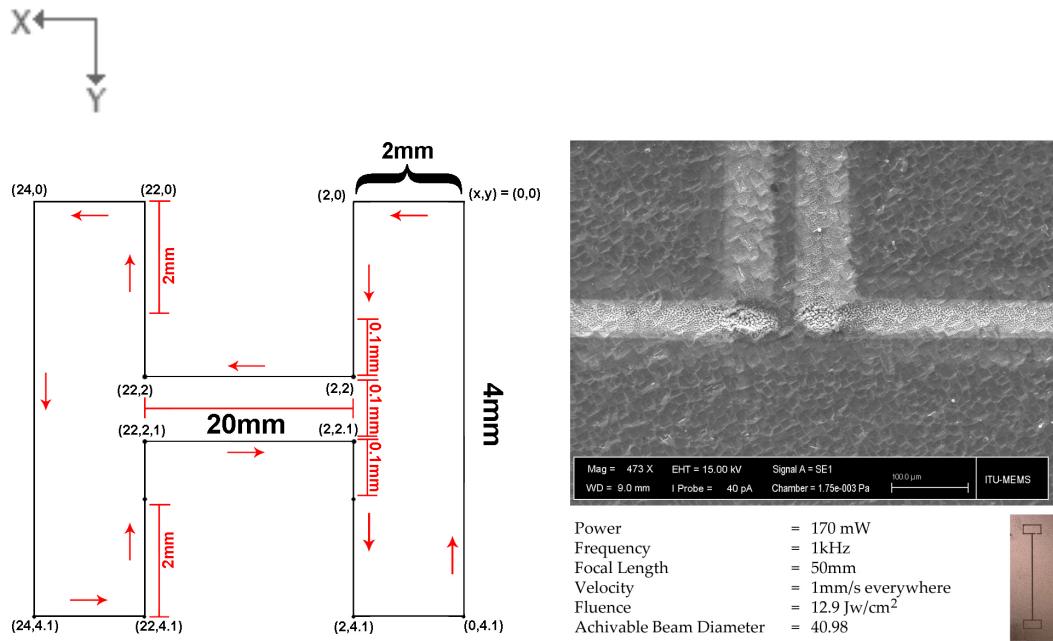
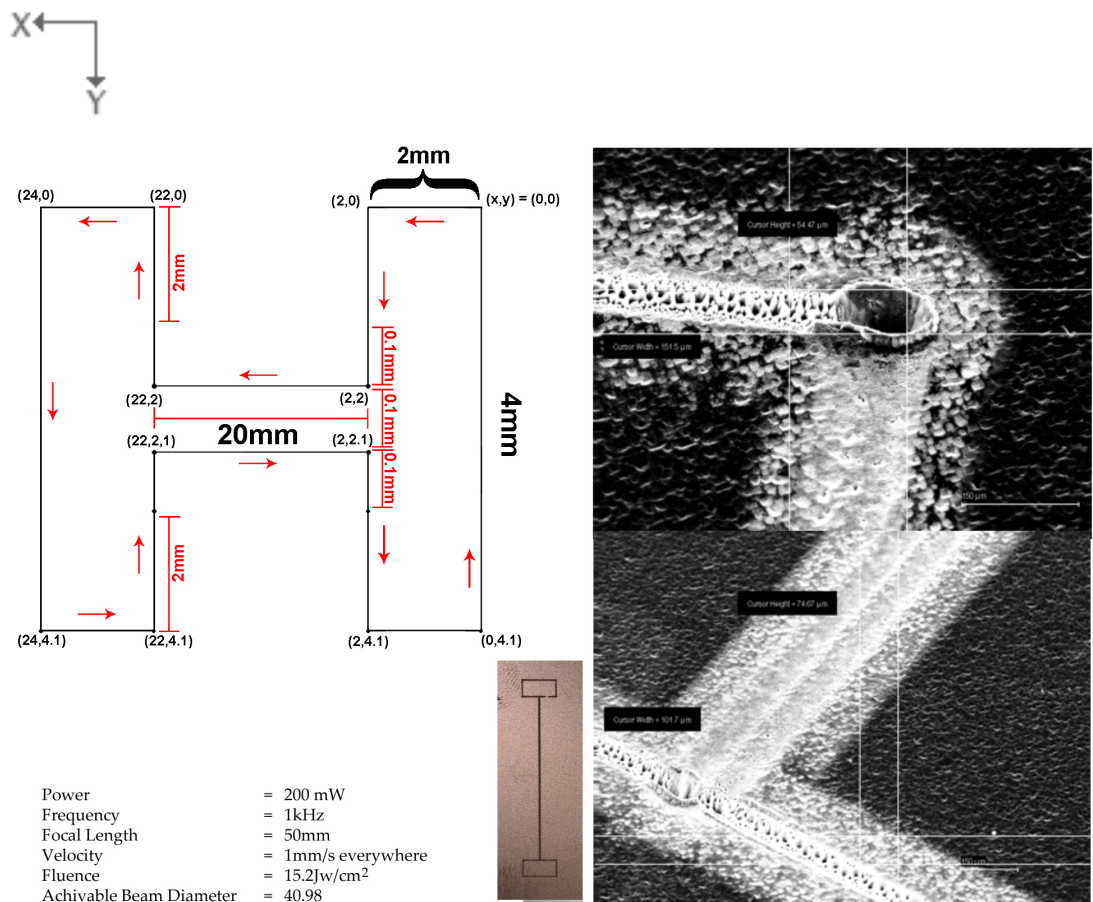


Figure 4.36 Dumbbell shape statistics and resulting SEM image for 100 mW.



**Figure 4.37** Dumbbell shape statistics and resulting SEM image for 170 mW.



**Figure 4.38** Dumbbell shape statistics and resulting SEM images for 200 mW.

As seen in the resulting images in **Figure 4.35**, **Figure 4.36**, **Figure 4.37** and **Figure 4.38**, although the high levels of energy is used, the cavities are not deep at all, since a very high rate of scan speed was chosen making the pulse per area amount very low. But this result was predictable.

The odd thing in the images was that although the polarization angle, scan speed, fluence stayed the same throughout, when creating the dumbbell, the cavities ablated in the X and Y directions show much difference from each other. This could have been a sign to create the perfect cavities. Maybe calibrating the polarization angle according to the scanning direction would eliminate all the unpredictable and unwanted formations on the surfaces.

Further tests have shown visible differences between the ablated areas when the stage was moving in the X axis, and the ablated areas were moving in the Y axis. This difference would be tested with further experimentation.

Since cavity depth and width were not satisfactory, overlapping parallel cavities have been micromachined to form a much wider cavity when combined. The way this system works is, every linear cavity irradiation overlaps the previous one to form a uniform wide cavity.

#### **4.20 Polarization Vs. Scanning Direction X- Y- XY**

The aim of this experiment was to create rectangular cavities 500  $\mu\text{m}$ 's long and 1000  $\mu\text{m}$ 's wide in the directions X, Y and X & Y together to see the effect of polarization angle in different scanning directions. To achieve this goal, cavities are overlapped a radius or less away from the previous cavity. Further to this aim surface characteristics were to be observed when ablating in three directions. 2 passover (1 cycle) was run in the x directions and 2 in the y directions and 1 in both. Polarizer angle was fixed at  $90^\circ$ , with a power of 228 mw at a scan speed of 0.05mm/s with a fluence of  $1.3.1\text{J}/\text{cm}^2$  through an  $f=50\text{mm}$  focal length lens.

The morphology of the creation of the wider cavities which are ablated in the directions, X, Y and XY by the overlapping method can be seen in **Figure 4.39**.

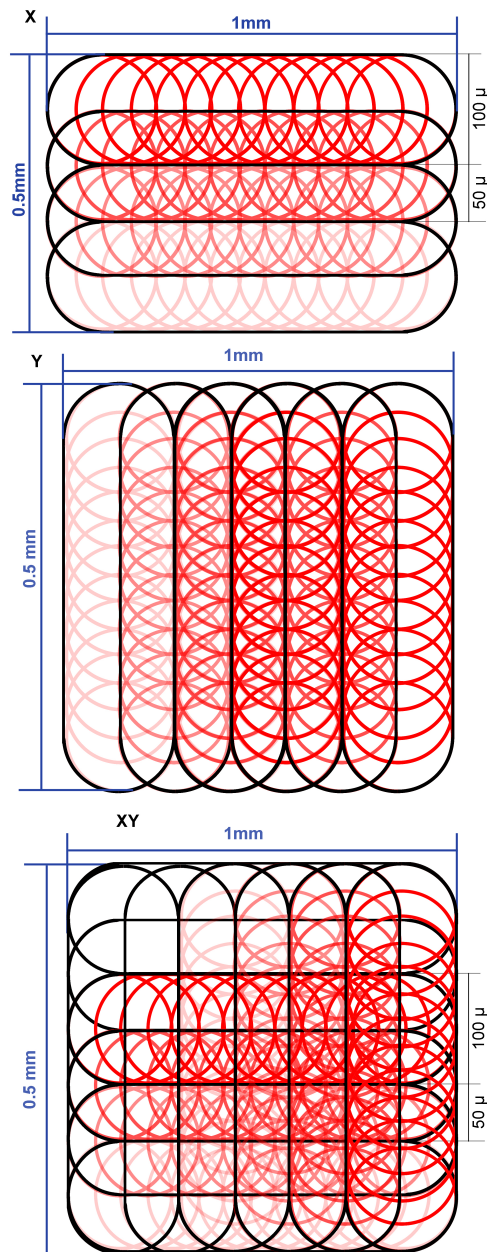
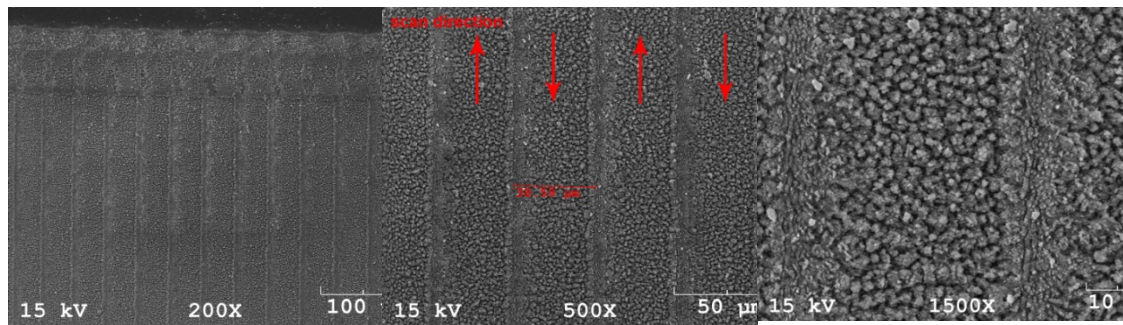
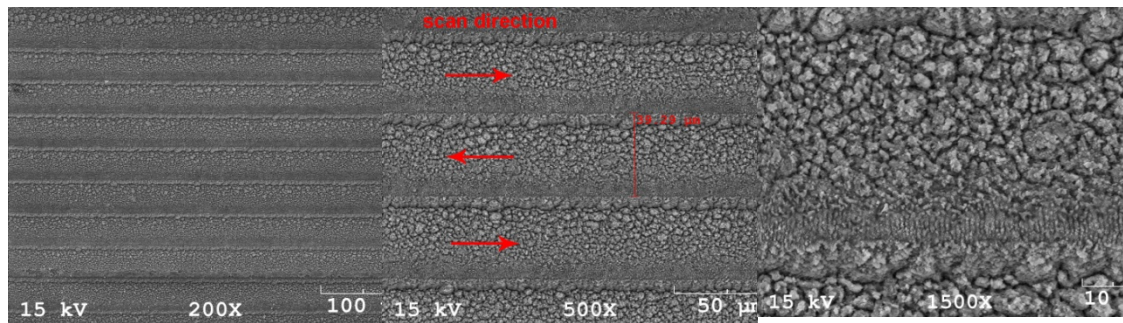


**Figure 4.39** Methodology for creating overlapping cavities.

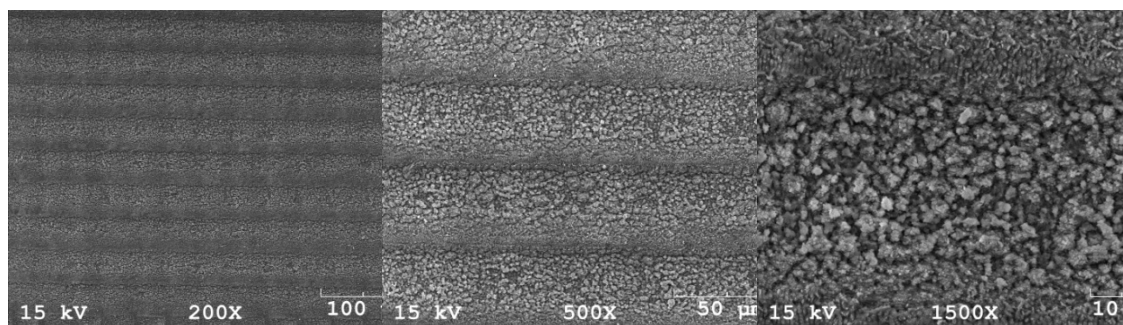
Referring to the picture sets in **Figure 4.40**, it was noted that cavities in the x direction are uneven and incoherent, while cavities in the y direction were smooth and symmetrical. Cavities machined in x then y directions are smoother than cavities machined only in the x direction, but still smoother than the cavities ablated in only the Y direction. This shows that scanning direction is an important parameter when dealing with micro structures. Thus it is better to irradiate in the direction of the polarization angle. The reasoning behind this is, if the laser is moving in the direction of the polarization angle, then they are in the perpendicular direction. The first stage of ripples are formed, making it uniform. Otherwise, if the polarization angle and the scanning direction is perpendicular, the first stage of ripples would form in the scanning direction as the ripples form perpendicular to the polarization angle.



(a)



(b)



(c)

**Figure 4.40** (a) Stage Direction y, Polarization: 90, Power: 228 mW, Fluence: 27.1 J/cm<sup>2</sup>, F: 50mm, V: 0.05 mm/s, (b) Stage Direction , Polarization: 90, Power: 228 mW, Fluence: 27.1 J/cm<sup>2</sup>, F: 50mm, V: 0.05 mm/s, (c) Stage Direction xy, Polarization: 90, Power: 228 mW, Fluence: 27.1 J/cm<sup>2</sup>, F: 50mm, V: 0.05 mm/s

In other words if the cavity is machined in the direction of the ripple formation the waves collide and accumulate disrupting surface symmetry. If the direction of machining is perpendicular to the ripple formation direction, the waves are cut in half, resulting in stronger deformations and uniformity.

In short to achieve smoother and less deformed and more effective laser ablation, polarization angle scanning direction should be parallel to the scanning direction. To

test if the polarization angle being parallel to the scanning direction was good enough. Further experiments on scanning directions were to be run.

#### 4.21 Surface Characteristics In Both X And y Directions (Letter M)

The aim of this experiment is to determine the surface characteristics when scanning in different directions.

Polarizer angle was fixed at  $90^\circ$ , with a power of 230 mW at a scan speed of 0.05 mm/s with a fluence of  $17.4 \text{ J/cm}^2$  through an  $f=50\text{mm}$  focal length lens.

At first the scanning direction goes in the radial coordinate of  $90^\circ$  direction for an absolute distance of 1 mm in the Y axis, the same as the polarization angle. Then the direction turns to the radial coordinate of  $225^\circ$  and moves in that direction until an absolute distance of 0.5 mm in the X axis and 0.5 mm in the Y axis is covered. After the second step is complete, the scanning direction goes in the radial coordinate of  $135^\circ$  until covering an absolute distance of 0.5 mm in the X axis and 0.5 mm in the Y axis. At last the scanning direction goes in the radial coordinate of  $270^\circ$  until an absolute distance of 1 mm is covered in the Y axis. These steps create the M shape in the below schematics.

The measurements and the morphology directions of the creation of the letter M is shown in **Figure 4.41**. The parameters used to machine the letter M are listed below in **Table 24**.

**Table 24** Parameters used to machine the above imaged surfaces.

Cavity No.	Actual Cavity Diameter	Desired Cavity Diameter	Polarizer Angle	Scanning Direction f
Cavity 119	40.49	40.8	$90^\circ$	$90^\circ$
Cavity 120	29.49	40.8	$90^\circ$	$225^\circ$
Cavity 121	39.9	40.8	$90^\circ$	$135^\circ$
Cavity 122	31.9	40.8	$90^\circ$	$270^\circ$

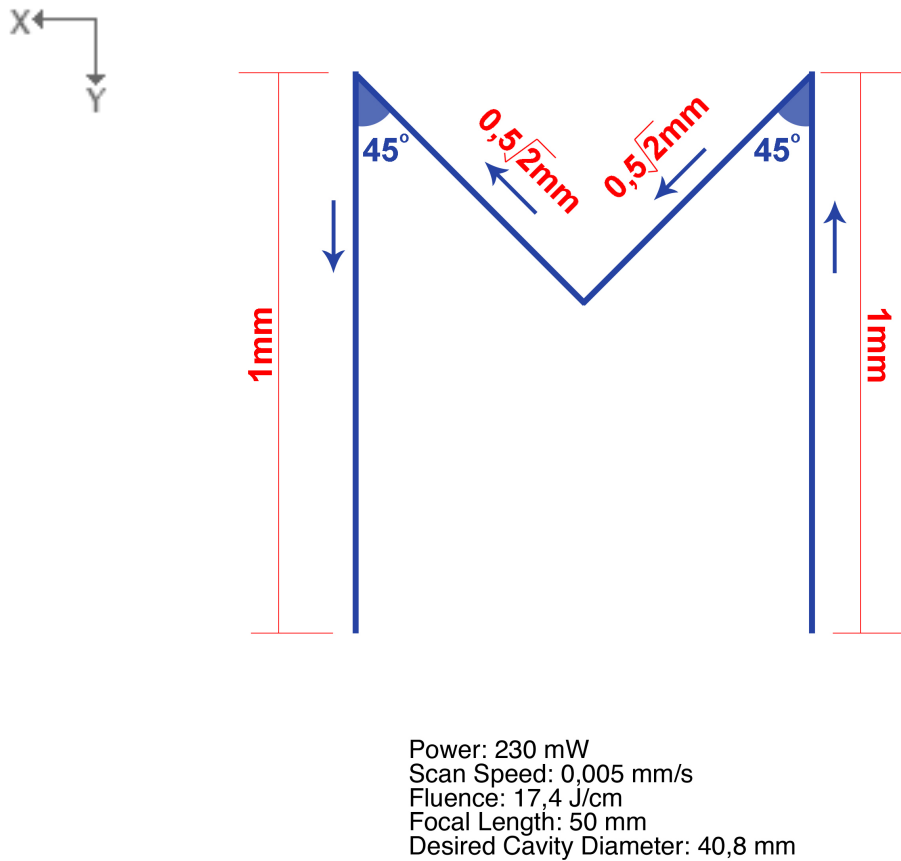


**Figure 4.41** Experiment guidance schematics.

As seen in the table and graphics above in **Figure 4.42**, it is obvious that the closer the radial scanning direction gets to the polarization angle, the closer Actual Cavity Diameter gets to the Desired Cavity Diameter. Referring to the results and images in **Figure 4.43** below consequently keeping the polarization angle and the radial coordinate of the scanning direction equal to each other would give the most estimated results, avoiding the concerns that might occur when an unpredictable data is found by eliminating the unpredictable.

The results of this experiment has shown that polarization angle changes cavity width and surface characterization, but even moving in y or -y effects surface formations.

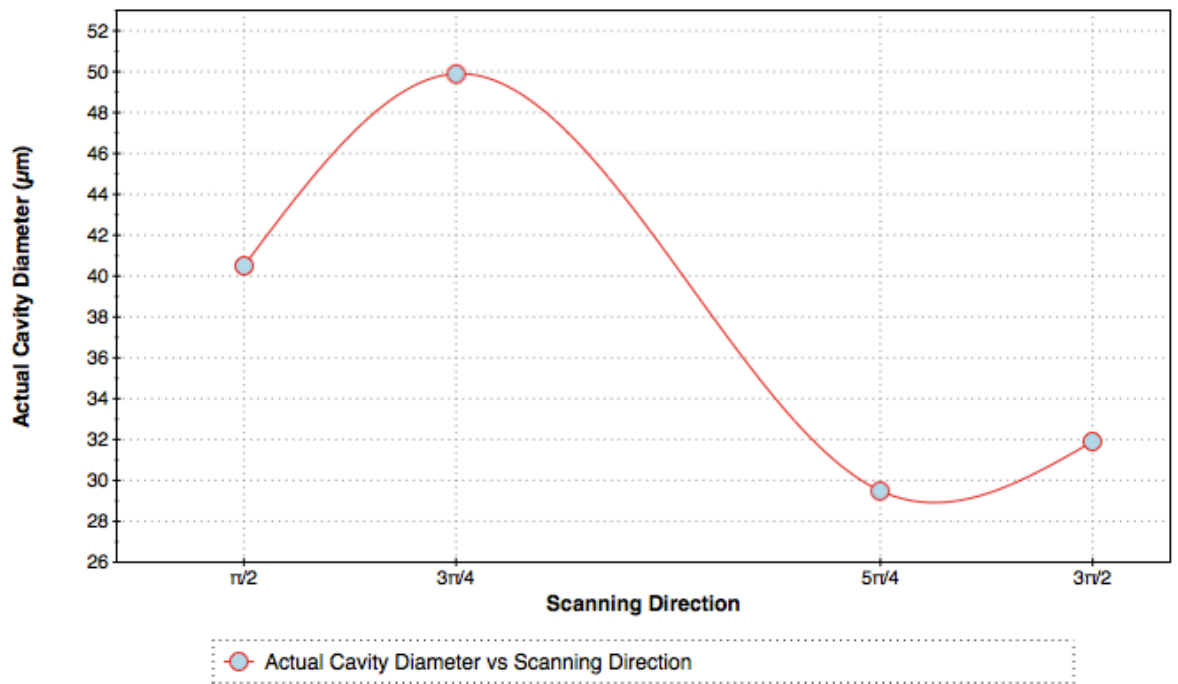


**Figure 4.42** Actual Cavity Diameter to Scanning Direction comparisons, polarization angle of  $90^\circ$  is used.

New experiments were run to further test the creation of dumbbell like structures. This time the middle channels of the dumbbell like structure ablated much more wider by the overlapping process as shown in **Figure 4.43**, which is overlapping half of the radius of one cavity to a side and ablating another cavity, then another until the desired width is reached.

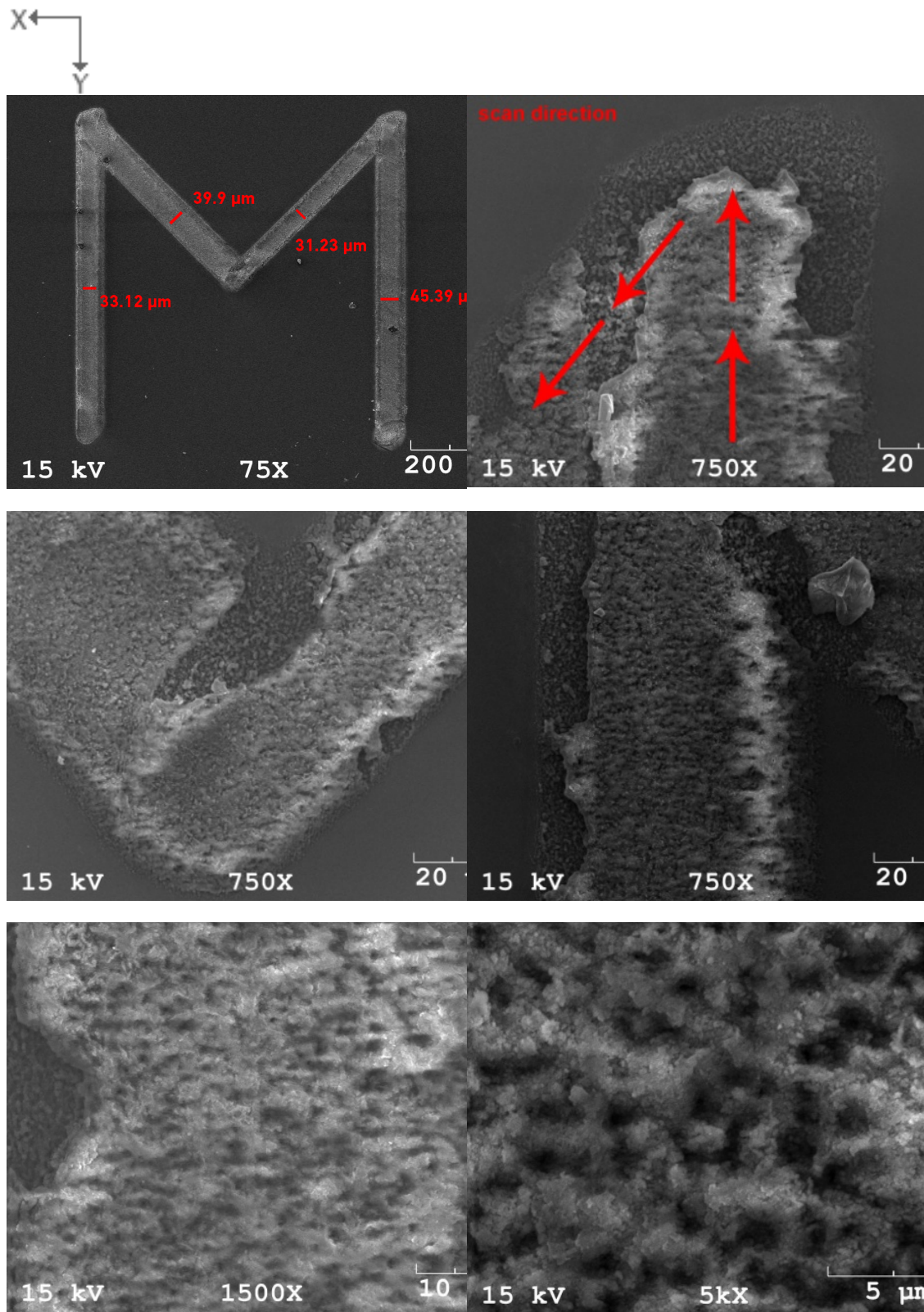


**Figure 4.43** Power: 230 mW, ScanSpeed:0.005 mm/s, Fluence: 17.4  $\text{j}/\text{cm}^2$ , Focal Length: 50 mm, Desired Cavity Diameter: 40.8 mm

## 5. CONCLUSION

We have utilized femtosecond laser between 0 mW and 220 mW power and between a wide range of velocities, repetition rates and between 0.1 khz and 1 khz frequency rates using focal lenses at 25.4 mm, 15 mm, 50 mm and 100 mm. After utilizing the laser with these parameters, following results were found.

- i. It is known that Femtosecond Laser is very advantageous in micro-machining due to the thermal diffusion law. However unless the micromachining method is run with the correct parameters, the advantages of the Femtosecond Laser Micromachining are useless.
- ii. One of the most important parameters to use correctly is; while micromachining the laser fluence must be kept between the melting threshold and the ablation threshold. It is easy to calculate the subject materials melting and ablation thresholds when examining it's surface characteristics. While no ablation occurs beyond melting threshold, beyond this threshold so called ripple like structures form on the surface.
- iii. These ripple shapes are first formed perpendicular to the electric field thus to the polarization angle. When number of pulses or fluence is slowly increased ripple like structures parallel to the polarization angle are formed.
- iv. After fluence is slowly increased, and when ablation is reached and number of pulses is exponentially increased ripples are replaced by long rectangular structures.
- v. The fluence marking this change from ripples to rectangles also marks the ablation threshold. After this threshold when fluence or number of pulses is increased the surface structure is first rectangular, then it turns oval and bubble like structures are formed and the surface is deformed which are schematically represented in **Figure 4.21**.
- vi. Cavities closest to the desired cavity width are those micro-machined with close to ablation threshold level cavities. That is to say figuring the ablation threshold and machining on fluence levels is one of the primary requirements of laser micromachining.

- vii. An important aspect is the increase of pulse numbers, while keeping the fluence between melting threshold and ablation threshold. The number of pulses can be controlled by manipulating the scan speed or by running multiple cycles on the cavity. Increase in the number of pulses means increase in the depth of the cavity. Thus desired depths can be reached by increasing the number of pulses.
- viii. Another important aspect is to keep the scanning direction and the polarization angle parallel to each other. This is important to achieve smooth surfaced cavities. To explain further when the scanning direction is moving in the x direction the polarizer angle must be  $0^\circ$  and when it's moving in the y direction, the polarizer angle must be set to  $90^\circ$ . Further to that when the scanning direction is both x and y the polarization angle must follow.
- ix. Otherwise deformed cavities are obtained.
- x. Lastly optical lens shape is also important. When comparing the experiment results, using high focal length lenses increases the achievable beam waist ( $W_0$ ). But this lowers the quality of the light hitting the material. This is thought to be an uncontrollable light burst.
- xi. When micromachining with high focal length lenses is compared, whether in literature or our own experiments, it yields unworthy results.
- xii. If wide cavities are desired, instead of using high focal length lenses, cavities overlapping each other to achieve wider and smoother cavities which are schematically explained in **Figure 4.39**.
- xiii. Taking these parameters into consideration while micromachining will yield fruitful results.

This body of work can be extended to produce microfluidic systems or direct glass bonded silicon based microfluidic systems.

Our findings can lead to the production of an integrated smooth and optimized mask of cavities. Silicon can be ablated without plasma formation. Because of this, uncontrolled surface deformations can be avoided.

## REFERENCES

- [1] **Dahotre, N.B., Harimkar, S.P.**, 2008, Laser Fabrication and Machining of Materials, Basics of Lasers, Chapter 1, Springer
- [2] **Wilson, J., Hawkes, J.F.B.**, 1987, Laser Principles and Applications
- [3] **Wee, L.M., Ng, E.Y.K., Prathama, A.H., Zheng, H.**, 2010, Micro-machining of wafer in air and under water, *Optics & Laser Technology* College of Engineering, Nanyang Technological University, Singapore, 62-71
- [4] **Chang, H., Tsai, Y., Cheng, C., Lin, C., Lin, Y., Wu, T.**, 2011, Nanostructured Ag surface fabricated by femtosecond laser for surface-enhanced Raman scattering, *Journal of Colloid and Interface Science*, National Chung Hsing University, China, November 9,
- [5] **Volodin, V.A., Korchagina, T.T., Koch, J., Chichkov, B.N.**, 2009, Femtosecond laser induced formation of Si nanocrystals and amorphous Si clusters in silicon-rich nitride films, *Physics E 42*, Institute of Semiconductor Physics, Germany, 1820-1823
- [6] **Kolasinski, Kurt W., Elsevier Ltd.**, 2009, Current Opinion in Solid State and Materials Science 13, West Chester University, West Chester, USA, 1-3
- [7] **Li, C., Shi, X., Si, J., Chen, T., Chen, F., Li, A., Hou, X.**, 2009, Fabrication of three-dimensional microfluidic channels in glass by femtosecond pulses, *Optics Communications 282*, Xi'an Jiaotong University, China, 657 - 660
- [8] **Lee, S., Yang, D. and Nikumb, S.**, 2007, Femtosecond laser micromilling of Si wafers, *Applied Surface Science 254*, Published by Elsevier B.V., Materials Institute, National Research Council, Canada, 2996-3005
- [9] **Yingling, Y.G., Conforti, P.F., Garrison, B.J.**, 2004, Theoretical investigation of laser pulse width dependence in a thermal confinement regime, *Applied Physics A 79*, 152 Davey Laboratory, Department of Chemistry The Pennsylvania State University, University Park, USA, 757-759
- [10] **Scuderi, D., Benzerga, R., Albert, O., Reynier, B., Etchepare, J.**, 2005, Spectral and temporal characteristics of metallic nanoparticles produced by femtosecond laser pulses, *Applied Surface Science 252*, GREMI, CNRS Universite d'Orleans, France, 4360-4363
- [11] **Alexander, D.R. and Rohlf, M.L.**, 2000, Date of Current Version, 06 August 2002, Propagation of Ultra-Short Femtosecond Laser Pulses in Aerosols, University of Nebraska, Lincoln, USA, 1742-1744

- [12] **Biegert, J., Kubecek, V., Diels, J.C.**, 1999, A New femtosecond UV source based on Nd: YAG, *OSA Trends in Optics and Photonics Series*, The University of New Mexico, Mexico, 59
- Brunner, B.D., Miller, R.J.D., Demmer, D., Walker, D.**, 1999, Programmable pulse shaping for optimized laser interactions, University of Toronto, 59
- [13] **Steen, W.M., Mzaumder, J.**, 2010, Laser Ablative Processes – Macro- and Micromachining, *Laser Material Processing*, London, United Kingdom, 371-387
- [14] **Stratakis, E., Ranella, A., Farsari, M., Fotski, C.**, 2009, Laser-based micro/nanoengineering for biological applications, Foundation for Research and Technology Hellas, Institute of Electronic Structure and Laser (IESL), Heraklion, Greece, 2-35
- [15] **Zorba, V., Stratakis, E., Barberoglou, M., Spanakis, E., Tzanetakis, P., Fotakis, C.**, 2008, Tailoring the wetting response of silicon surfaces via fs laser Structuring, *Appl Phys A 93*, Institute of Electronic Structure and Laser, Foundation for Research & Technology, Greece, 819-825
- [16] **Shah, L., Richardson, M., Tawney, J., and Richardson, K.**, 2000, Femtosecond micro-machining at atmospheric pressure air-ionization threshold, *Lasers and Electr-Optics Conference*, University of Central Florida, Orlando, Florida, USA, 14-15
- [17] **Bulgakov, A.V., Ozerov, I., Marine, W.**, 2004, Silicon clusters produced by femtosecond laser ablation: Non-thermal emission and gas-phase condensation, Institute of Thermophysics, *Applied Physics A 79*, Russia, Universit'e de la Mediterranee, France 1591-1594
- [18] **Halbwax, M., Sarnet, T., Delaporte, Ph., Sentis, M., Etienne, H. Torregrosa, F., Vervisch, V., Perichaud, I., Martinuzzi, S.**, 2007, Micro and nano-structuration of silicon by femtosecond laser: Application to silicon photovoltaic cells fabrication, *Thin Solid Films 516*, Paul Cezanne Aix-Marseille, France, 6791-6795
- [19] **Fishburn, J.M., Kapitan, D., Withford, M.J., Brown, D.J.W., Piper, J.A.**, 1999, Effect of Cumulative heating on micromachining in the explosive ablation regime with copper vapour lasers, School of Mathematics, Australia, 360-361
- [20] **Zheng, H.Y., Jiang, Z.W.**, 2009, Femtosecond laser micromachining of silicon with an external electric field, *Journal of Micromechanics and Microengineering Volume 20*, Singapore Institute of Manufacturing Technology, Singapore, 1-4
- [21] **Valle, G.D.**, 2008, Micromachining of photonic devices by femtosecond laser pulses, *Journal of Optics A: Pure and Applied Optics Volume 11*,

- [22] Nakata, Y., Miyanaga, N., Okada, T., 2007, Effect of pulse width and fluence of femtosecond laser on the size of nanobump array, *Applied Surface Science* 253, Institute of Laser Engineering, Osaka University, Japan, 6555-6557
- [23] Jia, J., Li, M., Thompson, C.V., 2004, Amorphization of silicon by femtosecond laser pulses, *Applied Physics Letters Volume 84 Number 16*, Massachusetts Institute of Technology, Cambridge, Massachusetts, 3205-3207
- [24] Bonse, J., Baudach, S., Kruger, J., Kautek, W., Lenzner, M., 2001, Femtosecond laser ablation of silicon—modification thresholds and Morphology, *Applied Physics A* 74, Federal Institute for Materials Research and Testing (BAM), Germany, 19-25
- [25] Zhu, J.T., Shen, Y.F., Li, W., Chen, X., Yin, G., Chen, D.Y., Zhao, L., 2005, Effect of polarization on femtosecond laser pulses structuring silicon surface, *Applied Surface Science* 252, Department of Physics and Surface Physics National Key Laboratory, Fudan University, Shanghai, China, 2552-2556
- [26] Mannion, P., Magee, J., Coyne, E., OConnor, G., 2000, Ablation thresholds in ultrafast laser micro-machining of common metals in air, *Opto-Ireland 2002: Optics and Photonics Technologies and Applications Conference*, National Centre for Laser Applications, National University of Ireland, Galway, Ireland, 470-478
- [27] Ameer-Beg, S., Perrie, W., Rathbone, S., Wright, J., Weaver, W., Campoux, H., 1998, Femtosecond laser microstructuring of materials, *Applied Surface Science* 127-129, University of Central Lancashire, UK, Colorado School of Mines, USA, 875-880
- [28] Li, C., Shi, J., Si, J., Chen, T., Zhang, Y., Hou, X., 2009, Photoinduced multiple microchannels inside silicon produced by a femtosecond laser, *Applied Physics A* 98, School of Electronics and Information, Engineering, Xi'an Jiaotong University, China, 377-381
- [29] Suriano, R., Kuznetsov A., Eaton M., 2011, Femtosecond laser ablation of polymeric substrates for the fabrication of microfluidic channels, *Applied Surface Science* 257, Istituto di Fotonica e Nanotecnologie, Politecnico di Milano, Milan, Italy, 6243-6250
- [30] Gonzalez, J.J., Fernandez, A., Oropeza, D., Mao, X., Russo, R.E., 2008, Femtosecond laser ablation: Experimental study of the repetition rate influence on inductively coupled plasma mass spectrometry performance, *Spectrochimica Acta Part B* 63, Universidad Central de Venezuela, 277-286
- [31] Wang, X., Chen, F., Liu, H., Liang, W., Yang, Q., Si, J., Hou, X., 2010, Femtosecond laser-induced mesoporous structures on silicon surface,

*Optics Communications* 284, Xi'an Jiao Tong University, Xi'an, China, 317-321

- [32] **Kam, D.H., Shah, L., Mazumder, J.**, 2011, Femtosecond laser machining of depth microchannel networks onto silicon, *Journal of Micromechanics and Microengineering* 21, University of Michigan at Ann Arbor, Michigan, 037901-1 – 037901-4
- [33] **Ming, Z., Dong-Qing, Y., Wei, Z., Jian, S., Bao-Jia, L., Juan, S., Lan, C.**, Received 2008, Sub-wavelength Ripple Formation on Silicon Induced by Femtosecond Laser Radiation, *Chin. Phys. Lett.* Vol.26, No.3, Jiangsu University, Zhenjiang, China, 1-5
- [34] **Korfiatis, D.P., Thoma, K.A.T., Vardaxoglou, J.C.**, 2009, Numerical modeling of ultrashort-pulse laser ablation of silicon, *Applied Surface Science* 255, Physics Department University of Patras, Rio, Patras, Hellas, Greece, 7605-7609
- [35] **Ivanov, D.S., Rethfeld, B.**, 2009, The effect of pulse duration on the interplay of electron heat conduction and electron–phonon interaction: Photo-mechanical versus photo-thermal damage of metal targets, *Applied Surface Science* 255, University of Kaiserslautern and Research Center OPTIMAS, Physics Department, Germany, 9724-9728
- [36] **Tan, B., Dalili, A., Venkatakrishnan, K.**, 2008, High repetition rate femtosecond laser nano-machining of thin Films, *Applied Physics A* 95, Ryerson University, Canada, 537,545
- [37] **Dabot, N.B., Harimkar, S.P.**, 2008, Laser Fabrication and Machining of Materials, Laser Drilling, *Laser Fabrication and Machining of Materials Chapter 4*, University of Tennessee-Knoxville
- [38] **Lorazo, P., Lewis, L., J., Meunier, M.**, 2008, Molecular-dynamics thermal annealing model of laser ablation of silicon, *Physical Review B*, D epartement de G énie Physique et de G énie des Mat ériaux et Groupe de Recherche en Physique et Technologie des Couches Minces (GCM), Ecole Polytechnique de Montr éal, Case Postale, Montr éal, Qu ébec, Canada, Universit é de Montr éal, Montr éal, Quebec, Canada, 1- 18
- [39] **Condeu, J.C., Gonza, P., Lusquin, F., Chiussi, S., Serra, J.**, 2007, Analysis of plume deflection in the silicon laser ablation process, *Applied Physics A* 88, University of Vigo, Dpto. Fisica Aplicada, Lagoas-Marcosende, Spain, 667-671
- [40] **Rullie, C.**, 2005, Femtosecond Laser Pulses, Principles and Experiments Second Edition, Centre de Physique Moleculaire Optique et Hertzienne (CPMOH) Universit é Bordeaux, Commissariat á l'Energie Atomique (CEA) Centre d'Etudes Scientifiques et Techniques d'Aquitaine, France, 1-437

- [41] **Von Der Linde, D., Sokolowski-Tinten, K., Bialkowski, J.**, 1997, Laser–solid interaction in the femtosecond time regime, *Applied Surface Science 109/110*, Universitat Essen, Germany, 1-10
- [42] **Yu. Izawa, S. Tokita, M.Fujita, T.Norimatsu, and Y.Izawa**, 2006, Ultra fast crystallization of amorphous Si by femtosecond laser irradiation,
- [43] **Lu,Y.F., Hong, M.H., Low,T.S.**, 1998, Laser plasma interaction at an early stage of laser ablation, *Journal of Applied Physics Volume 85, Number 5* ,National University of Singapore, Singapore, 2899-2903
- [44] **Dabotre, N.B., Harimkar, S.P.**, 2008, Laser Fabrication and Machining of Materials, Laser interference processing, Chapter 11, University of Tennessee-Knoxville, 451-476
- [45] **Sokolowski-Tinten, K., Bialkowski, J., Cavalleri, A., Von Der linde, D.**, 1998, Transient States of Matter during Short Pulse Laser Ablation, *Physics Review Letters, Volume 81, Issue 1*, Universitat Essen
- [46] **Von Der Linde, D., Sokolowski-Tinten, K., Bialkowski, J.**, 1996, Laser Solid interaction in the femtosecond time regime, *Applied Surface Science 109/110*, Universitat Essen, Germany, 1-10
- [47] **Anisimov, S.I., Luk'yanchuk, B.S.**, 2002, Selected problems of laser ablation theory, *Physics-Uspexhi 45 (3)*, Russian Academy of Sciences,Russia, 293-324
- [48] **Juergen, R.**, 2010, Basic Physics of Femtosecond Laser Ablation, *Laser-Surface Interactions for New Materials Production*, 19-41
- [49] **Lewis, L.J., Perez, D.**, 2008, Laser ablation with short and ultrashort laser pulses: Basic mechanisms from molecular-dynamics simulations, *Applied Surface Science 255*, Universite' de Montre'al, Canada, 5101-5106
- [50] **Zoubir, A., Shah, L., Richardson, K., Richardson, M.**, 2003, Practical uses of femtosecond laser micro-materials processing, *Applied Physics A 77*, School of Optics/CREOL, University of Central Florida, USA, 311-315
- [51] **Zoubir, A., Shah, I., Richardson, K., Richardson, M.**, 2003, Practical uses of femtosecond laser micro-materials processing, Laser Plasma Laboratory, School of Optics/CREOL, University of Central Florida, 4000 Central Florida Blvd., PO Box 162700, Orlando, FL 32816, USA
- [52] **Furusawa, K., Takahashi, K., Kumagai, H., Midorikawa, K., Obara, M.**, 1999, Ablation characteristics of Au, Ag, and Cu metals using a femtosecond Ti:sapphire laser, Department of Electronics and Electrical Engineering, Keio University
- [53] **Dabotre, N.B., Harimkar, S.P.**, 2008, Laser Fabrication and Machining of Materials, Laser micromachining, Chapter 7, University of Tennessee-Knoxville, 247-288

- [54] <<http://www.amplitude-systemes.com>>, retrieved on 29.01.2011
- [55] Cavelleri, A., Sokolowski-Tinten, K., Bialkowski, J., Schreiner, M., Von Der Linde, D., 1998, Femtosecond melting and ablation of semiconductors studied with time of flight mass spectroscopy, *Journal of applied physics Volume 85, Number 6*, Universita't-GHS-Essen, Germany, 3301-3309
- [56] Barsch, N., Korber, K., Ostendorf, A., Tonshoff, K.H., 2003, Ablation and cutting of planar silicon devices using femtosecond laser pulses, *Applied Physics A 77*, Laser Zentrum Hannover e.V., Hannover, Germany, 237-242
- [57] Coyne, E., Magee, J.P., Mannion, P., O'Conner, G.M., Glynn, T.J., 2004, Characterisation of laser ablation of silicon using a Gaussian and computer generated wavefront reconstruction, *Applied Surface Science 229*, University of Ireland-Galway, Galway, Ireland, 148-160
- [58] Dalili, A., Tan, B., Venkatakrishnan, K., 2010, Silicon wafer surface patterning using femtosecond laser irradiation below ablation threshold, *Optics and Lasers in Engineering 48*, Department of Mechanical and Industrial Engineering, Ryerson University, 350 Victoria Street, Toronto, Ontario, Canada, 346-353
- [59] Schade, M., Varlamova, J., Reif, J., Blumtritt, H., Erfuth, W., Leipner, H.S., 2009, High-resolution investigations of ripple structures formed by femtosecond laser irradiation of silicon, *Anal Bioanal Chem 396*, Martin-Luther-Universität Halle-Wittenberg, Brandenburgische Technische Universität Cottbus, Germany, 1905-1911
- [60] Han, Y., Qu, S., 2010, The ripples and nanoparticles on silicon irradiated by femtosecond laser, *Chemical Physics Letters 495*, Harbin Institute of Technology, China, 241-244
- [61] Singh, A., Kapoor, A., Tripathi, K.N., Kumar, G.R., 2001, Laser damage studies of silicon surfaces using ultra-short laser pulses, *Optics & Laser Technology 34*, University, Tata Institute of Fundamental Research, India, 37-43
- [62] Von der Linde, D., Sokolowski-Tinten, K., 1999, The physical mechanisms of short-pulse laser ablation, *Applied Surface Science 154-155*, Universitat Essen, Germany, 1-10
- [63] Jurgilaitis, A., Nuske, R., Enquist, H., Navirian, H., Sondhauss, P., Larsson, J., 2009, X-ray diffraction from the ripple structures created by femtosecond laser pulses, *Applied Physics A 100*, Lund University, Sweden, 105-112
- [64] Reif, J., Varlamova, O., Ratzke, M., Schade, M., Leipner, H.S., Arguirov, T., 2009, Multipulse feedback in self-organized ripples formation upon femtosecond laser ablation from silicon, *Applied Physics A 101* Brandenburgische Technische Universität, Germany, 361-365

- [65] Harzic, R.L., Huot, N., Audouard, E., Jonin, C., Laporte, P., 2002, Comparison of heat-affected zones due to nanosecond and femtosecond laser pulses using transmission electronic microscopy, *Applied Physics Letters Volume 80, Number 21*, Universite Jean Monnet, France, 3886-3888
- [66] Alexander, D.R., Mihulka, B., Doerri D., 2002, Femtosecond laser drilling of high aspect ratio 1 $\mu$ m holes in silicon, *High-Power Laser Ablation IV*, University of Nebraska, USA, 383-393
- [67] Koch, J., Heiroth, S., Lippert, T., Gunther, D., 2010, Femtosecond laser ablation: Visualization of the aerosol formation process by light scattering and shadowgraphic imaging, *Spectrochimica Acta Part B 65*, Swiss Federal Institute of Technology, Zurich, 943-949
- [68] Borowiec, A., Mackenzie, M., Weatherly, G.C., Haugen, H.K., 2002, Transmission and scanning electron microscopy studies of single femtosecond-laser- pulse ablation of silicon, *Applied Physics A 76*, University, Ontario, Canada, 201-207
- [69] Katsuya O., Okano, Y., Nishikawa, T., Nakano, H., 2008, Dynamic Imaging of Femtosecond Laser Ablation Plume by Using Laser-Generated Soft X-Ray, NTT Basic Research Laboratories, Japan, 864-865
- [70] Barada K. Nayak and Mool C. Gupta, 2005, Femtosecond Laser-Induced Micro-Structuring of Thin a-Si:H Films, *Material Research Society Symp. Proc. Vol.850*, Old Dominion University, Virginia, USA, MMI.8.1-MMI.8.5
- [71] Klinger, D., Łusakowska E., Kret, S., Kozankiewicz, B. and Z'ymierska, D., 2011, Surface morphology created by nanosecond laser annealing of amorphised Si layer Investigations by complementary methods, *Radiation Physics and Chemistry Volume 80, Issue 10*, Polish Academy of Sciences, Warsaw, Poland, 1-5
- [72] Tsai, H., Luo, S., Wu, C., Wang, J., 2009, Sub-micron-structure machining on silicon by femtosecond laser, *Trans. Nonferrous Met. Soc. 19*, National Taiwan Ocean University, National Tsing Hua University, China, s171-s177
- [73] Her, T.H., Finlay, R.J., Wu, C., Mazur, E., 2000, Femtosecond laser-induced formation of spikes on silicon, *Applied Physics A 70*, Harvard University, Cambridge, USA, 383-385

## **CURRICULUM VITAE**

**Name:** Şirin Didem Sofuođlu  
**Date and Place of Birth:** Ankara / 14.10.1981  
**Address:** Tahir Ekdal Sokak 14/2 ınar Apt.  
Feneryolu / Kadıköy İSTANBUL  
**University:** Istanbul Technical University